SINGLE AND DOUBLE DIRECT PHOTON PRODUCTION IN PION-PROTON INTERACTIONS AT 280 GEV/C

Michael Edward Joseph Feliks B.Sc.

Department of Physics and Astronomy,

University of Glasgow.

Presented for the degree of Doctor of Philosophy

in the University of Glasgow,

May 1989.

Acknowledgments

Many people and organisations have helped and supported me during my studies. In particular I must thank the following:

The Science and Engineering Research Council for their avuncular patronage.

The Department of Physics and Astronomy, University of Glasgow, under the direction of Professors E.W.Laing and I.S.Hughes, for providing me with a roof, a desk and a computer terminal.

My supervisors Drs. R.M.Turnbull and P.J.Negus, for all their help and encouragement, and the other staff members of the Glasgow WA70 group: Dr. J.G.Lynch, Dr. A.S.Thompson and Dr. J.Wells.

The many other physicists and students in the WA70 collaboration, whom it has been my pleasure to know. Amongst the non-Glasgow contingent, I would like to thank Dr. Maria Kienzle-Focacci and Michel Donnat of the University of Geneva in particular.

The computer operators in the Physics and Astronomy Department for their efficient performance.

Ms. Catherine McIntyre, for her practical help, not to mention running a message to Cairo for me.

Dr. Denis Hendry and the DESY and ALEPH students for their help and friendship.

Steve Wright and the Afternoon Boys deserve a mention.

Special thanks go to the students who worked on WA70 before me, and on whose software my Ph.D. reclines; Steven Jack, Richard Lucock and last but not least R. Alan Maxwell.

Lastly, I would like to thank my Aunt for putting me up and putting up with me, and Valerie for keeping me going.

Table of Contents. *Page*

Preface

This thesis decribes the work of the author during the period October 1985 to September 1988 as a postgraduate student in the Experimental High Energy Physics Group of the Department of Physics and Astronomy, University of Glasgow.

In October and November 1986 the author participated in a 40-day data-taking run of the experiment WA70, which was situated in the West experimental Area at CERN, Geneva, at the end of the H1 beam line from the CERN Super Proton Synchrotron (SPS). This experiment used the Omega Spectrometer together with a purpose-built photon calorimeter and MWPC to collect data on direct photon production by π^-, π^+ and proton beams of 280 GeV/c momentum incident on a liquid hydrogen target. The experiment, performed by a collaboration from the Universities of Geneva, Glasgow, Liverpool, Milan and Neuchatel, ran four times in 1983 (test run), 1984, 1985 and 1986. The author's work is based on the data collected during the last run, in which only π^- beams were used. In the course of this study, the author set up and ran existing computer programs to assist in the analysis, and wrote original programs to identify the double direct photon signal. The author was solely responsible for the single and double direct photon analysis of the '86 data at Glasgow.

Note

In this thesis, frequent reference is made to the Feynman x variable (usually written x_F) which is defined as

$$x_F = 2\, p_L / \sqrt{s},$$

where p_L is the longitudinal component of momentum in the centre of mass frame. Throughout the text the symbol xf is used to represent Feynman x and the symbol pt is used for transverse momentum.

Synopsis

This thesis presents results on single and double direct photon production in π^-p interactions at an incident beam momentum of 280 GeV/c, using data recorded by the CERN experiment WA70 at the Omega Prime Spectrometer in October and November 1986. The single direct photon cross-section is measured over the transverse momentum (pt) range 4.5→7.0 GeV/c and the Feynman x range -0.45→+0.45. The ratio of single direct photon to π^0 production was measured over the same pt range. The double direct photon cross-section is measured over the pt range 3.0→6.0 Gev/c.

Chapter One contains a short overview of Quantum Chromodynamics (QCD) and a discussion of the theoretical framework used to describe single and double direct photon production. A brief review of recent experimental results concludes the chapter.

Chapter Two describes the experimental apparatus used by WA70, in particular the large fine-grained calorimeter which was built specifically for the experiment.

Chapter Three discusses the computer programs used in the processing and analysis of the data. The reconstruction programs GLOBAL, OMGEANT and TRIDENT are described, as are the LUND and TWISTER Monte Carlo programs.

Chapter Four consists of a detailed discussion of the cuts made to isolate the single direct photon and π^0 signals, with special note being made of the problem of muon 'halo' contamination.

Chapter Five describes the determination of the detection efficiencies and acceptances for the single direct photon and π^0 signals and the calculation of the background to the single direct photon signal.

In Chapter Six the single direct photon and π^0 cross-sections are presented. A parametrisation of both is made, and the current results compared with those from

the 1984 and 1985 experimental runs. The direct photon cross-section is compared with results published by the contemporary direct photon experiments NA24 and UA6. This cross-section is then compared with the predictions from recent Beyond-Leading-Log (BLL) QCD calculations. A discussion of how the data can be used to measure the gluon distribution function and the fundamental QCD parameter Λ_{QCD} is also given.

Chapter Seven is devoted to the topic of double direct photons. The cuts used to isolate this signal are listed, followed by a detailed description of the background calculation. The detection efficiency and acceptance are discussed, and the final double direct photon cross-section presented. A description of the measurement of the coupling strength of the strong force α_s using the double and single direct photon cross-sections is given. The chapter concludes with a discussion of how the choice of scaling affects the interpretation of these measurements.

Conclusions are presented in the short Chapter Eight.

CHAPTER 1

The Theoretical and Experimental Status of Direct Photon Production in Hadronic Interactions.

1.1 Introduction.

Physicists have identified four fundamental forces in Nature: the Strong, Electromagnetic, Weak and Gravitational. At the scale of high energy particle physics the gravitational force is negligible, being a factor of $\sim 10^{-40}$ down as shown in the table below.

Force	Relative strength (at distance < 1fm)
Strong	1
Electromagnetic	1/137
Weak	10^{-10}
Gravitational	10^{-40}

Of the remaining three it is the strong force, despite its strength, which submits least readily to exact study in the laboratory. This is due to its being inherently more complicated that the others.

This thesis uses data from the CERN experiment WA70 to investigate the strong force by studying the phenomenon of direct (or prompt) photons. Experiment WA70 was designed, built and run by a collaboration of five unversities, namely Geneva University, Glasgow University, Liverpool University, Milan Univerity and

Neuchatel University.

The underlying motive in much of comtemporary particle physics is to unify these disparate forces into one theory. So-called 'Grand Unified Theories' aim to demonstrate that at a sufficiently high energy, greatly beyond the reach of present day particle accelerators, the strength of all three forces will be the same, as illustrated in fig. 1.1[1]. The weak and electromagnetic forces have already been unified by the 'Electroweak' theory [2], their coupling constants α_W and α_E becoming equal at an energy of 10^{15} GeV. At present the strong force remains largely outside the unification schemes.

The current understanding of the physical world at the level of elementary particles is embodied in the 'Standard Model' [3], a scheme containing the known particles, postulated particles expected to be seen, and the forces between them. The standard model is based on six 'quarks' - down, up, strange, charmed, bottom and top - from which hadrons are constructed. It stipulates six leptons, namely the electron, the muon, the tau and three varieties of neutrinos. The quarks and leptons fall naturally into 3 generations, as shown in fig. 1.2 [4]. The Standard Model also requires particles to act as carriers of the various forces. These are the photon (electromagnetic), the gluon (strong), the W^+, W^- and Z^0 (weak) and graviton (gravitational). The top quark and the graviton, together with another particle called the 'Higgs', which the theory requires to explain the masses of the others, have yet to be observed experimentally. The Standard Model is in no way intended as a definitive explanation of observed physical behaviour, but it is sophisticated enough for the purposes of this thesis.

The ensuing discussion is largely concerned with the strong force.

1.2 The Strong Force.

The field theory now widely accepted as describing the strong force is Quantum

Chromodynamics (QCD) [5]. In this theory quarks possess 'colour charge' and interact with other quarks via spin-1 exchange particles called gluons. Unlike the exchange particles of the other forces - the chargeless photon for electromagnetism and massless graviton, for example - gluons themselves carry colour and are therefore subject to the force they carry. This 'self-interaction' greatly complicates the theory.

The strength of the strong force for a particular energy transfer, Q^2, is characterised by $\alpha_s(Q^2)$, the 'coupling constant'. As the distance between two coloured particles increases, so does the attraction between them. This phenomenon would clearly give rise to difficulties in the theory were it not for the fact that quarks in hadrons arrange themselves into colour-neutral configurations, either aggregates of three quarks, one of each colour ('baryons') or of a quark of one colour and an antiquark of the same colour ('mesons'). (In the explicit wave function of a meson, all three colours are represented.)

QCD is a perturbative theory, based on expansion series in α_s. Calculating the cross-section for a particular subprocess is complicated and at present only two, or exceptionally three, orders of α_s are retained in the calculations and the cross-section is necessarily approximate. As a function of energy transfer Q^2, α_s can be written [6]

$$\alpha_s(Q^2) = \frac{12\pi}{(33-2N_f)\log(Q^2/\Lambda_{qcd}^2)} \qquad -1.1$$

where N_f is the number of quark flavours. Only leading (or first order) logarithms were retained in the calculation of this equation. The inclusion of further orders would give a different value of Λ_{QCD}, and this constant is not defined. It is often taken to be in the range 200 to 400 MeV. These considerations make the determination of the fundamental constants of QCD a matter of

definition as well as of experiment.

There is a further problem caused by the imperfect perturbative nature of QCD. Any attempted perturbative description of α_s will fail below an energy level of Λ_{QCD}, (the term $\log(Q^2/\Lambda^2_{QCD})$, in eqn. 1.1 will become negative), and no quantitative estimate can in fact be made by QCD in these energy regions. This is a great problem for experimentalists as it is in these regions that 'fragmentation' occurs.

Quark confinement prevents free quarks and gluons being detected since a coloured quark or gluon created at an interaction vertex will 'fragment' into a jet of colour-neutral hadrons, the parent particle of which is not identifiable from the observed jet. QCD cannot describe this 'fragmentation'.

We can circumvent this limitation by restricting study to reactions involving large momentum transfers e.g. those in which particles with high transverse momentum are produced.

Experimental uncertainty can also be reduced by studying sub-processes with one QCD vertex and one well understood electromagnetic vertex, rather than those with two purely strong vertices. A convenient case for study, as has often been pointed out since 1978 (e.g. [7] [8]), is direct (or prompt) photon production at high transverse momentum (pt).

1.3 Direct Photons.

A direct photon is defined as a photon produced in a hadronic collision which is not attributable to the decay of a known particle or resonance.

The QCD calculations describing the production rates for direct photons have been performed to next-to-leading order in α_s by Aurenche et al (1984) [9].

Rather than concentrating simply on quantitative cross-section predictions, studies in direct photon phenomenology often concern the behaviour of ratios with pt, xf etc. which can be checked qualitatively. The most commonly measured ratio is the ratio of direct photon production to π^0 production, which is expected to increase with pt . This ratio has been measured by WA70.

The direct photon signatures obtainable with different hadronic beams incident on a proton target also lend themselves to comparative ratios (eg. see [10]). Only π^-p interactions, however, are considered in this thesis.

Five years or so ago the error in the measurement of direct photon cross-sections and in the the QCD calculations predicting them were both of the order of a factor two. Experiment WA70 allows a measurement of the direct photon cross-section to within an uncertainty of 20%, while considerable progress has also been made on the theoretical side and the uncertainty there is now also around 20%.

1.4 The QCD Theory of Direct Photons.

Let us consider the inclusive production of direct photons in the general reaction AB→γX, where A and B are the interacting hadrons and X is any allowed particle or combination of particles. The invariant cross-section for this process is [11]

$$E\frac{d^3\sigma}{dp^3}(AB\rightarrow\gamma X) = \sum_{ab}\int_{x_a\ min}^{1} dx_a\ G_a^A(x_a,Q^2)\,G_b^B(x_b,Q^2)\frac{x_b}{\pi x_2}\ \frac{d\sigma}{dt}(ab\rightarrow\gamma c)$$

$$-1.2$$

where $G_a(x_a,Q^2)$ and $G_b(x_b,Q^2)$ are the probabilities of finding partons a and b with momentum fractions x_a and x_b in hadrons A and B respectively (fig. 1.3), and we have assumed that the constituent partons are massless and have no

'primordial' transverse momentum within the parent hadrons. G_a and G_b are determined from experimental data on lepton scattering and production [12].

Denoting the centre of mass scattering angle by θ, the rapidity y for massless partons is written

$$y = \ln \cot \theta/2.$$

We can rewrite equation. 1.2 as

$$E \frac{d^3\sigma}{dp^3}(AB \to \gamma X) = \sum_{ab} \frac{2}{\pi} \int_{x_{a\,min}}^{1} dx_a \; G_a^A(x_a, Q^2)\, G_b^B(x_b, Q^2) \frac{x_a x_b}{2x_a - x_T e^y} \frac{d\sigma}{dt}(ab \to \gamma c) \qquad -1.3$$

where

$$x_{a\,min} = \frac{x_T e^y}{2 - x_T e^{-y}} \qquad \text{and} \qquad x_b = \frac{x_a\, x_T\, e^y}{2_a - x_T\, e^y}.$$

We now consider generalized direct photon production at the partonic level, $ab \to \gamma c$.

Two sub-processes of order $\alpha\alpha_s$ are the principal sources of direct photons at high pt in hadronic interactions, namely 'Compton scattering' $qg \to \gamma q$, and 'quark-antiquark annihilation' $q\bar{q} \to \gamma g$. The Feynman diagrams for these sub-processes are shown in figs. 1.4a and 1.4b respectively.

Both processes have one well understood vertex (QED γ-γ coupling), and one involving a QCD interaction between quarks and gluons.

The differential cross-sections for these sub-processes can be written

$$\frac{d\sigma}{dt}(qg\rightarrow\gamma q) = e_q^2\,(-2)(1/6)\frac{\pi a a_s}{\hat{s}^2}\left(\frac{\hat{u}}{\hat{s}}+\frac{\hat{s}}{\hat{u}}\right) \qquad \text{'Compton'} \qquad -1.4a$$

and

$$\frac{d\sigma}{dt}(q\bar{q}\rightarrow\gamma g) = 2e_q^2\,(-4/9)\,\frac{\pi a a_s}{\hat{s}^2}\left(\frac{\hat{u}}{\hat{t}}+\frac{\hat{t}}{\hat{u}}\right) \qquad \text{'Annihilation',} \qquad -1.4b$$

where e_q is the quark charge, $\hat{s}$, $\hat{t}$ and $\hat{u}$ are the Mandelstam invariants for the sub-process and 1/6 and 4/9 are colour factors.

To summarize, we can write the QCD cross-section for direct photon production in the reaction $AB\rightarrow\gamma X$ as

$$E\frac{d^3\sigma}{dp^3}(AB\rightarrow\gamma X) = \sum_{ab}\frac{2}{\pi}\int_{x_a\ min} dx_a\; G_a^A(x_a,Q^2)\,G_b^B(x_b,Q^2)\,\frac{x_a\,x_b}{2x_a - x_T\,e^y}$$

$$\times\; e_q^2\frac{\pi a a_s}{\hat{s}^2}\;\times\begin{cases}(-1/3)\left(\dfrac{\hat{u}}{\hat{t}}+\dfrac{\hat{t}}{\hat{u}}\right) & \text{Compton}\\[2ex] (-8/9)\left(\dfrac{\hat{u}}{\hat{s}}+\dfrac{\hat{s}}{\hat{u}}\right) & \text{Annihilation}\end{cases} \qquad -1.5$$

to first order in a_s. A lengthy exposition of the QCD theory of direct photons is given in the review article by Owens [13].

1.5 Higher order corrections.

Some of the Feynman digrams used to calculate the next-to-leading order corrections to the QCD cross-sections are shown in figure 1.5.

Calculating the contribution of higher order diagrams to overall direct photon

production is dependent on choosing how to scale Q^2, which appears at several stages of the cross-section calculation in the structure and fragmentation functions and of course in the running coupling constant $\alpha_S(Q^2)$.

In a perfect calculation to all orders, the choice of Q^2 scale would not affect the final result. However in a limited order calculation a scale must be chosen arbitrarily and $Q^2 = n \times pt^2$ where $n > 0$ and ~ 1 is the most common choice.

Results of second order calculations have varied; contributions from higher orders up to 100% of the Born (first order) terms have been found. For example, Aurenche for π^+ on p, found the second order contribution to be 91% of the Born term [9] (pt=4 GeV, xf=0.0). A more empirical approach is to examine the effect large groups of higher order diagrams such as soft-gluon loops have on the overall cross-section and quantify it as a numerical 'K-factor'. Contogouris et al [14] have estimated the K-factor to be between 1.5 and 2.

1.6 Bremsstrahlung

A significant contribution to direct photon production at high pt is hadronic bremsstrahlung, where a parton in a hard scattering event radiates a photon. Examples of this are $qq \rightarrow qq(q \rightarrow \gamma q)$ $qg \rightarrow qg(q \rightarrow \gamma q)$ and $\bar{q}\bar{q} \rightarrow \bar{q}\bar{q}(\bar{q} \rightarrow \gamma \bar{q})$. A less important process is $g \rightarrow q\bar{q}(\bar{q} \rightarrow \gamma \bar{q})$.

Calculation of the bremsstrahlung cross-section involves the use of fragmentation functions such as $D_\gamma(z,Q^2)$, which gives the number of photons carrying fractional longitudinal momentum between z and z+dz. The variation of this function with Q^2 involves non leading-order terms and must be parametrised using experimental data. In general the fraction of direct photons produced by bremsstrahlung processes is < 30% (see fig.1.8).

1.7 Higher Twist Processes

When more than one of the partons in an interacting hadron participates in the scattering, we have a 'higher twist' event, such as $\pi q \rightarrow \gamma q$ shown in fig. 1.6.

The cross-section for this particular process is proportional to pt^{-6}, which might suggest a large cross-section at low pt. However, higher twist processes are suppressed by the (1-x) factors in the structure functions by several orders of magnitude relative to the parton-parton contributions described above [11].

The total predicted direct photon cross-section at $\sqrt{s}$=27.4 GeV (close to the $\sqrt{s}$=22.9 GeV of WA70) for $\pi^- p$ reactions together with the contributions from the two first-order processes, higher twist and bremsstrahlung processes, is shown in fig. 1.7 [15].

1.8 The γ/π^0 Ratio.

The ratio of the direct photon production to neutral pion production is expected to rise with pt. The experimental advantage of studying this ratio is that systematic errors in the measurement of each cross-section should cancel out. This ratio has been found to increase with pt in all previous experiments.

There are three reasons for expecting this to happen.

Firstly, consider a parton fragmenting into a jet of hadrons; the momentum of the parton will be divided among the fragmenting hadrons. The probability of a single hadron carrying most of the parton's momentum is low, but occasionally a single π^0 may carry most of the pt of the original parton. Direct photons however, carry 100% of their momentum to the detectors at all transverse momenta, so the π^0 cross-section will fall faster with pt than that for direct photons.

Secondly, many π^0s arise from the sub-process $gg \rightarrow gg$, which falls away more rapidly with pt than the direct photon production.

The third reason is that as pt increases, Q^2 increases, and this will lead to a lower α_s. Since the γ/π^0 ratio can be looked at simplistically as the ratio of the processes $qg \rightarrow q\gamma$ and $qq \rightarrow qq$, i.e. the ratio α/α_s as α_s falls the ratio will increase. Over the pt range considered in this thesis, however, this is a small effect.

1.9 Double Direct Photons.

Double direct photon production via the QED subprocess $q\bar{q} \rightarrow \gamma\gamma$ was discussed in the literature as early as 1971 [16]. This subprocess involves the point-like QED coupling between the quark and the photon, and is of great interest to theorists (fig. 1.8a). The differential cross-section for this process is;

$$\frac{dt}{d\sigma}(q\bar{q} \rightarrow \gamma\gamma) = 2e_q^4 \, (1/3) \, \frac{\pi\alpha^2}{\hat{s}^2} \left(\frac{\hat{u}}{\hat{t}} + \frac{\hat{t}}{\hat{u}} \right) \qquad - 1.6$$

The subprocess $gg \rightarrow \gamma\gamma$ (via a quark box diagram - fig. 1.8b) will also be present in pion and proton interactions, though in π^-p reactions the abundance of available u and $\bar{u}$ quarks will cause $q\bar{q} \rightarrow \gamma\gamma$ to dominate.

Bremsstrahlung from the hadronic product in single direct photon processes also contributes e.g. $qg \rightarrow \gamma q (q \rightarrow \gamma q)$ (fig. 1.8c).

Comparing the single direct photon cross-section (subprocesses of order $\alpha\alpha_s$ to the double direct photon cross-section (subprocesses of order α^2, will give the ratio

$$\frac{d\sigma(q\bar{q} \rightarrow \gamma\gamma)/dt}{d\sigma(q\bar{q} \rightarrow \gamma g)/dt} = \frac{3}{4} \frac{\alpha}{\alpha_s} e_g^2 \sim 10^{-2}. \qquad - 1.7$$

If we assume that annihilation dominates both single and double direct photon production we can, in principle, make a measurement of α_S. We can eliminate some of the error inherent in this assumption if we note that the annihilation term can be isolated by subtracting the π^+p signal from the π^-p signal. Defining the ratio R as

$$R = \frac{\sigma(\pi^-p\rightarrow\gamma X)-\sigma(\pi^+p\rightarrow\gamma X)}{\sigma(\pi^-p\rightarrow\gamma\gamma)-\sigma(\pi^+p\rightarrow\gamma\gamma)}$$

we note that at leading order approximation (and neglecting dd annihilation);

$$\alpha_S(LO) = (1/3)\alpha R$$

We must now take account of higher order processes in both the single and double direct photon cross-sections in equation. 1.7. (Some authors [17]. have commented on the advantages of normalising $\gamma\gamma$ pair production to e^+e^- production, so that part of the higher order QCD corrections drop out of the calculation since they are the same in both the processes considered. Though not done in this thesis, the e^+e^- signal could in principle be identified in the WA70 data.) Defining correcting 'K-factors' as equal to σ(BLL + Born)/σ(Born), K_1 corresponding to single direct photon production and K_2 to double, we can write

$$R = \frac{K_1\sigma_0(q\bar{q}\rightarrow\gamma g)}{K_2\sigma_0(q\bar{q}\rightarrow\gamma\gamma)} \qquad \sigma_0 \equiv \text{born term only.} \qquad 1.8$$

Aurenche et al have recently performed a full QCD calculation of the double direct photon cross-section [18]. Using the conventional scaling $M_1^2 = M_2^2 = Q^2 = pt^2$ then $K_1 \cong 1.6$ and $K_2 \cong 1.5$. However if the optimization discussed below is adopted (using Λ=200 MeV and Duke and Owens set I structure

functions) the K-factors decrease; $K_1 \cong 0.9$ and $K_2 \cong 1.2$. We defer any statement of preference between these schemes till chapter 7.

1.10 Scaling and Double Direct Photon Results.

The value of the a_s measurements made in this thesis would be lessened without a discussion of how scaling has been used to pinpoint the Q^2 region of the experiment. Work done by Aurenche et al [18], using the principle of minimum sensitivity [19] has suggested that WA70 is situated at a lower Q^2 region than the conventional $Q^2 = pt^2$ scaling indicates. The cross-sections predicted by QCD will vary with the choice of Q^2 scaling used in the coupling constants, the structure functions and the fragmentation functions. We must therefore consider our choice of scales carefully.

Aurenche considered the cross-section as a surface varying with M_1/pt M_2/pt and a/pt. He then examined this surface for the point at which the cross-section is varying least, i.e. a saddle point. Fig. 1.9 [20], shows a typical surface, for the process $pp \rightarrow \gamma X$. Using this 'optimization' of scales results in the assertion that WA70 is in the Q^2 range between 0.5 and 1.2, much lower than setting $Q^2=pt^2$ would indicate.

1.11 Previous Experimental Results.

The first experimental evidence for direct photons was found at the CERN Intersecting Storage Rings (ISR) in proton-proton collisions with $\sqrt{s}$ = 45 and 53 GeV, and was published in 1976[21]. (The early experiments are described in detail in the review paper of Ferbel and Molzon [22].)

The existence of direct photons was confirmed by a later series of experiments at the ISR, with data published between 1980 and 1983 (eg. [23] [24]

[28]).

Direct photons have also been observed by the experiment UA2 at the CERN $Sp\bar{p}S$ at $\sqrt{s}$ = 546, 630 GeV. The direct photon cross-sections produced by UA2 [26] were in agreement with QCD predictions but there were several sources of systematic errors in their analysis. The two photons produced by $\pi^0 \rightarrow \gamma\gamma$ decays could not be resolved (due to their very high energy) and were differentiated from direct photon showers by an algorithm based only on the isolation of the trigger shower from other particles in the event. They published updated and improved results in 1988 [27] including a tentative observation of four double direct photon events.

The handicap of the ISR and $Sp\bar{p}S$ experiments with respect to direct photon physics was that they had been designed to study many topics other than direct photons, and did not have the layout and performance in specific areas which would have made their study easier. The subject had to await dedicated direct photon experiments. Proposals were advanced for three of these in 1980/81. All were fixed target experiments at CERN, namely NA3, NA24, and WA70.

NA3 presented its first results in 1985 [28] It used π^-, π^+ and p beams on a carbon target at 200 GeV/c ($\sqrt{s}$ = 19.4 Gev). Significant numbers of direct photons up to a pt of 7 GeV/c were seen, but though the cross-section reported was in agreement with QCD predictions, the errors were too large for any preference between Duke and Owens set I or set II structure functions [29] to be made (fig. 1.10). More interestingly, the collaboration reported a 3 standard deviation double direct photon signal (fig. 1.11) [30], though their data was restricted to the pt range below 2.5 GeV/c. Better data on this process are required.

NA24 (which was essentially an upgrade of NA3) published their first results in 1987 [31]. They used π^-, π^+ and p beams at 300 GeV on a H_2 target at

$\sqrt{s}$ = 23.75 GeV). They identified a direct photon signal up to pt = 7 GeV/c and an xt of 0.6, where xt=2pt/$\sqrt{s}$. The cross-section was again in agreement with QCD predictions (fig. 1.12), but the errors were not small enough to favour either Duke and Owens' set 1 or set 2 structure functions. They also produced a measurement of the γ/π^0 ratio between pt = 3 and 7 GeV/c (fig. 1.13).

The experiment UA6 [32] used the antiproton beam at the Sp$\bar{p}$S collider on a gas jet target in fixed target mode with a $\sqrt{s}$ of 24.3 GeV. They have published data on direct photon inclusive cross-sections as well as a measurement of the γ/π^0 ratio up to a pt of 6.5 GeV/c (fig. 1.14). Their measurement of the single direct photon cross-section (fig. 1.15) clearly favoured the Duke and Owens set I structure functions and allowed set II to be ruled out.

Table 1.1 [11] shows in summary all the experiments which have produced data on direct photons. It includes the specifications of the Fermilab experiment E706, which should be able to reach a pt of 10 GeV/c. This experiment had an experimental run in 1987 but suffered badly from detector and accelerator problems.

Chapter One Figures and Table.

Figure 1.1 Evolution of fundamental coupling constants.

Figure 1.2 Schematic diagram illustrating the Standard Model.

Figure 1.3 Idealised diagram of a general direct photon producing hadronic interaction $AB \rightarrow \gamma X$.

Figure 1.4 The two lowest order QCD sub-processes producing direct photons;

a) Compton scattering, and

b) Quark-antiquark annihilation.

Figure 1.5 Some of the Feynman diagrams involved in the next-to-leading order QCD calculation of the direct photon cross-sections.

Figure 1.6 An example of a higher twist event, in this case $\pi q \rightarrow \gamma q$.

Figure 1.7 Diagram showing the how the cross-sections of the main direct photon producing subprocesses vary with pt, $\pi^- p$ reaction, $\sqrt{s}$ = 27.4 GeV and $\theta_1 = 90°$.

Figure 1.8 Feynman diagrams of three double direct photon producing subprocesses;

1) quark antiquark annihilation $q\bar{q} \rightarrow \gamma\gamma$,

2) the 'quark box' diagram $gg \rightarrow \gamma\gamma$ and

3) bremsstrahlung $qg \rightarrow \gamma q (q \rightarrow \gamma q)$.

Figure 1.9 Cross-section for the reaction $pp \rightarrow \gamma X$ as a surface

varying with M^2/pt^2 and α_s/π.

Figure 1.10 Direct photon cross-section as measured by the NA3 collaboration, $\pi^- p \rightarrow \gamma X$ at $\sqrt{s}$ = 19.4 GeV, showing QCD prediction of this cross-section made using Duke and Owens set I and set II structure functions (dashed and solid lines respectively). The open and closed circles refer to 'calorimeter trigger' and 'conversion trigger' respectively.

Figure 1.11 Double direct photon cross-section as measured by the NA3 collaboration, $\pi^- p \rightarrow \gamma\gamma X$ (•), and $pp \rightarrow \gamma\gamma X$ (o) at $\sqrt{s}$ = 19.4 Gev.

Figure 1.12 Direct photon cross-section as measured by the NA24 collaboration, $\pi^- p \rightarrow \gamma X$ at $\sqrt{s}$ = 19.4 GeV, showing QCD prediction of this cross-section made using Duke and Owens set I and set II structure functions (dot/dashed and dashed lines respectively).

Figure 1.13 The γ/π^0 ratio as measured by the NA24 collaboration, $\pi^- p$ reactions at $\sqrt{s}$ = 19.4 GeV.

Figure 1.14 The γ/π^0 ratio as measured by the UA6 Collaboration, pp reactions at $\sqrt{s}$ = 24.3 GeV.

Figure 1.15 Direct photon cross-section as measured by the UA6 collaboration, $p\bar{p} \rightarrow \gamma X$ at $\sqrt{s}$ = 24.3 GeV, showing QCD prediction of this cross-section made using Duke and Owens set I and set II structure functions.

Table 1.1 Parameters of recent direct photon experiments.

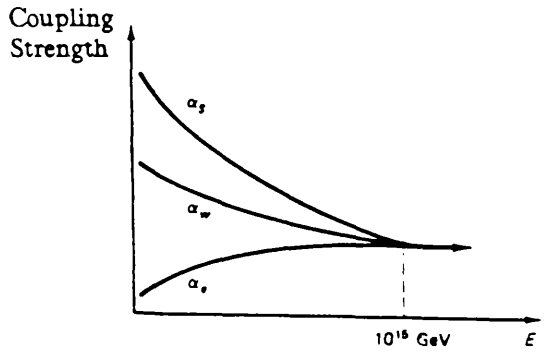

Evolution of the three
fundamental coupling constants.

Figure 1.1

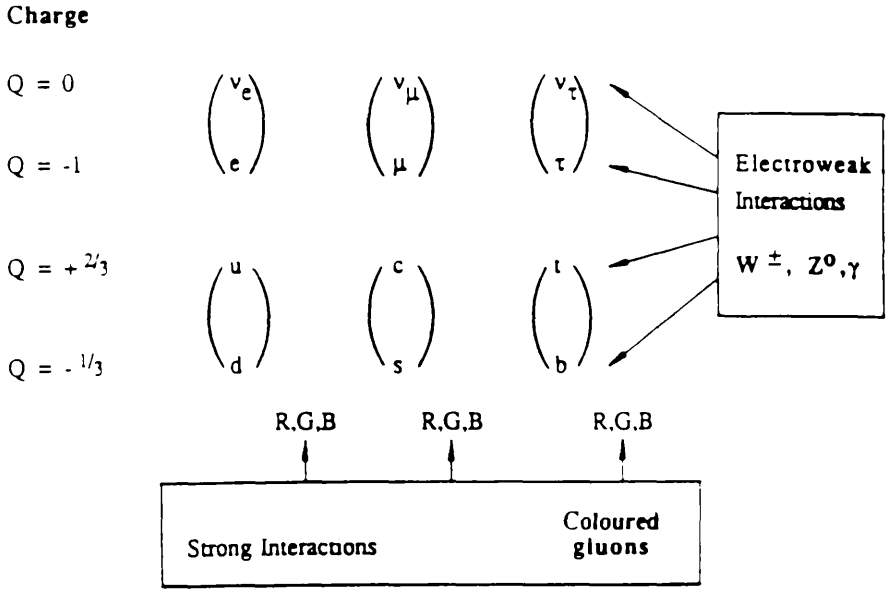

The leptons are sensitive only to the electroweak interactions; the quarks also experience the strong interaction via coloured gluons.

Figure 1.2

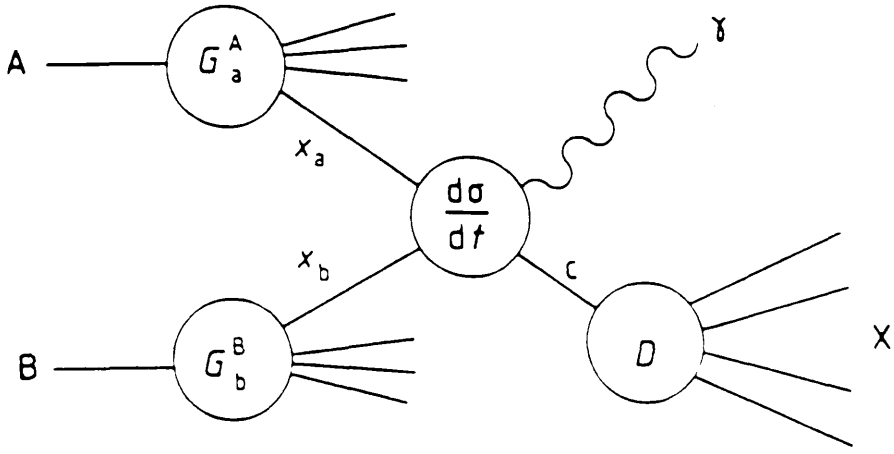

Figure 1.3

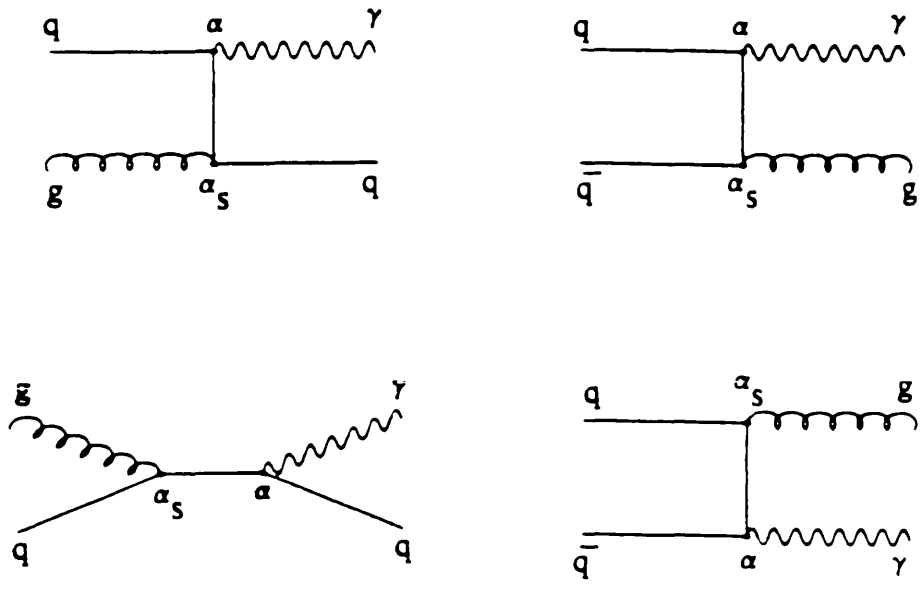

a) b)

Figure 1.4

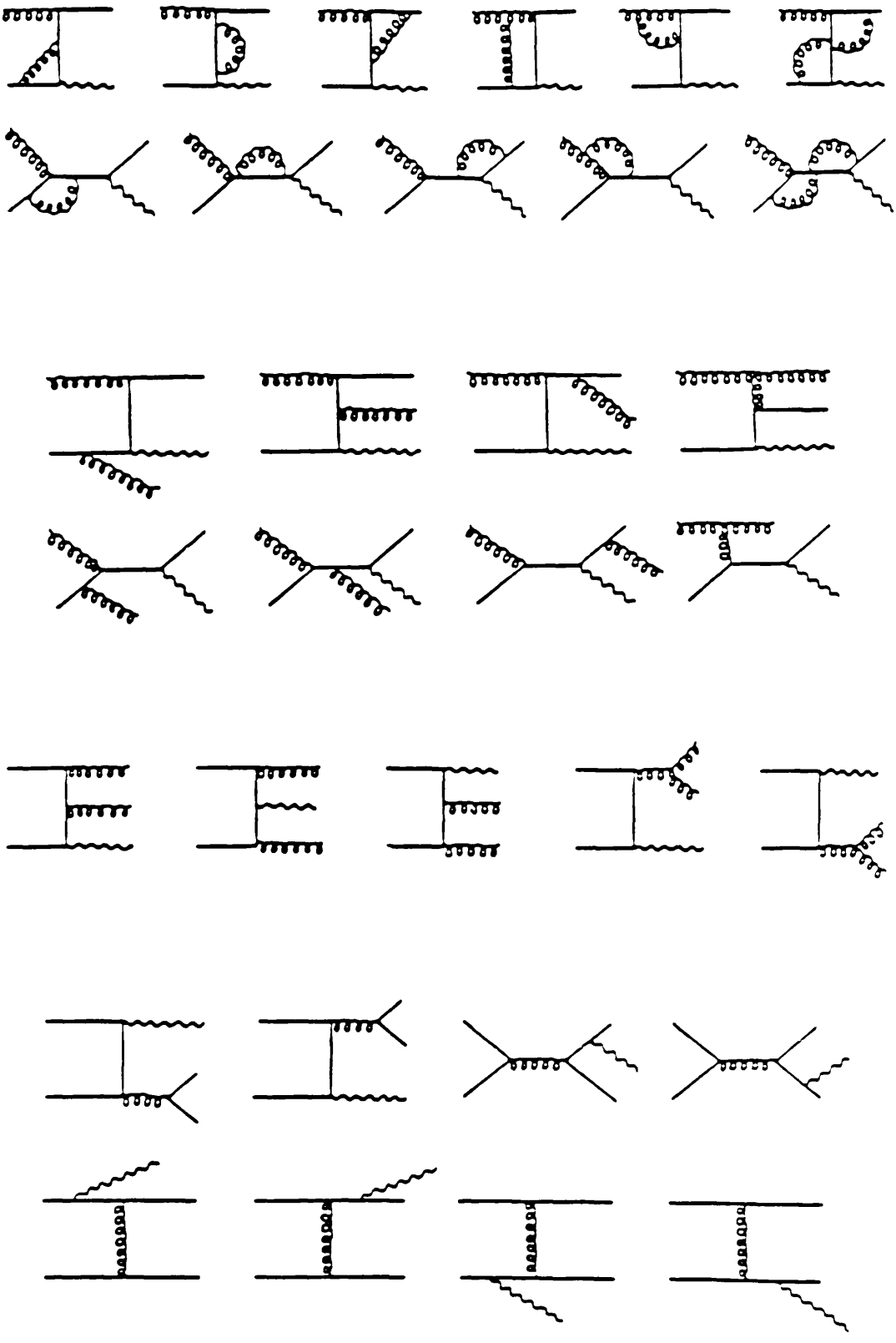

Figure 1.5

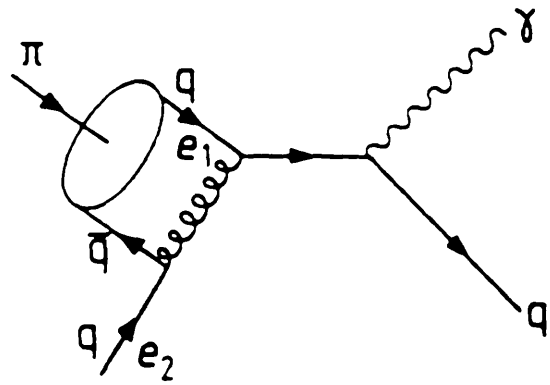

Figure 1.6

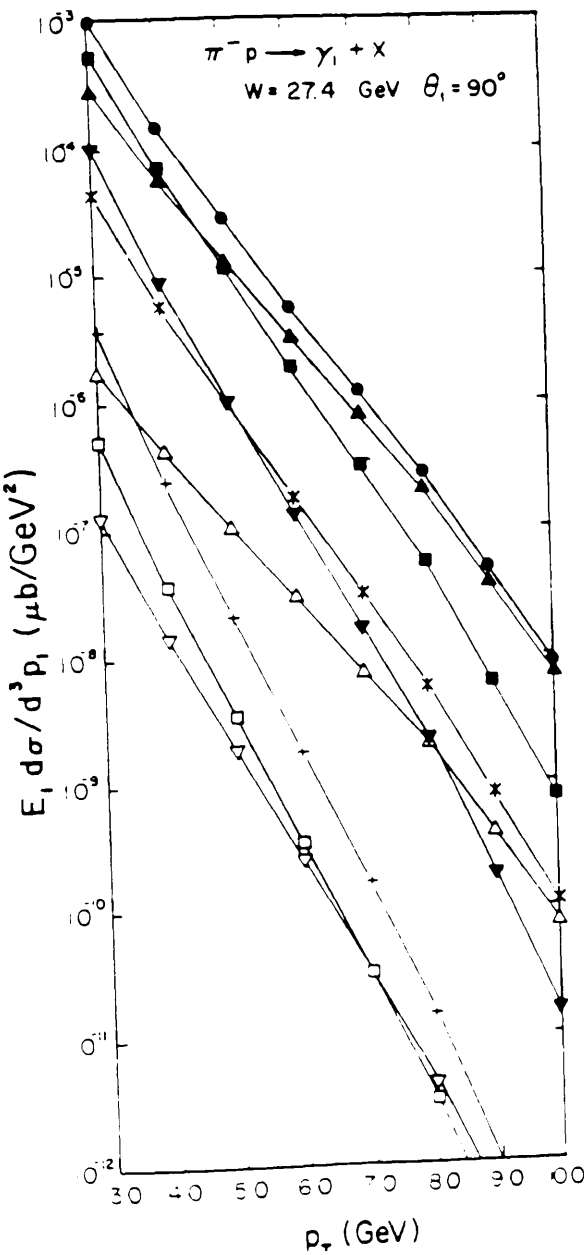

total (solid dots)

$gq \rightarrow \gamma_1 q$ (solid squares)

$q\bar{q} \rightarrow \gamma_1\gamma_2$ (up pointing open triangles)

$gq \rightarrow \gamma_2(q \rightarrow \gamma_1)$ (down pointing open triangle)

$qq \rightarrow (q \rightarrow \gamma_1)q$ (asterisk)

$gq \rightarrow g(q \rightarrow \gamma_1)$ (down pointing solid triangles)

$gg \rightarrow \gamma_1 g$ (plus sign)

$q\bar{q} \rightarrow \gamma_1 g$ (up pointing solid triangles)

$gg \rightarrow \gamma_1\gamma_2$ (open squares)

Figure 1.7

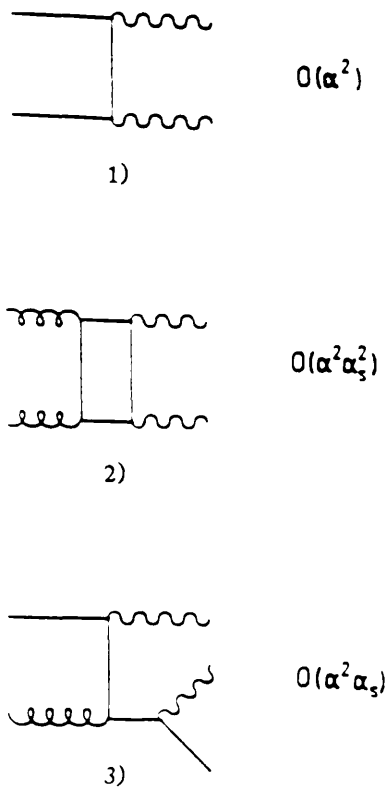

Figure 1.8

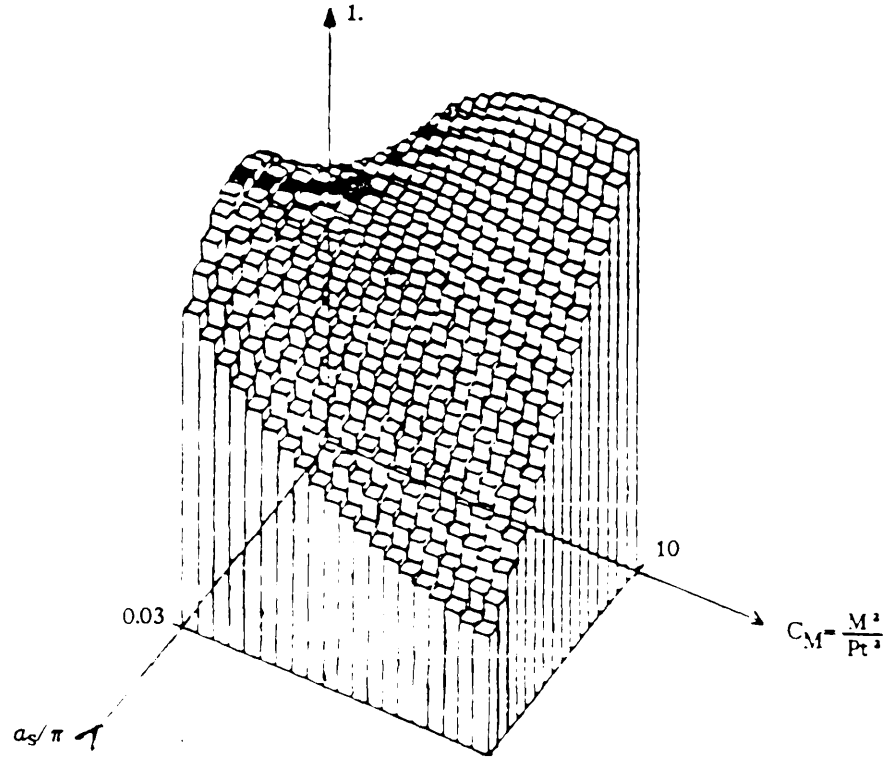

Figure 1.9

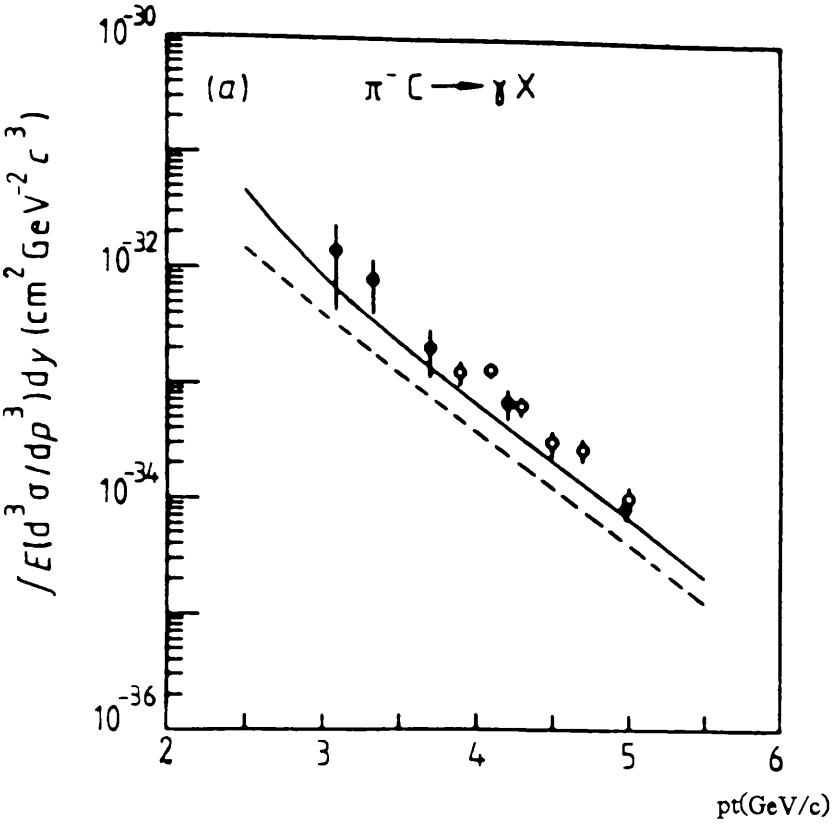

Figure 1.10

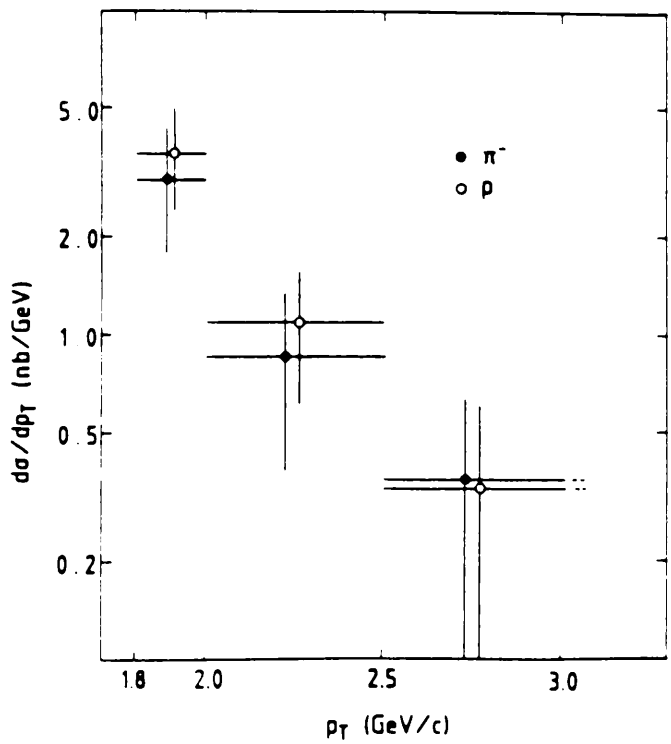

Figure 1.11

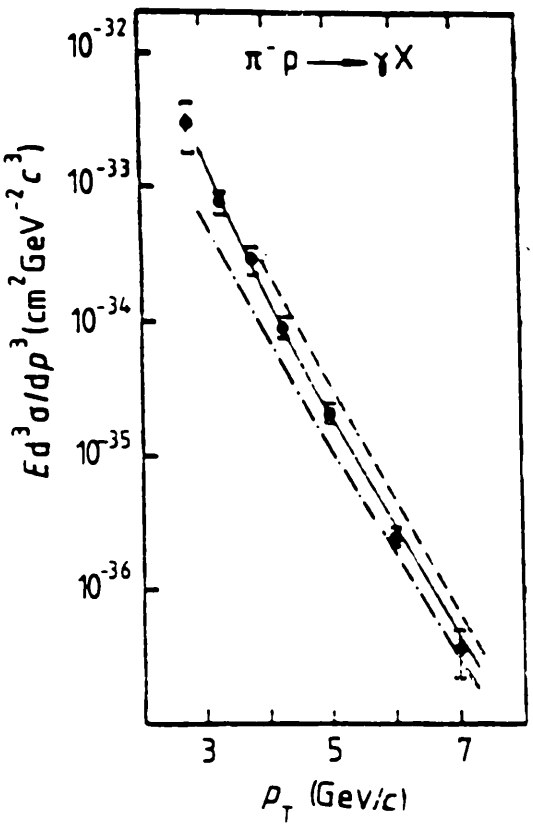

Figure 1.12

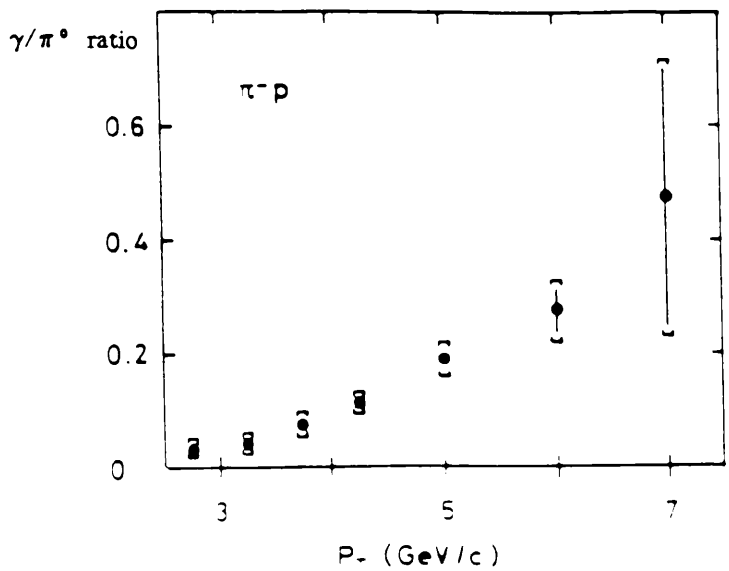

Figure 1.13

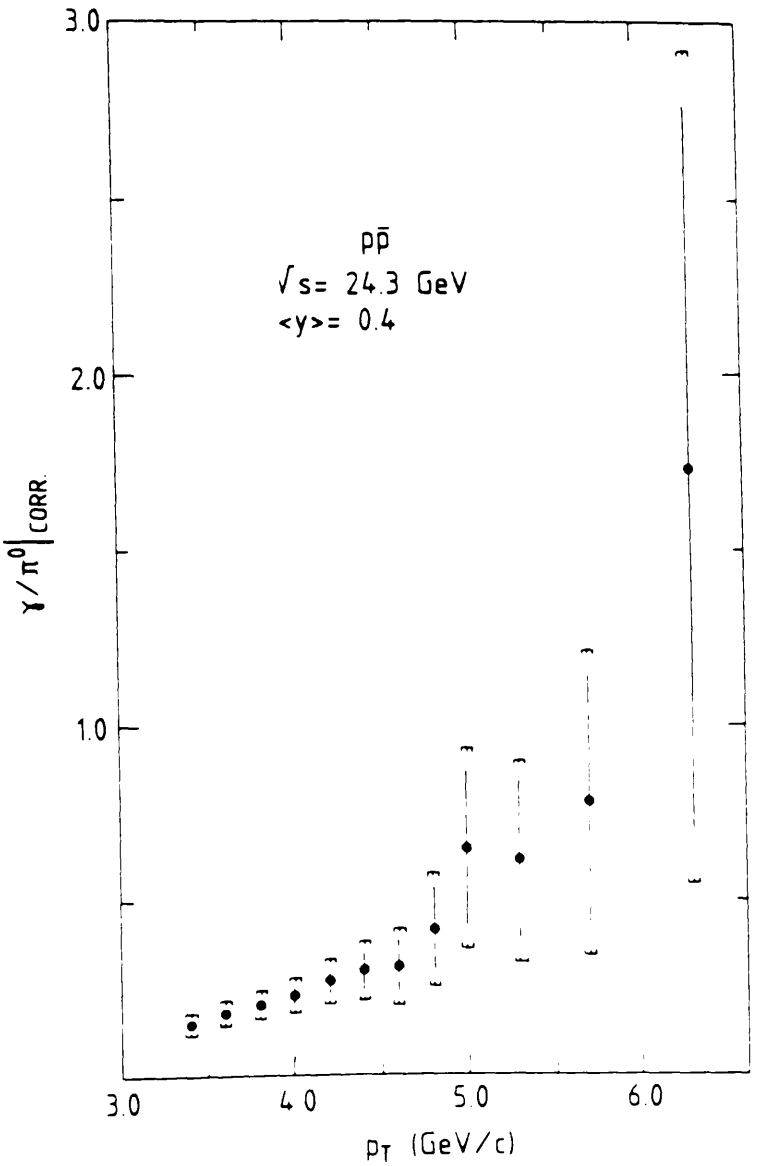
3.0
2.0
1.0
$\gamma/\pi^0|_{CORR.}$
$p\bar{p}$
$\sqrt{s}$= 24.3 GeV
<y>= 0.4
3.0
4.0
5.0
6.0
p_T (GeV/c)

Figure 1.14

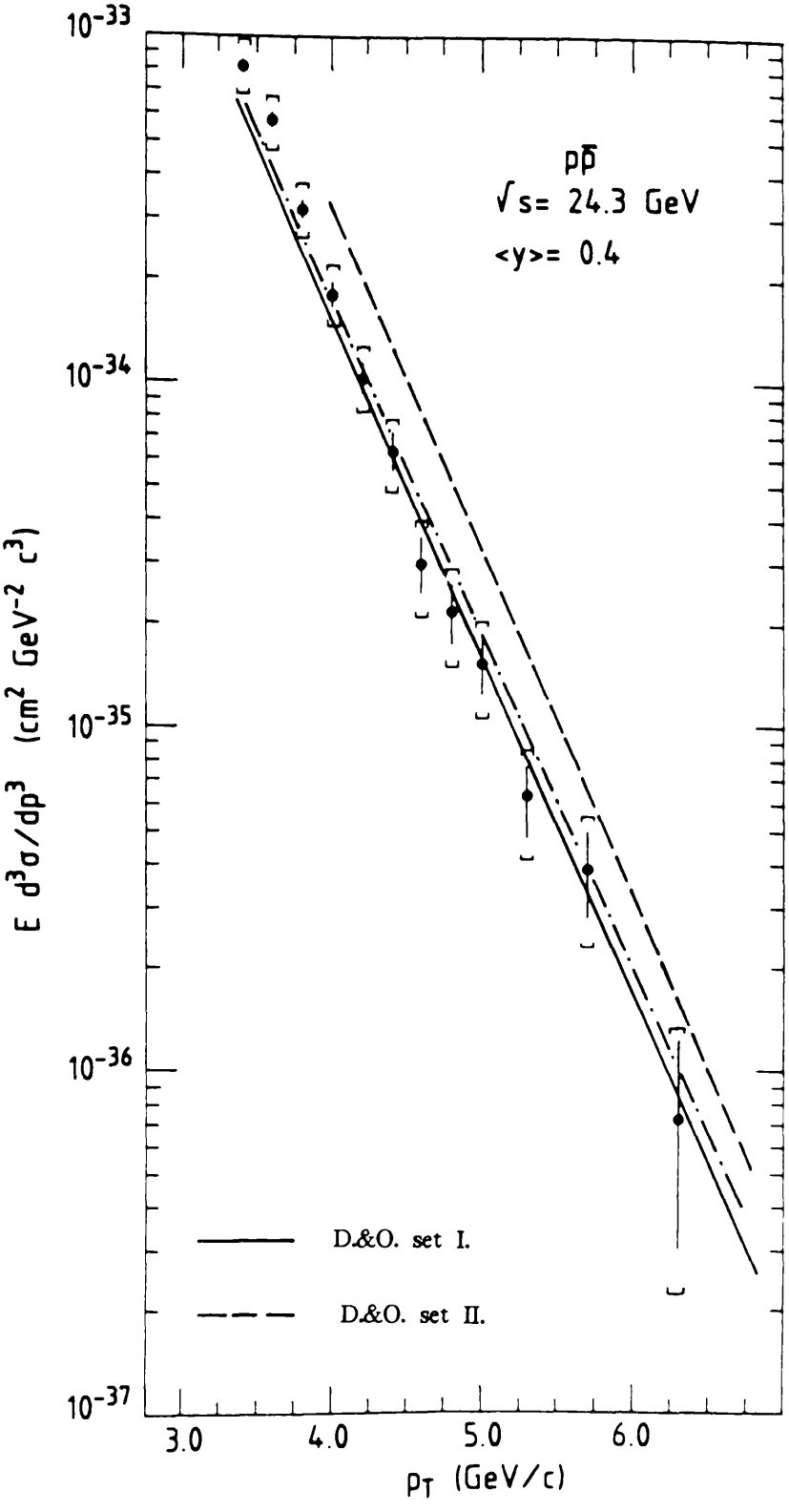
10^{-33}
10^{-34}
10^{-35}
10^{-36}
10^{-37}
$E\ d^3\sigma/dp^3$ (cm^2 GeV^{-2} c^3)
$p\bar{p}$
$\sqrt{s}$= 24.3 GeV
<y>= 0.4
D.&O. set I.
D.&O. set II.
3.0
4.0
5.0
6.0
p_T (GeV/c)

Figure 1.15

Table 1.1 Parameters of recent direct photon experiments.

Experiment	Beam (GeV/c)	Target	$\sqrt{s}$ (GeV)	p_t range (GeV/c)	Approximate x_t range	Energy resolution $\Delta E/E$ (E in GeV)	$\sigma(M_{\pi^0})$ (MeV)
McLaughlin *et al* FERMILAB E629	200 π^-, p	C	19.4	2–5	$0.2 < x_t < 0.5$	$0.14/\sqrt{E}$	6.5
Badier *et al* CERN NA3	200 $\pi^\pm$, p	C	19.4	3–5	$0.3 < x_t < 0.52$	$0.22/\sqrt{E}$	17
Bonesini *et al* CERN WA70	280 $\pi^\pm$, p	H_2	22.9	3.5–7	$0.3 < x_t < 0.7$	$0.15/\sqrt{E}$	10
De Marzo *et al* CERN NA24	300 $\pi^\pm$, p	H_2	23.75	3.5–7	$0.3 < x_t < 0.6$	$0.28/\sqrt{E}$	16
Camilleri *et al* CERN UA6	$\bar{p}$, p	p	24.3	2.5–5	$0.2 < x_t < 0.4$	$0.23/\sqrt{E}$	—
Akesson *et al* CERN AFS	$\bar{p}$, p	p	53.63	2–6	$0.06 < x_t < 0.2$	$0.09/\sqrt{E}$	15
Appel *et al* CERN UA2	$\bar{p}$	p	546,630	10–40	$0.03 < x_t < 0.13$	$0.15/\sqrt{E}$	—
Fermilab E706 (Future)	430, 500, 800 $\pi^\pm$, p	C Al, Be	28.5 30.65 38.76	3–?	$0.15 < x_t < ?$	$0.14/\sqrt{E}$	—

CHAPTER 2

The Experimental Apparatus.

The experimental apparatus has essentially six elements; beam line with trigger counters, H_2 target, Omega spectrometer, wire chambers and drift chambers, plus the electomagnetic calorimeter. This last was designed and built by the WA70 collaboration specifically to detect, with high efficiency, direct photons as well as photons arising from the decays of π^0s and ηs. Also especially built for WA70 was the large wire chamber (the 'BMWPC') which was positioned half a metre in front of the calorimeter. A side elevation of the experiment is shown in fig. 2.1.

The data acquisition system and the detector calibration are also discussed in this chapter.

2.1 The Beam Line.

The experiment was sited at CERN, Geneva. The accelerator used was the Super Proton Synchrotron (SPS), capable of delivering a beam of protons at 450 GeV into the H1 beam line, which extends from the central accelerator ring to CERN's West Experimental Area. Five hundred metres upstream of the H_2 target, this primary beam struck a 500mm beryllium target, producing various secondary beam particles. Downstream from this point collimators and the H1 magnets were used to isolate the desired type of particles with a selected momentum.

Both 'positively' and 'negatively' charged beams were used during the experiment's three main data-taking periods. The positive beam consisted of protons (82%),

positive pions (15%), and kaons (3%), while the negative beam consisted of antiprotons (0.3%), negative pions (97%) and kaons (2.6%).

Only negative beams were used in 1986 and it is upon data from that year that this thesis is based.

Particle identification was achieved using two CEDARs [32] (ring image Cerenkov counters) positioned about 10m upstream from the H_2 target. In these instruments a large spherical mirror in a gas-filled chamber is used to focus the Cerenkov radiation produced by a charged particle passing through the chamber onto a circle of eight photomultipliers. The diameter of the light ring is proportional to the speed of the particle (for a fixed gas pressure), and in a beam of known energy such as this the mass of the particle can be calculated. The gas pressure can be varied to cause the ring produced by a particle of a particular mass to fall exactly on the ring of photomultipliers. Since, in the 1986 WA70 run, the beam consisted almost entirely of π^-s, this mass was set to be that of the π^-.

Before a beam particle was accepted as a π^-, six of the eight photomultipliers in one of the two CEDARs had to record the presence of a light ring.

A cut-away diagram of a CEDAR of the type used is shown in fig. 2.2.

2.2 The Target and the Co-ordinate System.

A cylindrical target of liquid hydrogen was used. It was contained in a steel casing 100 cm long and 1.25 cm in radius. The liquid hydrogen was kept at a temperature of 30°K and had a density of 63 Kg/m^3.

The origin of the WA70 co-ordinate system was defined as the centre of the Omega Magnet. The x-axis was close to the beam direction (to be exact, it was taken as perpendicular to the vertical planes in the multi-wire chambers). The z

direction was taken as being vertical, and the y axis was defined to form a right-handed co-ordinate system. The co-ordinates of the centre of the downstream face of the target were (-3.5 cm,0,0).

2.3 The Omega Spectrometer - Charged Particle Detection.

The Omega Prime Magnetic Spectrometer [33] [34] was used to track charged particles and measure their momenta. The magnetic field generated by this 3000 tonne magnet is 1.5m high and has a half field diameter of 4m. The peak field used in this experiment was 1.18 Tesla.

Thirteen wire chambers were situated within the Omega yoke downstream of the target; firstly, the 6 'A' chambers and beyond these the 7 'B' chambers. The wire spacing in all the chambers was 2mm, and the 'A' chambers were closely packed to help vertex reconstruction.

The A and B chambers have respectively two and three wire planes. Defining the U and V planes as $\mp$ 10.14° to the vertical respectively, the configurations are (UY) and (YV) alternately in the A chambers, and UVY in the B.

On the downstream side of the Omega yoke are a butterfly chamber (2 planes, 4mm spacing, both Y plane), and two drift chambers (4 planes, 5cm spacing, planes UVYY', where Y' denotes a Y plane offset 2.5 cm).

Ten metres further downstream a large (4m x 4m) Big Multi Wire Proportional Counter (BMWPC) is positioned 50cm infront of the calorimeter. This purpose-built wire chamber has four wire planes (UYVZ) with a wire spacing of 4mm.

2.4 The Electromagnetic Calorimeter.

The experiment was designed to observe direct photons within an xf range of

-0.45 to +0.45, and to reconstruct the $\pi^0 \rightarrow \gamma\gamma$ decays which constitute the largest background to the direct photon signal. The configuration decided upon was a 4m x 4m calorimeter ([35] [36]) with a spatial resolution of 2 cm positioned 10m from the target. The calorimeter is shown in an isometric view in fig. 2.3.

A lead/liquid scintillator sandwich design was adopted which used tubes of liquid scintillator aligned along the Y and Z directions to record the coordinates of the 'hit'. The basic principle of the detector is shown in figs. 2.4a and b. A photon intersecting a scintillator tube in the Y plane at 'a' may produce a signal at the photomultiplier (Phil ips XP2972 [37]) similar to that produced by a less energetic one at 'b' (fig. 2.4a). It is not possible to deduce the distance of the shower along the scintillator using a single photomultiplier signal alone. Using the information from the tubes aligned in the Z plane however, we can deduce the shower position (fig. 2.4b).

In practice, several hits will register on the face of the calorimeter (an example of a real event is shown as fig. 2.5) and a computer program must be used to pair the PM signals correctly. WA70 uses the GLOBAL program to do this (see section 3.1).

This basic structure is employed throughout the calorimeter, which was divided into identical quadrants each with a sensitive face 205.4cm x 205.4 cm, with each quadrant further subdivided into 3 'segments'.

Each segment was composed of ten layers of lead 0.42 cm thick interleaved with sheets of 0.52 cm external diameter teflon tubes, containing NE235 liquid scintillator, aligned in the y and z directions alternately as described above. The spaces between the tubes were filled with epoxy resin. Fig. 2.6 shows the calorimeter construction in detail.

The whole assembly comprising 20 layers was placed in an aluminium frame and enclosed in a stainless steel frame to form a segment.

Not every scintillator tube constituted an independent channel; in fact 10 or 20 tubes (2 or 4 from each level of y- or z-tubes in a segment) are fed into a PM via a perspex light-mixer. Thus the channels were either 1.02 or 2.04 cm wide. The larger channel width is used in the outer regions of segments 1 and 2 and throughout segment 3 (fig. 2.7).

The scintillator tubes extended 25 cm beyond the lead/scintillator sandwich, where they were attached to glass windows fixed in the aluminium frame. From this window the light finally reached the PM via a 15cm light mixer (fig. 2.8). The PMs were connected to 12-bit charge integrated ADC's in the counting room.

To streamline data-taking several processors subtracted pedestals and recorded only those channels with a non-zero ADC signal and their immediate neighbours.

There are 3072 PM's in total and to adjust their voltages individually a computer-controlled system was necessary. The various high voltage supply units and CAMAC modules were in fact controlled by one of the data acquisition computers (see section 2.12).

2.5 Calibration of the Calorimeter.

It was not practical to manufacture the photomultipliers with exactly the same gain so their (relative) gains had to be measured before the calorimeter could be used.

Two independent systems were used to do this. One used a pulsed N_2 laser, while the other used movable radioactive sources mounted inside the quadrants.

The advantage of the laser system was speed; scans of the calorimeter took only 15 minutes, allowing them to be taken during the run. Against this, a (trouble free) source scan took at least 36 hours. The disadvantage of the laser system

was that inhomogenities in the photocathodes of the PMs could cause the reponses of PMs with the same gains to vary by 25%. This presented difficulties in measuring relative gains. The laser system therefore was used principally to check the PM gains for variation with time, while the source system was used to provide the absolute calibration. The rms error of the equalisation thus acheived was 4%, with further corrections using the data reducing the residual systematic error in gain across each quadrant to less than 1% [38].

2.6 The Laser System.

The basic idea behind this system was to deposit identical amounts of energy (pulses of laser light) into each scintillator tube using a N_2 laser which produced UV light with a wavelength of 337 nm.

The laser pulses had a full width half maximum of 4 ns and an energy of 10 mJ. A schematic diagram of the laser system appears as fig. 2.9. The light passes first through filters which can be used to vary its intensity, allowing tests on the linearity of the PM response to be conducted. The light is then passed through a scintillating mixture which shifts its wavelength in such a way as to make the pulse simulate the energy spectrum generated by the particles as they pass through the calorimeter. The resulting pulse is injected into a bunch of 25 fibres, each 6m long by 1.5mm diameter. One of the fibres is connected to two reference photomultipliers which are used to monitor the pulse to pulse laser output. The other 24 fibres transmit light to the calorimeter i.e. six per quadrant, two per segment, one per segment view. There are five scintillator layers per view each taking one fibre, so five bunches of twenty-five fibres are used, illuminated in turn by the laser.

In each segment, the light from each fibre is split (by a beam expander and a light-mixer) between 144 quartz fibres (96 in segment 3) contained in a stainless steel barette. These fibres then inject light into one scintillator tube per

photomultiplier in the calorimeter. This system was largely the responsibilty of the Neuchatel group.

2.7 The Source System.

The source system used movable ^{60}Co sources to deposit equal amounts of radiation into each scintillator tube. The strength of the sources was 5 milliCuries, where 1 Curie=3.7×10^{10} counts per second. They were mounted in polypropylene sheets built into each quadrant (fig. 2.10), cemented into chains which ran through channels cut in the polypropylene. The shape of the channels was such that the source could be positioned over every scintillator tube at 2 distances from the PM's, 'level 1' and 'level 2'.

Each segment has a source plate mounted behind and in front of it, so there are 4 sources in each quadrant. The chains are controlled by 4 clutches at the corner of the quadrant furthest from the beam hole. One motor drives all 4 clutches, and the whole system is under computer control. By 1986, the sources had decayed sufficiently (to $\sim$ 3.1 mCuries) to make readings at the distant 'level 2' position unreliable, so only level I readings were used for the '86 run.

'Source scans' were performed before and after the '86 run and also during the 4-day machine development break in mid-run. During the run itself laser scans were carried out daily.

The Source calibration system was the responsibility of the Glasgow group.

The laser and source systems are described in greater detail in the calibration paper [38].

2.8 The Energy Resolution of the Calorimeter.

The energy resolution of the calorimeter for isolated electromagnetic showers was studied using an electron test beam with electrons of momenta of 10, 20 and 50 GeV/c. It was shown to be

$$(\sigma_E / E)^2 = c_1^2/E + c_2^2$$

where c_1=0.126 GeV^2, c_2=0.032 and the energy E is in GeV. During real data-taking the calorimeter had to cope with overlapping showers rather than isolated ones, and this reduced its efficiency.

By the end of the last run, some 50 photomultipliers out of a total of 3072 had failed. This was not enough to seriously affect detector performance, however.

2.9 The Absolute Energy Calibration of the Calorimeter.

As the direct photon and π^0 cross-sections fell steeply with pt, an error in the absolute energy scale would cause a large uncertainty in their values at a specified pt. Quantitatively an uncertainty of 1% in the absolute energy scale caused an uncertainty of 10% in the cross-section.

The absolute energy calibration of the calorimeter was done by comparing the η mass obtained from reconstructed $\eta \rightarrow \gamma\gamma$ decays with its accepted value. This was done for each quadrant, the systematic variation in the η mass from quadrant to quadrant being less than 1%.

A voltage change was then made to all the PM's in the quadrant to bring the measured η mass into line with the accepted value.

The accuracy of the absolute energy scale was checked by comparing the momenta of electrons as measured by the Omega spectrometer with the shower energy measured at the calorimeter. The two quantities agreed to within 0.6%,

equivalent to an uncertainty of of ∓5% in the final cross-sections.

As a final check in '86, the reconstructed π^0 mass was also examined. It was found to be 135.5∓0.6 MeV/c^2. The energy calibration in '84 and '85 was done primarily with the π^0, but in '86 the η was thought to be more reliable because of the possibility of threshold effects affecting the π^0 mass peak.

Finally, uncertainty in the measurement of a shower's energy will be introduced if the gains of the PMs' drift between measurements by a source or laser scan. A study of this in '86 found that the PM gains were drifting by only 0.5% per day per channel, and since the laser scans were done daily even this small drift was corrected for, and the error introduced into the cross-section assumed to be negligible.

2.10 The Time-of-Flight System.

Since the calorimeter does not have a "tower-structure", when a group of particles hits it only a set of y- and z-coordinates are produced. These must be matched to find each particle's impact position. Sometimes different hypotheses can be reached to reconstruct the hit positions, so to reduce ambiguity a time-of-flight (TOF) system [49] was built into the WA70 calorimeter assembly.

It compared the elapsed time between a hit in the calorimeter and a (delayed) signal from a counter in the beam upstream from the target.

Specifically, an output was fed to a discriminator from the second last dynode on each PM in the first segment of the calorimeter. A 'hit' in the calorimeter sent a pulse to the discriminator which caused a constant current to be input to a charge integrating ADC. This was stopped by a delayed pulse from the beam counter S2. This pulse was set in coincidence with the high pt calorimeter trigger such that the charge collected by the ADCs is an indication of the time elapsed

from the trigger particle passing a particular point in the beam line to the resulting showers appearing at the calorimeter.

To calibrate the system the relative timing of the PMs had to be known as well as the ADC-to-time conversion factor for each channel. The first could be measured by simply feeding signals from the laser into each photomultiplier (real data being used to refine the measurements). The second was measured by feeding a laser signal into each PM with and without a delay in the 'stop' signal for the current generators.

The exact time at which each discriminator fired was dependent on the rate of increase in the PM signal, which varied with shower energy. Every TOF signal was therefore corrected for this, a study of the problem having been made using an electron scan.

A further, event-by-event correction was made to the TOF values to allow for the jitter in the 'stop' signal from the beam counter.

The spatial resolution of the TOF system was $\simeq$ 4 cm for a 5 GeV shower. Showers with energies of less than 1 GeV could not be usefully dealt with by the TOF system.

2.11 The Trigger.

WA70 had three triggers: the 'interaction trigger', the 'calorimeter trigger', and the 'MICE' trigger.

1) The Interaction Trigger.

The interaction trigger was designed to check that an interaction in the target had genuinely taken place. It used various counters and anti-counters in the beam line (fig. 2.1), in the following way;

a) To establish the presence of an incoming beam particle, the signal

$$CB = S2.S4.\overline{V4A}.\overline{V4B}.\overline{V2}$$

had to be logically positive. This was called 'Clean Beam'.

b) If the particle had not interacted with the target, counters A1 and A2 would fire. In 1984 and 1985 a requirement for an event to be accepted was that these two counters did not fire. However a small problem was caused by charged tracks from genuine direct photon events firing counters A1 and A2, thereby vetoing the event. To counter this in 1986 a magnet and two extra counters, A3 and A4 (fig. 2.11), were added downstream of A1 and A2 in such a configuration that beam particles would be swept round through A3 and A4. A particle with lower momentum would, however, not pass through the counters. A real interaction was signaled, therefore, by a positive 'INT' signal, defined as

$$INT = CB.\overline{(A1.A2.A3.A4)}$$

2) The Calorimeter Trigger

Recalling (section 1.3) that WA70 was interested only in high pt events, the calorimeter trigger was designed to accept events which had sufficiently high pt to be of interest.

To facilitate this, the face of each quadrant was divided into 16 square cells and the transverse energy deposited in each cell calculated. Outputs were taken from the last dynode of each PM and weighted to give a signal proportional to the transverse energy of that co-ordinate. The outputs from the PMs constituting one strip of four cells were summed, passed through a pulse-shaping amplifier, and sent to the trigger electronics [40].

(Each cell overlapped its neighbours by one photomultiplier to avoid any loss of events due to a shower cluster being split.)

The trigger electronics made a two level decision based on the distribution of transverse energy (E_t) across the calorimeter.

i) The first level tested for the condition $E_{ti} > K$? where i denotes any strip of any quadrant, and K a given threshold. This removed events without any significant interaction in the calorimeter.

ii) In the second the amount of transverse energy in each cell was calculated by matching the signals from the strips crossing it. The outputs calculated in the first level were digitised using flash ADC's and passed to a set of look up-tables. For each cell there were four of these in parallel, thus allowing four different triggers to be set. If an event successfully passed any of these it progressed to the third level of the trigger, the MICE microcomputer (see next section). Each look-up table took the E_{ty} and E_{tz} pairs and checked the following conditions;

a) $E_{ty} > L1$;

b) $E_{tz} > L2$;

c) $E_t = \sqrt{(E_{ty}^2+E_{tz}^2)} > T$; and

d) asymmetry = $|E_y-E_z|/(E_y+E_z) < AMAX$,

where L1, L2, T and AMAX were pre-set limits, and E_y and E_z were the apparent energies in each view. This level presupposed that all the energy seen in any two y and z strips was deposited in the strips where they overlapped, the quantities Ety and Etz for each cell being corrected for attenuation down the scintillator tubes. Clearly this was unrealistic and condition (d) above is intended to reduce spurious triggers.

Out of four possible triggers only two were used in 1986. One was set to record candidate single direct photon events, and required a shower with a pt of at least 3.5 GeV/c in the event, while the other (known as 'trigger 4') was set with the intention of recording double direct photon events. This trigger required

showers with a pt greater than 1.8 GeV/c to be found in two opposite quadrants i.e. 1 and 3 or 2 and 4. The reason for keeping events with such low pt was to record π^0s and η's with a pt > 3.0 GeV/c and asymmetry $\simeq$ 0.5. These would be used later in connection with the calculation of background to the double direct photon signal.

The search for double direct photons is dealt with in Chapter 7.

3) The MICE microprocessor system.

The third level of the trigger was the MICE microcomputer. This was a small on-line microcomputer which was used to reject events of no interest which had passed the earlier trigger levels. Specifically, any calorimeter cell which gave a trigger was examined more closely to verify that a shower with pt > 1.5 GeV/c had indeed been seen. MICE used a simple algorithm to do this and if no such shower was seen the event was rejected. (Trigger 4 events were not passed through MICE and were dealt with separately.)

2.12 Beyond the Trigger: the Data Aquisition System.

The experiment used two VAX 11/780 computers for recording data and running monitoring programs to check detector performance during data-taking. Events not vetoed by MICE were written to tape by the main VAX computer. The data recorded on tape for each event was;

1) the calorimeter ADC and TOF information;
2) the results from the MICE filtering program;
3) the calorimeter trigger and CEDAR information;
4) the digitisings from the Omega Prime chambers.

It took $\sim$ 4 hours to fill a magnetic tape with approximately 15000 events.

2.13 The Magnetised Iron and the Muon Hodoscopes.

A significant problem which the experiment encountered were muons travelling parallel to the beam line at distances of approximately one metre. These muons could simulate direct photon showers at the calorimeter and became known as the 'muon halo'.

Many software routines were written into the analysis to identify muon-induced events, and for the 1985 run simple electromagnets (10 tonnes of iron with coils around them) were positioned around the beam about 100m upstream of the detector assembly in an attempt to deflect the muons before they reached the calorimeter. Though the available current through the coils was not enough to deflect the muons away from the calorimeter entirely, it did shift them across the calorimeter. This was useful as a check for showers tentatively identified as being caused by the muon halo. The 'magnetised iron' was left in place for the '86 run.

Despite these measures, the muon halo was still a large source of background and for the experiment's final run in 1986 four 2m x 2m muon hodoscopes were installed. They were positioned in two pairs upstream of the Omega spectrometer. Space was limited here and the lower pair had to be mounted 2m further upstream than the upper pair (fig. 2.11).

Each hodoscope was composed of 15 (3x5) scintillator cells. These were set in coincidence with the trigger cells of the calorimeter, the intention being to identify muon showers explicitly. No online vetos were made, the hodoscope information being decoded and used later during the analysis.

Chapter Two Figures.

Figure 2.1 Layout of WA70 Apparatus.

Figure 2.2 Cutaway diagram showing construction of a ring image Cerenkov counter (CEDAR) as used by WA70.

Figure 2.3 Isometric view of calorimeter, showing configuration of segments and orientation of coordinate system.

Figure 2.4a and b Diagrams showing how the postions of showers on the calorimeter are determined.

Figure 2.5 Example of shower distribution on calorimeter for a real event.

Figure 2.6 Calorimeter construction in detail.

Figure 2.7 Distribution of wide and narrow channels throughout the calorimeter.

Figure 2.8 Diagram showing how the scintillator tubes are linked to the photomultipliers via light guides.

Figure 2.9 Schematic diagram of the laser system.

Figure 2.10 The source path in the polypropylene sheet.

Figure 2.11 Positions of additional apparatus for '86 data-taking run:

a) The A3 and A4 counters.

b) Magnet installed behind calorimeter.

c) Muon halo counters.

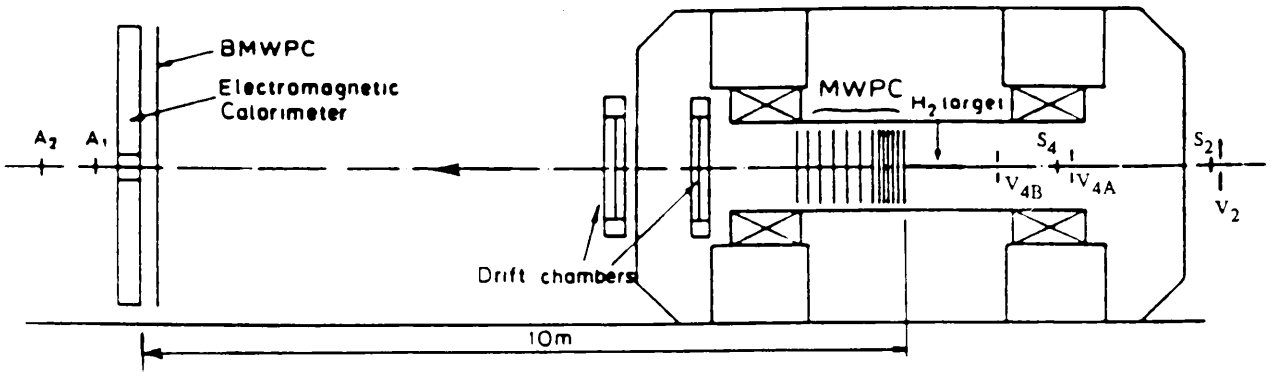

Figure 2.1

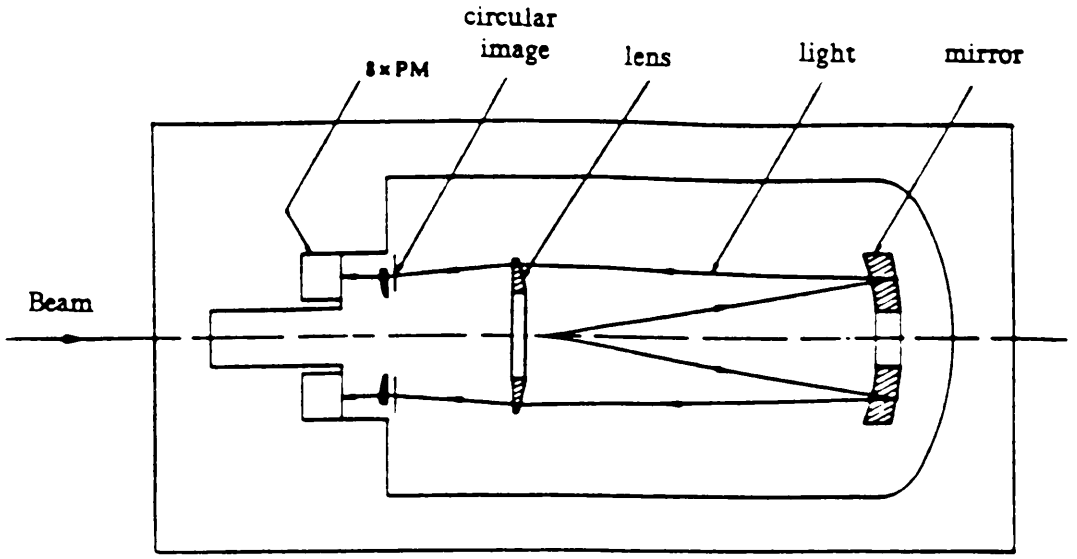

Figure 2.2

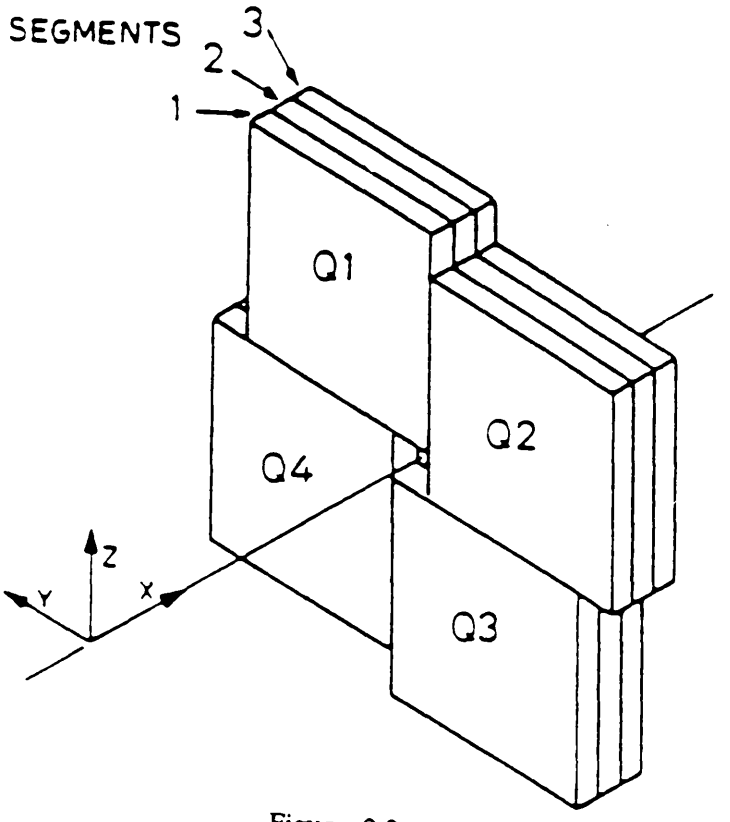

Figure 2.3

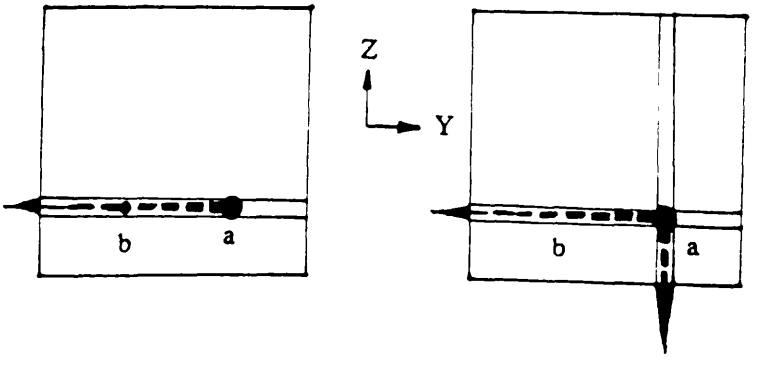

Figure 2.4a

2.4b

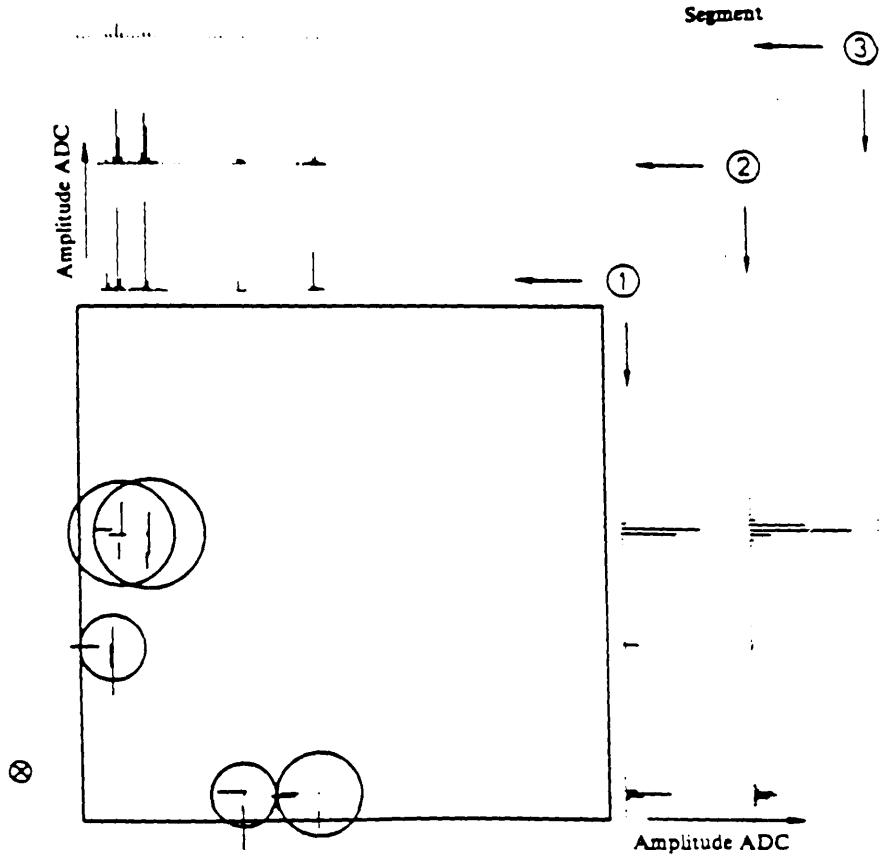

Figure 2.5

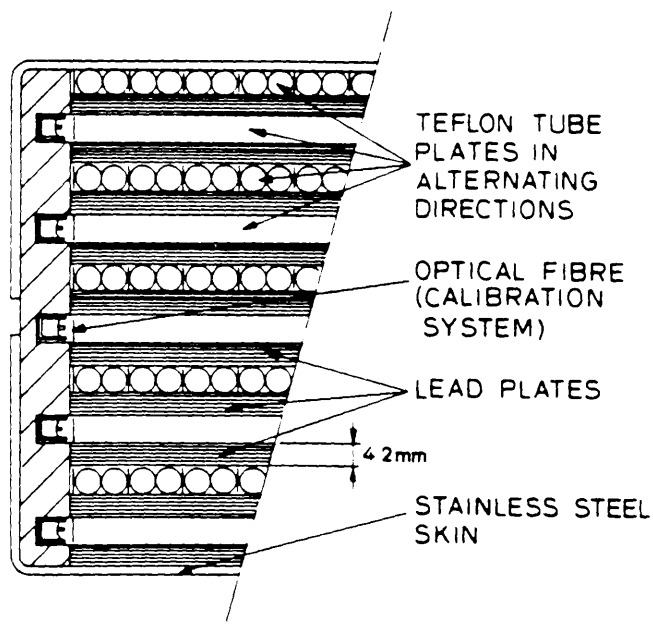

Figure 2.6

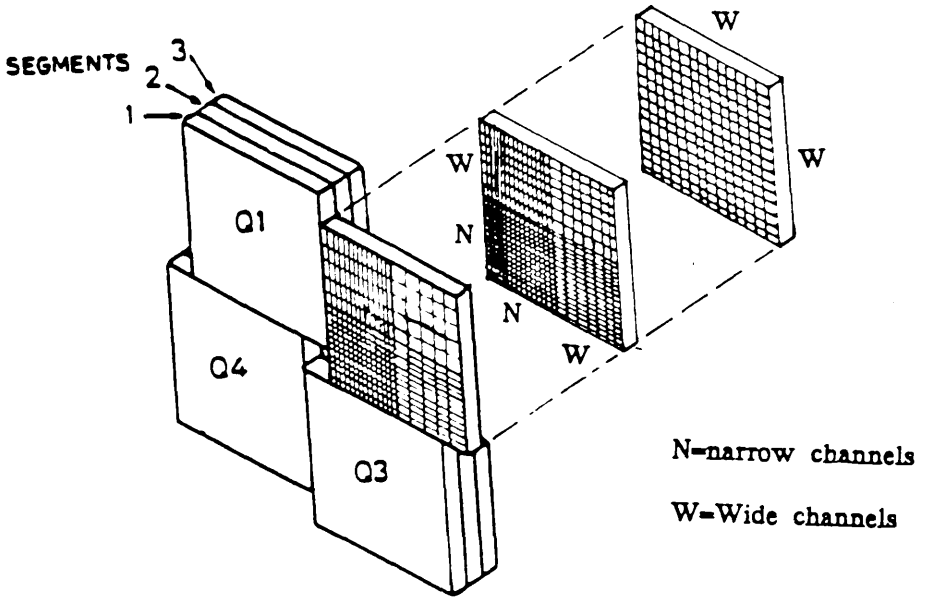

Figure 2.7

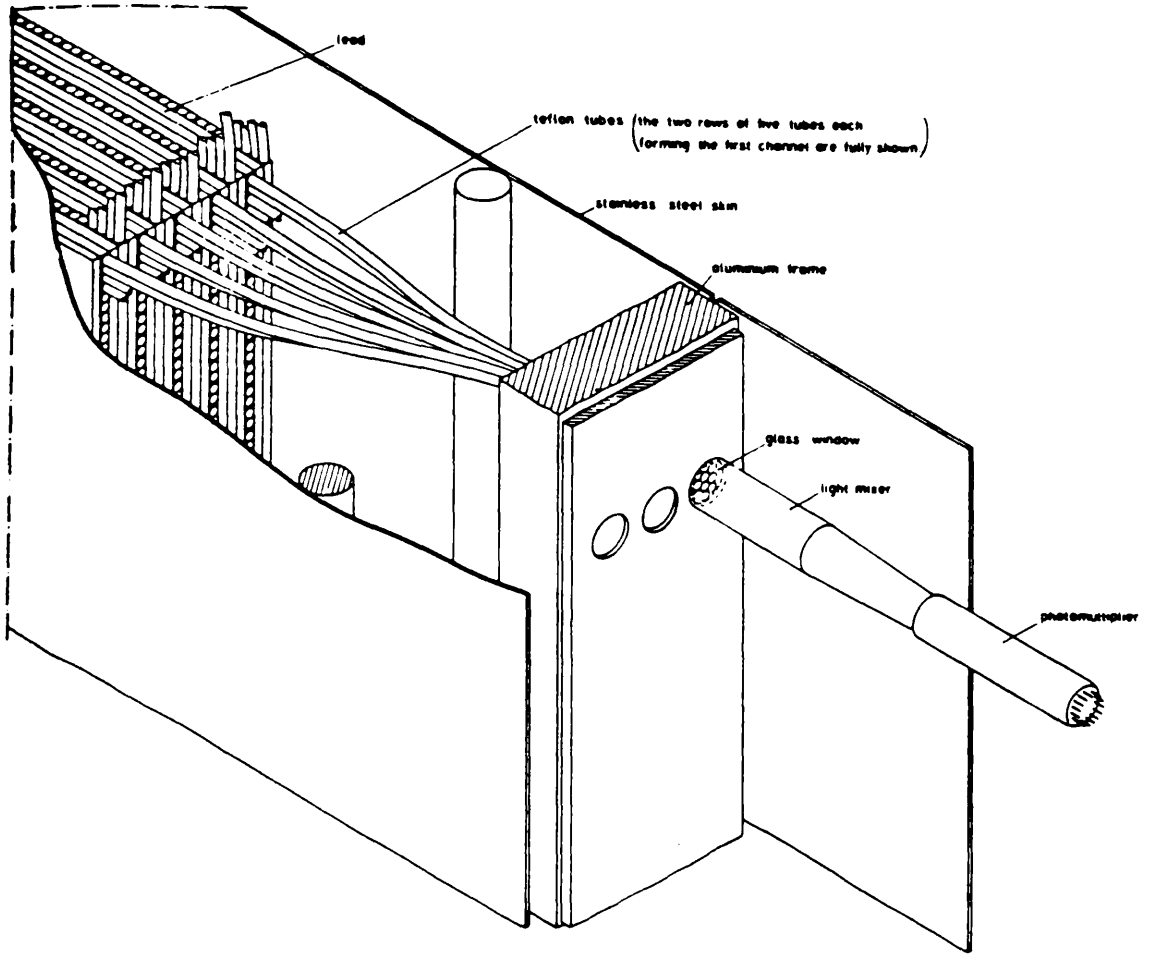

Figure 2.8

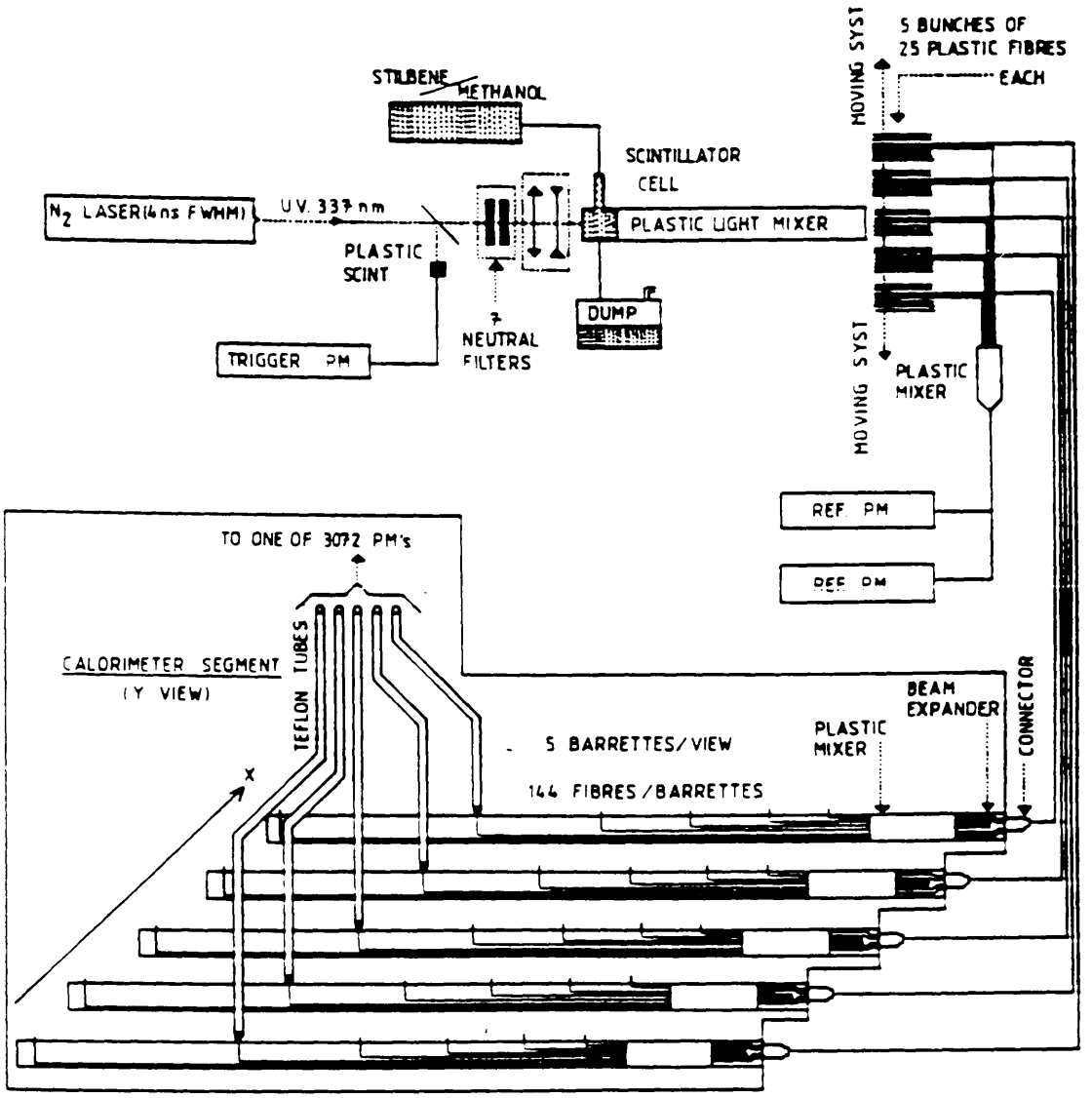

Diagram of the laser light injection and distribution system.

Figure 2.9

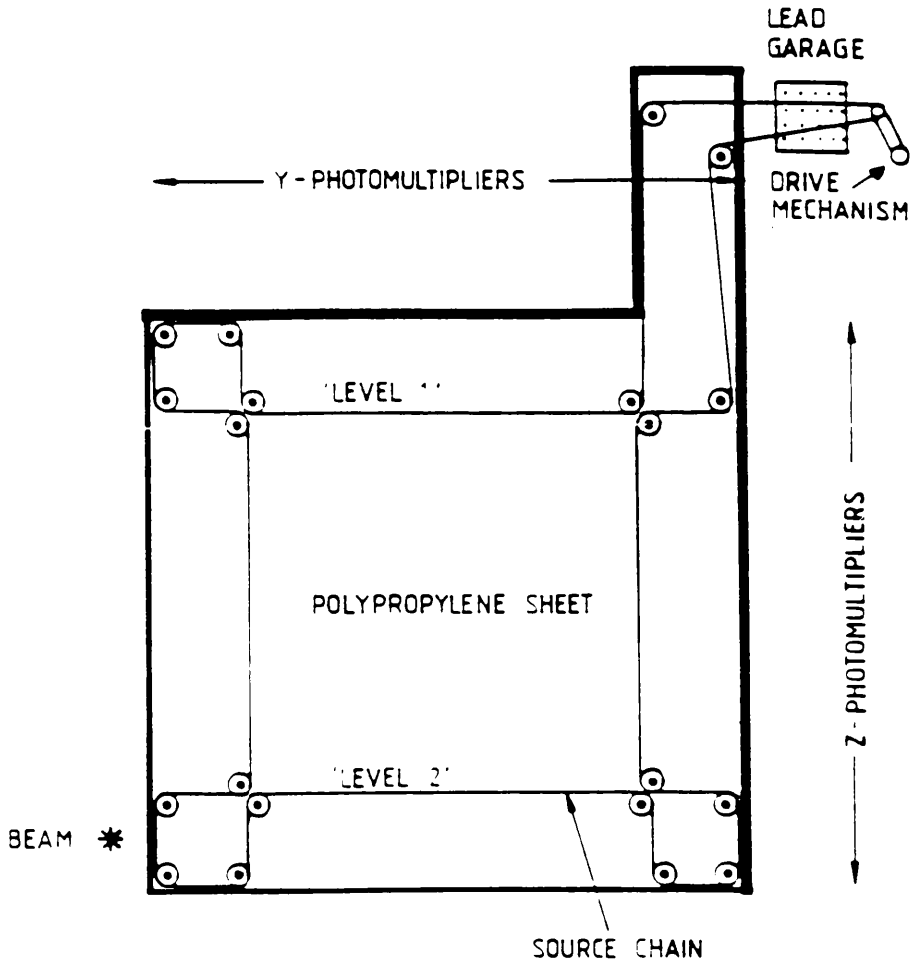

Diagram of source sheet showing source path geometry.

Figure 2.10

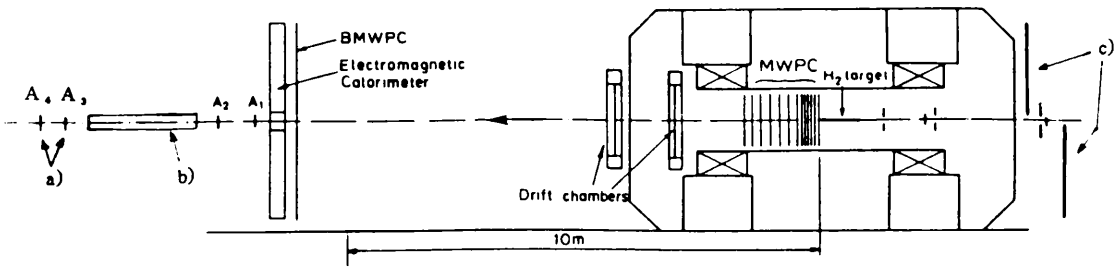

Figure 2.11

CHAPTER 3

Chapter 3. The Utility Computer Programs.

In this chapter the 'utility' programs used in the analysis of the data are described. These were;

1) GLOBAL: this program reconstructed the pattern of showers on the the calorimeter from the photomultiplier signals,
2) TRIDENT: the program which analysed the wire chamber data inside the Omega's magnetic field for charged tracks, and
3) LUND: the Monte Carlo program used to generate simulated events for use in computing efficiencies, backgrounds etc. Also described are the programs used to convert these events into realistic data, i.e. simulating their appearance in the detector.
4) OMGEANT: the program used to simulate the Monte Carlo data in the wire chambers, and
5) TWISTER: a specialised Monte Carlo used to produce events with two high pt particles.

3.1 The GLOBAL Program

As described in section 2.4, a shower hitting the calorimeter was recorded as two sets of ADC readings on the y and z axes. Reconstructing the position of one isolated shower was straightforward, but reconstructing the positions of several showers on the face of a quadrant caused by the same event was more difficult - on average there were 17 showers across the whole calorimeter per event. Several

low energy ADC peaks in the same event could lead to ambiguities, usually because of uncertainties introduced by merged ADC peaks.

A program named 'PATREC' was used for shower reconstruction in the analysis of the 1984 data, but it was later superseded by the 'GLOBAL' program. The '84 data was reprocessed using GLOBAL, and it was used throughout the '85 and '86 analyses. PATREC did not have the advanced ADC peak matching methods present in GLOBAL.

GLOBAL looked at the calorimeter information from an event quadrant by quadrant, using the ADC and TDC readings from each to reach the best 'hypothesis' for the shower positions across the quadrant.

GLOBAL's first step was to check for showers which lay along vectors which intersected or came close to intersecting the target in the same view of all three of a quadrant's segments. Using this information large peaks with suspiciously flat distributions lying along these vectors were re-examined with the possibility of overlapping peaks in mind. This process is illustrated in fig. 3.1.

Generally, peaks closer than 5cm were also checked for possible coalescence (a small shower in the vicinity of a large one, however, was treated as a statistical fluctuation). The corrected ADC profiles were then passed on to the later stages of GLOBAL.

The next step was to pair the ADC profiles in each view. This was relatively straightforward when a shower was isolated or originated from an electron or photon with momentum greater than 20 GeV/c, but in practice this was not often the case. Showers were often of low energy, or badly defined. To deal with cases like these on a large scale a numerical algorithm was developed, which used all the available information about the ADC peaks, namely

a) the peak sizes, E,

b) their longitudinal development X_y or X_z, where

$$X_y = \Sigma(X_{yi}\ A_{yi}) / \Sigma A_{yi},$$

A_i being the ADC of segment i.

c) the TOF information associated with them,

d) and their y or z position.

The basic procedure was to link showers for which the quantities listed in a), b) and c) matched, using a χ^2 formula to find the best pairing. χ^2shower was defined as;

$$\chi^2\text{shower} = \chi^2E+\chi^2X+\chi^2\text{TOF},$$

where $\chi^2E = (E_y - E_z)^2/\sigma^2E$,

$\chi^2X = (X_y - X_z)^2/\sigma^2X$ and

$\chi^2\text{TOF} = [(\text{TOF}_y\text{-Z}) - (\text{TOF}_z\text{-Y})]^2 / \sigma^2\text{TOF}$.

The σs were dependent on the energy and configuration of the shower, and were determined by experiment during testing.

Each ADC peak was compared with 1,2 or 3 distinct peaks from the opposite Z or Y view, the two which gave rise to the lowest χ^2shower being paired. If the lowest χ^2shower obtained was too high, the peak was rejected altogether.

Rather than process individual showers, the χ^2shower for one set of pairings made in a quadrant are added together and considered as a whole 'hypothesis', and the χ^2shower minimised. The best hypotheses (up to 30) are stored and then subjected to an algorithm which examined unallocated ADC signals to check their validity (on average 6% of the total ADC signal was unallocated). The hypothesis with the lowest χ^2shower was rejected in favour of another in only 4% of cases.

In 24% of quadrant reconstructions only one sensible hypothesis was reached, 15% had 2 hypotheses, 11% had 3, and 50% had 4 hypotheses or more. In 95% of hypotheses the trigger shower was reconstructed uniquely.

Having decided which hypothesis was most likely, the x and y positions of the paired peaks could then be used to calculate the position and energy of the original showers.

Fig. 3.2 shows the shower reconstruction efficiency for showers of varying energies, for both the best hypothesis and all hypotheses considered together.

The reconstruction process followed by GLOBAL is illustrated as a flow chart in fig. 3.3.

A study was made of how GLOBAL affected the π^0 efficiency, using data generated by the LUND Monte Carlo [41]. When analysis programs were run on quadrant reconstructions provided by GLOBAL's first hypothesis, 94.8% of generated π^0s were found. In events which GLOBAL had processed fully 96% were present. It should be borne in mind here that not all π^0s decay to two photons - 1.2% do not. Of all $\pi^0 \rightarrow \gamma\gamma$ decays, therefore, GLOBAL reconstructs both photons correctly in 97.2% of cases.

3.2 The TRIDENT Program.

The TRIDENT program [42] [43] has been used by many experiments at the Omega spectrometer to calculate charged particle directions and momenta, and to find interaction vertices. In its WA70 version it made use of digitisings from the wire chambers including the 4m x 4m MWPC.

(A flow chart showing the steps taken by TRIDENT is shown as fig. 3.4.)

In the innermost A and B chambers (see the description of the Omega

spectrometer in section 2.3) digitisings are numerous, making track reconstruction there difficult. (If there are too many digitisings in any plane or if the average number per plane in any event is too high, it is rejected. This will partly remove overlapping events.) TRIDENT tries to find aligned digitisings in the less crowded MWPC, butterfly and drift chambers first, and then extrapolates these into the inner chambers.

Initially, the y plane digitisings in the butterfly chamber and the MWPC are examined for hits lying along straight lines pointing to the target (within errors). These lines were used to define 'roads' - slices in the z-direction - in the two chambers which were then searched for z plane digitisings. These were analysed for 'space points' which could be combined to form 'preliminary tracks'. Next, TRIDENT extrapolates these tracks to the A and B chambers and allocates digitisings to them. The digitisings which remain after this are then examined for possible further tracks, as follows;

1) The y plane digitisings in the A chamber furthest from the target were extrapolated into the next chamber upstream using simulated data to predict the likely track direction. If a digitising was found in the predicted position the extrapolation was continued into the next chamber and so on. If aligned points were found in 3 of the 4 chambers it was passed as a track.

2) The U and V planes were examined for digitisings which were compatible with the y plane digitisings. If the z-coordinates of these lay in a line they were included in the track.

When all the chambers had been searched using this procedure, a fit was performed to derive the track parameters (a quintic spline was used to evaluate the track's momentum).

If TRIDENT could reconstruct no tracks in an event, or if there were no tracks

with more than 8 space points, the event was rejected.

TRIDENT then used the tracks to find the primary vertex in the interaction. Each found track was described by a helix, and the cylinders contained by these helices were extended back into the target from the track point furthest downstream. These cylinders in turn produced circles in the x,y plane which were tested in pairs to see if they overlapped in a fiducial volume within the target.

TRIDENT then looked for groups of these intersections, using the absolute distance between them and also the distance normalized by the error in position of an intersection region.

When a vertex candidate had been found a least-squares routine was employed, using the helical track equations as constraints, to determine its acceptability. If the χ^2 was too high, the track with the highest contribution to the χ^2 was dropped and the calculation performed again.

When a vertex was accepted, the tracks in the event which had not been used to find it were checked to see if they could be reasonably traced to it. Those which did not pass within a certain distance of the vertex, allowing for the error in the track direction, were rejected.

3.3. The LUND Monte Carlo Program and the Detector Simulation.

Monte Carlo programs (MC's) have become an essential tool of particle physics and are used to calculate acceptances, efficiencies etc. They do, however, have limitations. The Lund Monte Carlo [44] [45], used by WA70 to simulate direct photon events, contains the matrix elements for the relevant QCD subprocesses to second order but the cross sections it produces, even assuming the theory to be largely correct, are dependent on inexactly known constants. Indeed, one of the purposes of WA70 was to measure some of these constants more accurately. We

must accept, therefore, the possibility of systematic errors caused by inaccuracies in the Lund and this is discussed in section 5.9.

3.3.1 The Physics Assumptions in the LUND Program.

The program must make physics assumptions at more than one level; over and above the parton subprocesses dealt with by the Standard Model of the strong and electroweak forces, structure functions, elastic and diffractive scattering and hadron fragmentation must be considered. This last is important for WA70, focussing as it does on jet production under QCD, and is dealt with in more detail below.

The distribution of momentum amongst the partons inside baryons cannot at present be predicted entirely from theory and experimental data must be used to derive them. The structure functions for nucleons are consequently more easily obtainable than those for charged pions as appropriate experimental data for the former is more abundant. In both cases the quark structure function is better understood than that for the gluon, which is more sensitive to differences in scaling. The nucleon stucture functions used in the LUND MC were derived from study of deep-inelastic lepton-nucleon scattering, high mass dilepton production and the production of massive particles such as the J/Ψ and the Υ [46]. For charged pions the Owens 'set I' structure functions were used [47]. These were calculated using data on J/Ψ and dimuon production. The WA70 experiment itself obtained information on the gluon structure function for the nucleon (see below section 6.2).

Another important systematic error which the Lund contains is the value of Λ used in the expression for α_s (Q^2) (equation 1.1). This can be set by the user of the program. WA70 used a value of Λ = 200 MeV.

3.3.2 Fragmentation.

When partons leave the interaction vertices they fragment into the hadrons which are eventually seen by the detectors. The fragmentation occurs at an energy too low to be treated by perturbative QCD, and therefore must be simulated in some other way. The 'Lund string model', specially written for the program, was used. It assumed that QCD is linearly confining at large distances, and has been checked by comparison with data from JADE.

3.3.3 Event Generation.

In the 'engine room' of a Monte Carlo devoted to high pt physics are the matrix elements of the simple 2 → 2 subprocesses. The cross-sections of these, when convoluted with the structure functions (see above), form the total cross section for the subprocess. In the version of LUND used by WA70, namely PYTHIA version 4.2, nine second order subprocesses were used. They were;

1) $q(i)q(j) \rightarrow q(i)q(j)$
   $q(i)\overline{q(j)} \rightarrow q(i)\overline{q(j)}$
   $\overline{q(i)}\overline{q(j)} \rightarrow \overline{q(i)}\overline{q(j)}$
2) $q(i)\overline{q(i)} \rightarrow q(j)\overline{q(j)}$
3) $q(i)\overline{q(i)} \rightarrow g\ g$
4) $q(i)\ g \rightarrow q(i)\ g$
   $\overline{q(i)}\ g \rightarrow \overline{q(i)}\ g$
5) $g\ g \rightarrow q(i)\overline{q(i)}$
6) $g\ g \rightarrow q\ q$
7) $g\ g \rightarrow q\ q$ (differing string configuration from 6)
8) $q(i)\overline{q(j)} \rightarrow g\ \gamma$
9) $q(i)\ g \rightarrow q(i)\ \gamma$
   $\overline{q(i)}\ g \rightarrow \overline{q(i)}\ \gamma$

The problem of any MC is to generate unbiased events in accordance with the cross-sections of the subprocesses above. This is achieved in the Lund by a sophisticated weighting technique in which the most populated regions of phase space are sampled most frequently.

We will now examine how the program works in some detail. There are three main sections.

In the first section, the user specifies the type of events to be generated, the beam and target particles, $\sqrt{s}$, Λ, beam angles, which set of structure functions to be used, and the parameter QTMIN which specifies the lower limit of the pt range. It is also possible to suppress one or more of the subprocesses listed above, and this facility was used to full advantage by WA70. It will be noticed that direct photons are only produced by subprocesses 8 and 9, while the main background to the direct photon signal, misidentified π^0s, are almost exclusively products of the other seven. For convenience, the two classes of events were generated seperately by suppressing subprocesses 1-7 or 8 and 9. Not only did this arrangement simplify the calculation of direct photon and π^0 efficiencies, it maximised the number of events which could be generated with the CPU time available on the computer at Glasgow, an IBM 4361.

Studies at Glasgow by A. Maxwell [46] showed that the distribution of events in pt is not realistic for direct photons below a pt of QTMIN + 0.7 GeV/c. To obtain a reliable sample of direct photons in the pt range above say 3.7 GeV/c, QTMIN had to be set at 3.0 GeV/c. The distribution of direct photon transverse momentum in events generated at QTMIN = 3.0 GeV/c is shown as fig. 3.5a. However, as fig. 3.5b shows, π^0 events generated at QTMIN = 3.0 GeV/c were found to have a realistic pt distribution almost immediately above QTMIN. Generating both types of event simultaneously would have necessitated the generation of many π^0 events with a pt below the range of interest.

Additionally, the yield of direct photon events among the other 'background' events was low, and an imbalance towards the latter would have been caused.

The main loop which generates the event is contained in the second section. On average, the time taken to generate a direct photon event (with QTMIN=3.0 GeV/c) was 4200 ms. A background event took 3360 ms. To increase the number of events each event was 'rotated' in the centre of mass to produce a further two events. This allowed a tripling of statistics for a comparatively small amount of CPU time. Later in the analysis the amount of MC events available proved to be the critical limitation.

In the third section the histograms displaying pt distribution etc. are filled, and the events are written out.

For the raw Monte Carlo events to be turned into simulated data, we must simulate their effect on the detector. The space points in the Omega wire chambers and the MWPC are generated by the OMGEANT program (see below). The calorimeter simulation, however, is incorporated within the Lund MC itself. In this, the events are processed one at a time. First, each event is given a vertex and the tracks of the produced particles are extrapolated to the calorimeter. Though the inner detectors are not simulated in any way, allowance is made for the photons etc. to be absorbed or converted before reaching the calorimeter. If they are not, the shower development in the three segments is calculated using figures for radiation length, absorption coefficients etc. given to the program. Having simulated the shower development the signals at the photomultipliers are calculated, and the TOF signals can also be calculated.

The PM'S on the real detector have a range of gains and their signals must be corrected using a file containing their relative gains ('the source file'), as measured by the source system. To ensure close simulation to real data the PM gains used in the Lund were multiplied by the (inverted) numbers in the source file and

then corrected using the same file, having allowed for ADC inaccuracies.

Having reproduced an event as it would be seen at the calorimeter, the event was passed to a simulated calorimeter trigger, and if it passed this, it was passed though GLOBAL. The absolute energy scale of the MC data was checked by comparing the difference between reconstructed photon showers and their generated energies. The energy scale was adjusted until these two (averaged) quantities matched to within 1 part in 1000. The mass of the π^0 was also measured in the MC data and found to be 134.5 $\mp$ 0.5 MeV/c^2, which matched with the expected value of 135.04 MeV/c^2. The events were then passed to OMGEANT.

3.4 The OMGEANT Program.

The OMGEANT Monte Carlo [47] simulates the WA70 detectors nearest to the target, i.e. the drift chambers, wire chambers, lever arm chambers etc. The region simulated includes the space up to the 4m chamber. The purpose of OMGEANT was to simulate the response of the inner detectors to the Lund-generated charged tracks passing through them. Digitisings were allocated to each track taking into account the efficiencies of each plane of these chambers and the absorption coefficients of the materials used in them. The Monte Carlo event having been fully tracked through the detector, the events are passed to the TRIDENT program in a form known as DST1.

The DST1 tapes are now passed to TRIDENT where they are processed exactly as real data. This involved the data being subjected to some halo cuts. Clearly, there can be no halo contamination in the Lund generated data, but the cuts were kept in to allow a measurement of the number of events rejected incorrectly.

The Monte Carlo events used in the main analysis were not generated by the author. Instead, the large number of events which already existed at Glasgow were used, though these events had been produced using the '85 hardware trigger. CPU

time permitting, reprocessing the raw Lund tapes through a simulation of the '86 trigger would have been desirable, particularly in view of the threshold in this trigger which rendered the collected direct photon data below 4.5 GeV/c unreliable. This may have been (partially) rectifiable using a large sample of Monte Carlo events put through an '86 trigger.

Reprocessing the 219,000 events involved would have been a large task bearing in mind that OMGEANT and TRIDENT took 4-5 times as long to process an event as Lund takes to generate it. On balance, it was thought that as the region of the trigger problem (4-4.5 GeV/c) had been well covered by the runs of 1984 and 1985, the existing '85 trigger Monte Carlo data could be used in the '86 analysis (the '85 trigger, which proved reliable at 4 GeV/c, would have no effect above 4.5 GeV/c). The main purpose of the 1986 run was improvement of statistics in the upper pt bins. This problem was independent of the double pt event trigger desribed in Chapter 7.

The number and type of Monte Carlo events used in the efficiency and background calculations of chapter 5 was as follows;

Direct Photon events, QTMIN=3.0 GeV/c	105,457
π^0 events (background) QTMIN=3.0 GeV/c	98,503
π^0 events (background) QTMIN=4.5 GeV/c	15,194

3.5 The 'Twister' Monte Carlo.

The version of the Lund MC described above, PYTHIA 4.2, does not include the matrix elements for the subprocesses $q\bar{q}\rightarrow\gamma\gamma$ or $gg\rightarrow\gamma\gamma$. For a study of the background to the double direct photon signal and its detection efficiency, a large sample of high pt double direct photon events was required. High pt $\pi^0\pi^0$,$\gamma\pi^0$ and $\pi^0\gamma$ events, the largest source of background, will also be needed. To generate

this type of event a later version of PYTHIA, the program TWISTER 1.2 [44], was used. This version of the Lund includes the double direct photon subprocesses named above as well as many other higher order subprocesses. Also included are several higher twist processes. The drawback with generating events with two high pt products is that it is very time-consuming. Had TWISTER been run on the Glasgow IBM 4361 only 1 event per hour would have been obtained. Generating a useful number of events was therefore unrealistic. Fortunately, the University of Geneva had access to an IBM 3090 computer which is 80 times faster than a 4361. After many hours of CP time on this, several tapes of double high pt MC events were produced as detailed below.

Event type	number of events (tapes).
$\gamma\gamma$	18600 (1)
$\gamma\pi^{\circ}/\pi^{\circ}\gamma$	47926 (3)
$\pi^{\circ}\pi^{\circ}$	14170 (1)

Chapter Three Figures.

Figure 3.1 Idealised example of merged peaks reconstruction.

Figure 3.2 Reconstruction efficiency of single showers, for both the best hypothesis only (a), and for all hypotheses considered together (b).

Figure 3.3 Flow chart for GLOBAL reconstruction program.

Figure 3.4 Flow chart for TRIDENT reconstruction program.

Figure 3.5a Pt distribution of Lund direct photon events, QTMIN=3.0 GeV/c.

Figure 3.5b Pt distribution of Lund π^0 events, QTMIN=3.0 GeV/c.

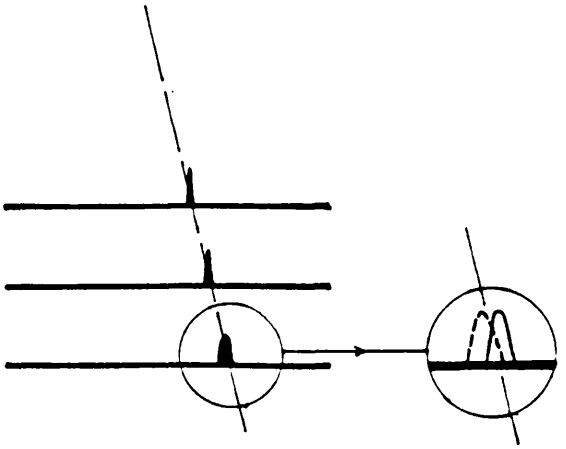

Figure 3.1

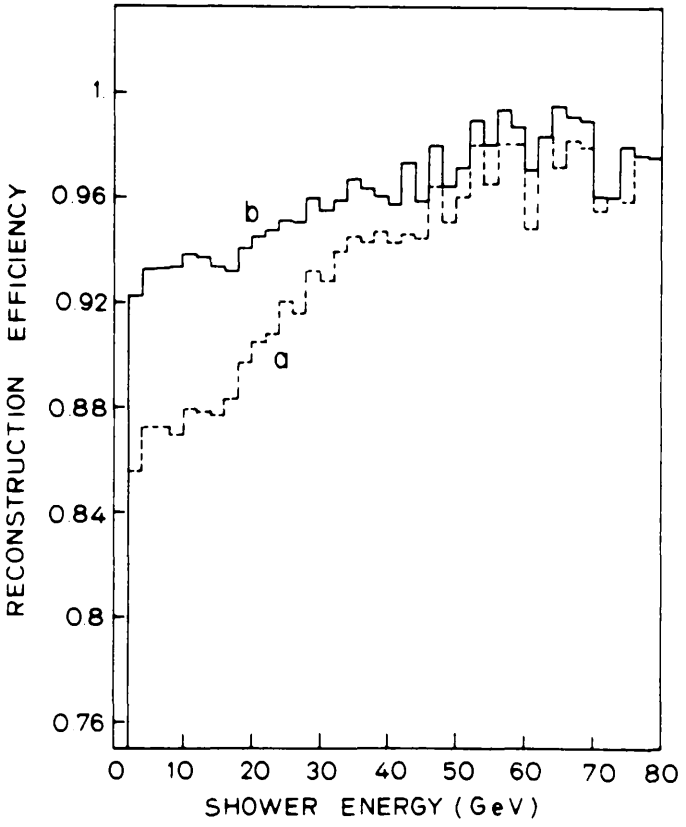

Figure 3.2

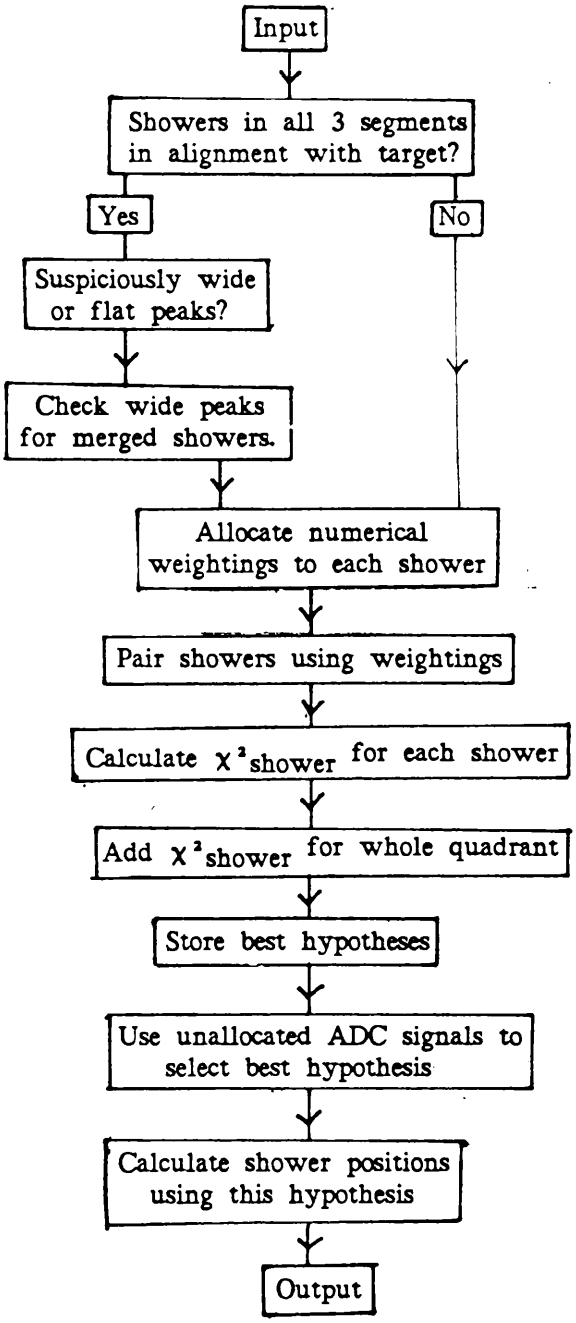
Input
Showers in all 3 segments in alignment with target?
Yes
No
Suspiciously wide or flat peaks?
Check wide peaks for merged showers.
Allocate numerical weightings to each shower
Pair showers using weightings
Calculate χ^2_{shower} for each shower
Add χ^2_{shower} for whole quadrant
Store best hypotheses
Use unallocated ADC signals to select best hypothesis
Calculate shower positions using this hypothesis
Output

Figure 3.3

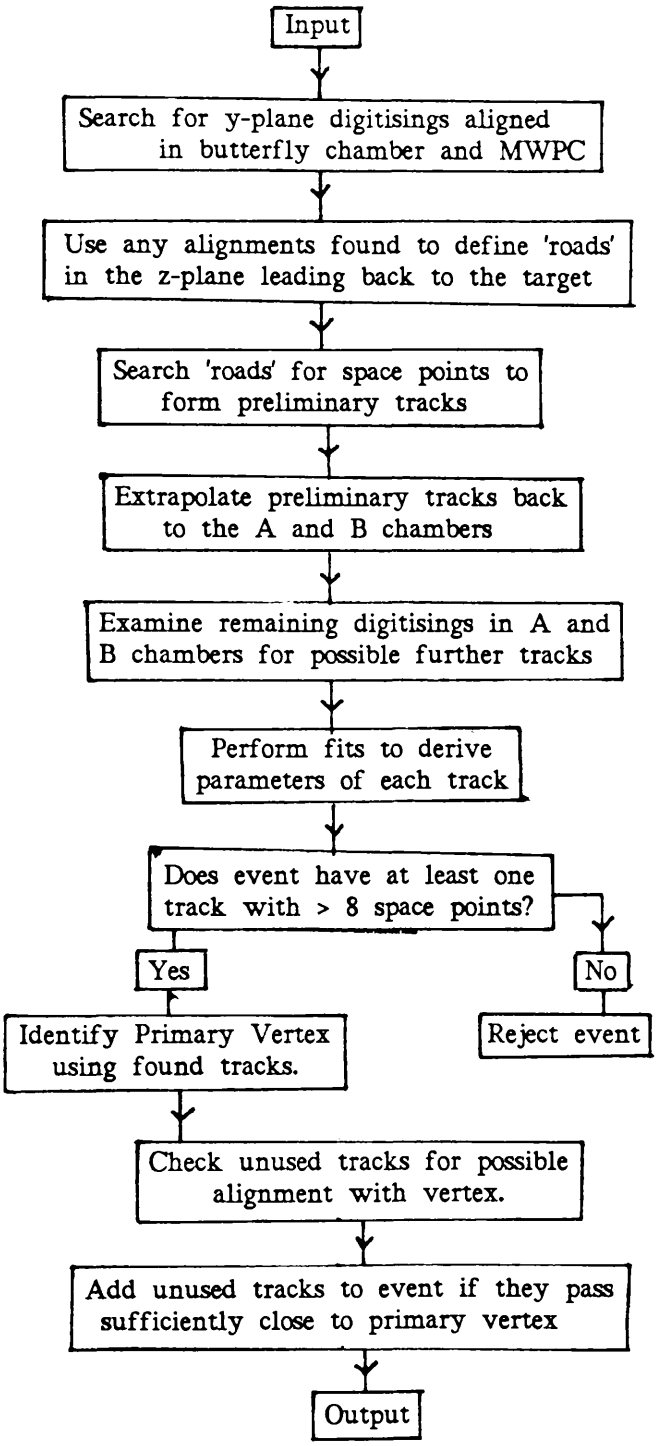
Input
Search for y-plane digitisings aligned in butterfly chamber and MWPC
Use any alignments found to define 'roads' in the z-plane leading back to the target
Search 'roads' for space points to form preliminary tracks
Extrapolate preliminary tracks back to the A and B chambers
Examine remaining digitisings in A and B chambers for possible further tracks
Perform fits to derive parameters of each track
Does event have at least one track with > 8 space points?
Yes
No
Identify Primary Vertex using found tracks.
Reject event
Check unused tracks for possible alignment with vertex.
Add unused tracks to event if they pass sufficiently close to primary vertex
Output

Figure 3.4

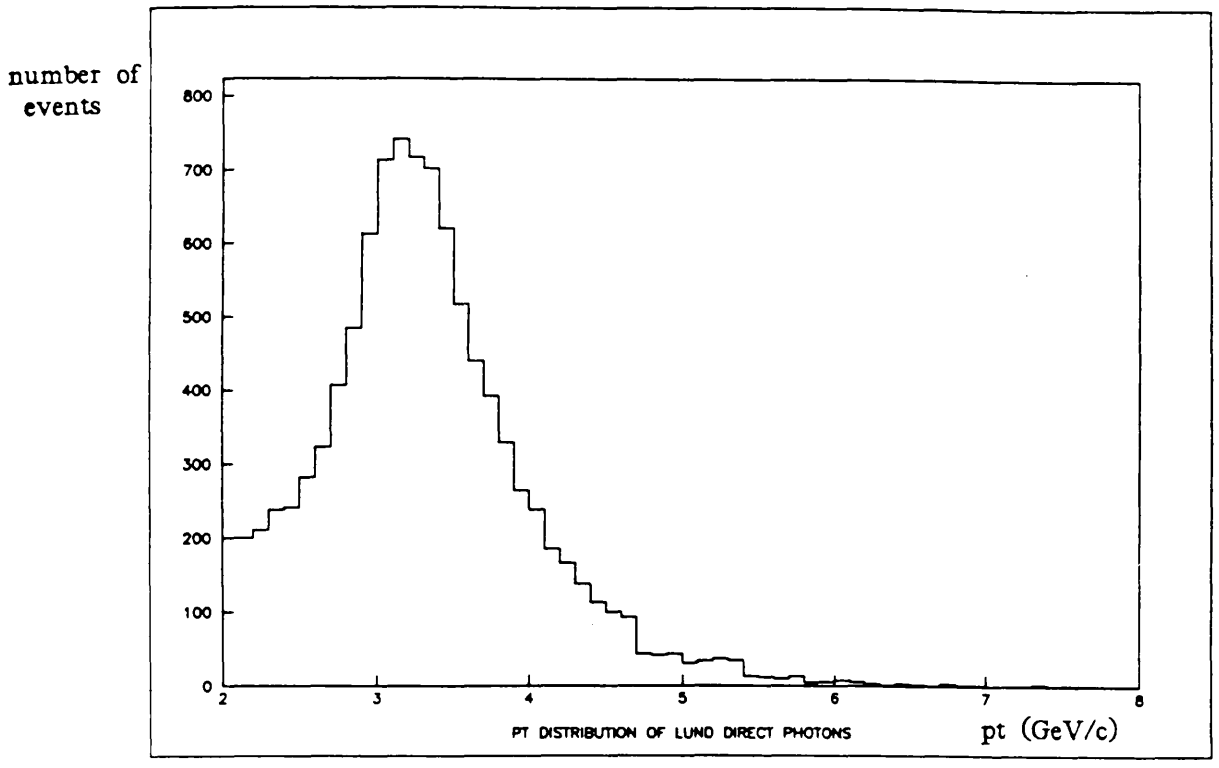

Figure 3.5a

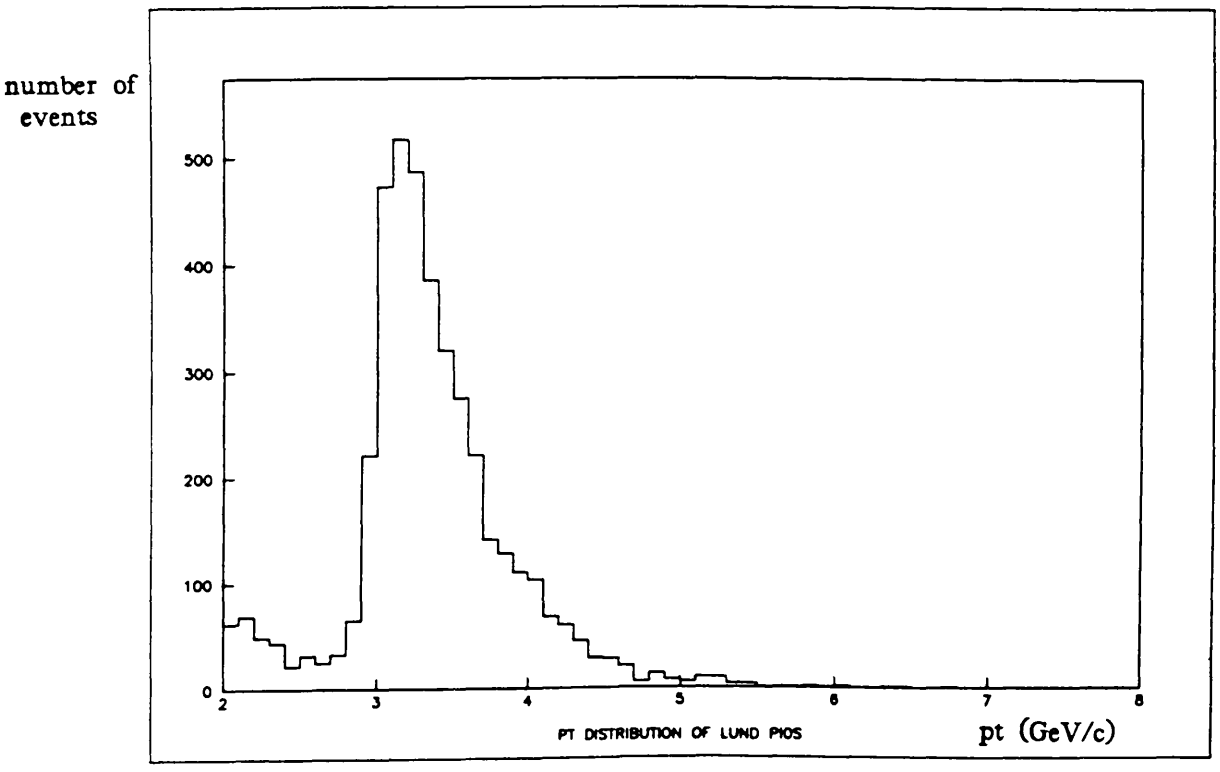

Figure 3.5b

CHAPTER 4

The Data.

This chapter outlines how the events which have survived the various trigger levels are analysed for direct photons, π^0s and ηs.

4.1 Pt and xf distributions.

The distribution in transverse momentum (pt) of the trigger showers from 321827 events is shown in fig 4.1 (trigger showers which were below the first pt cut described below or which were identified as hadrons are not shown). Statistics were large at a pt of 4 GeV/c, but by 7 GeV/c they had fallen considerably and above this the triggers were due largely to the muon halo (see below). Statistics as a function of xf were highest in the region between -0.45 and +0.45, and significant numbers of events were present out to an xf of $\mp$1.0 in the lower half of the pt range. Above a pt of about 5 GeV/c however, the outer xf bins were largely empty.

Geometrical factors affected the acceptance of the calorimeter for direct photons and π^0s at high and at low xf. In the region of xf $\sim$ -1.0, incident particles struck the calorimeter towards its outer edges, with a correspondingly higher chance of one or more photons from a $\pi^0 \rightarrow \gamma\gamma$ or $\eta \rightarrow \gamma\gamma$ decay missing the calorimeter. As the remaining photon may satisfy the cuts for a direct photon, this will increase the direct photon background as well as lowering the π^0 and η detection efficiencies. At very high positive xf a similar problem arises as one of the decay photons may pass through the central beamhole and not be detected.

Another problem limiting π^0 and η efficiency was that showers produced by two photons striking the calorimeter close together may not be resolved, leading to a π^0 or η being misidentified as a single photon. This problem was largest for π^0s with positive xf.

The geometrical acceptance of the calorimeter for direct photons against pt and xf is shown in fig. 4.2. Direct photon acceptance varied from 40% at a pt of 4 GeV/c to 90% at 7 GeV/c.

Originally, the analysis was intended to be concentrated on the region 4.0 < pt < 7.0 GeV/c and -0.45 < xf < +0.55, but a problem affecting the data at the lower pt limit arose, similar to that encountered during the 1985 run. Though the hardware trigger had been set at 3.5 GeV/c in the 1986 run (see section 3.8), this was found to have been closer to 4.0 GeV/c when the data was analysed. The pt distribution of the events passed as direct photons by the analysis described below is shown in fig. 4.14a, and a shortfall in direct photon numbers in the lowest 4.0 -> 4.25 and 4.25 -> 4.5 GeV/c bins can be seen, particularly towards high positive xf. This problem forced the lower pt limit of the analysis to be raised from 4.0 GeV/c to 4.5 GeV/c.

Measurements of the direct photon and π^0 cross-sections (and the γ/π^0 ratio) for the pt range 7→8 GeV/c were made seperately from the main analysis.

4.2 The Data Sample.

After the raw data had been processed through the programs GLOBAL and TRIDENT approximately 200,000 events remained on 37 data tapes. This was equivalent to a cross-section sensitivity of 7.7 inverse picobarns.

4.3 Identification of Direct Photon and π^0 Signals.

The largest source of background to the direct photon signal was caused by π^0s and ηs decaying to two photons, one of which failed to be detected. This left an event containing a single photon shower. Calculating the size of this background and correcting for it was the most important part of the analysis.

A flow chart showing the layout of the analysis appears as fig. 4.3.

Before an event was examined for direct photons or π^0s, a series of preliminary cuts were applied. These are listed below.

1) If TRIDENT failed to find a vertex in the target (restricted to a cylinder of radius 2 cm stretching from x = -108.0 cm to x = 0.0 cm, the event was rejected. The distribution of the recontructed vertices is shown in fig. 4.4. The number decreases towards the downstream end due to the beam being slighly absorbed (3% in total) as it passes along the target. This was corrected for at a later stage of the analysis.

2) The highest pt calorimeter shower was found, and the event rejected if this had a pt < 2 GeV/c. This is low compared with the 4.5 GeV/c limit discussed above, but provision had to be made for π^0s and ηs with pts of 4 GeV/c which might decay into two electromagnetic showers both with pts of 2 GeV/c.

3) The highest pt shower in an event (which we shall call the 'trigger shower')was examined to determine whether it was electromagnetic or hadronic. This was done by measuring the fraction of the shower's total energy deposited in the third segment of the calorimeter (i.e. the furthest downstream). The calorimeter was 24 radiation lengths deep for photons, so they deposited most of their energy in the first and second segments. Hadrons, however, had a much lower interaction rate and 50% of hadrons striking the calorimeter passed through it without interacting. Those which did deposited their energy in all 3 segments. If more than

20% of a shower's energy was found in segment 3 it was classified as hadronic and the event rejected.

4) If the shower did not fall within the 'sensitive area' of the calorimeter the event was rejected. Showers in the area defined as being within 4cm of the inner quadrant edges and within 8cm of the outer edges were rejected. (Incident particles striking the calorimeter at the outer edge enter at a steeper angle than those closer to the beam hole.) This area was not insensitive as such, the problems being caused rather by the relatively steep angle and the danger of losing part of a shower at the calorimeter edge.

4.4 The Muon Halo Problem.

Before describing the direct photon and π^0 analysis, an important source of fake photon hits at the calorimeter must be described. Muons travelling parallel to the beamline caused problems throughout the data-taking. As time progressed however, the problem became better understood and several measures were taken to minimise it.

The muons were produced by mesons in the beam which decayed upstream of the target. Travelling parallel to the beam, they produced showers at the calorimeter by bremsstrahlung. The muons were travelling 2m from the beamline at the calorimeter position and often faked photons with very high transverse momenta, and it was an excess of high pt triggers which drew attention to the problem. After a careful study of this muon 'halo', it was discovered to be only a weak background in the middle pt range - 4-5 GeV/c - but a highly significant one at the upper end of the pt range, i.e. 6-7 GeV/c. Both hardware and software solutions were developed to combat the problem.

During the 1985 magnetised iron (described in chapter two) was placed 100m upstream of the target to deflect the muons away from the beam line, and for

the 1986 data taking period four muon hodoscopes were constructed by the University of Geneva to detect the remaining muons. Both these measures are described in section 2.13.

The most effective method for counteracting the problem proved to be software routines which used information from the time-of-flight system, the calorimeter and the BMWPC to identify showers caused by muons. The methods used in these routines are described below.

4.4.1 The Muon Halo Cutting Routines.

In the first two of these routines, which used information from the time-of-flight (TOF) system and calorimeter, two levels of cuts were imposed on the data. Level 1, the 'gentle' halo cuts, were intended primarily to remove most of the halo without removing many genuine direct photons. The intention of the 'strict' level 2 halo cuts was to produce as clean a sample of direct photons as possible, even if a proportion of the genuine direct photons were removed by them.

a) Calorimeter information.

As the muons travel parallel to the x-axis the showers caused by them in the 3 segments of the calorimeter will lie along vectors which do not intersect with or pass close to the target. To utilise this fact, a least squares fit was performed to the shower positions in the 3 segments and the vector obtained was projected back towards x=0. This was compared with a line from the target to the shower on the face of the first segment. If the shower-producing particle originated in the target these vectors should match (assuming it was not a charged particle), so if they were found to be further than 0.11 cm apart in space at a distance 1cm upstream from the face of the calorimeter (0.09 cm for the 'strict' cuts) the shower was classed as a halo shower and the event vetoed.

b) Time-of-Flight

For an event to be accepted, the TOF system had to detect a beam particle within ∓20 nanoseconds of the particle hitting the calorimeter. Since the problem muons are unconnected with interactions in the target the TOF signals associated with them should be spread evenly across the -20ns → +20ns range. This proved to be the case, and by examining the TOF signals more spurious triggers can be rejected. The parameter

$$DTOF = ((Y-Ty) + (Z-Tz))/2$$

was calculated, where Y and Z are the shower coordinates and Ty and Tz are the coordinates of the shower as predicted by the TOF. This quantity is plotted for all showers in the '86 data sample passing the requirements of section 4.3 in fig 4.5a and for the subset of these with an apparent pt greater than 8 GeV/c in fig. 4.5b.

(Extrapolating the direct photon trigger rate from low pt indicates that fewer than 10 genuine direct photon showers above 8 GeV/c could be expected, and the large number observed in this region can be almost entirely ascribed to muon halo-caused showers. We can use these triggers as a 'clean' sample of muon halo events.)

The difference in the two plots is clear. Showers with |DTOF| > 40cm (level 1) or 24 cm (level 2) were rejected as halo.

c) The 4m x 4m Big Multi Wire Proportional Counter.

A muon striking the calorimeter along a line parallel to the x-axis must pass through the 4m x 4m MWPC. If 2 hits were found within 2cm of such a track extrapolated back from a calorimeter shower the shower was flagged as a muon. However if both these hits involved the z-plane the shower was not vetoed, as the z plane had a lower efficiency than the other three planes [49]. This

was a small effect.

d) The Muon Hodoscopes.

As described in section 2.13, the hodoscopes were divided into 12 (3x4) cells per quadrant, and when a cell was fired the information was stored, rather than the event rejected out of hand. This permitted later off-line matching of showers on the calorimeter to cells in the hodoscopes. A routine to match these was written by R. Poultney of Liverpool [50] and incorporated into the Glasgow analysis programs.

At Glasgow a study was made of the relative effectiveness of the hodoscope routines and the TOF routines used previously. The standard single direct photon analysis procedure was run on a sample of 10950 events with either the old routines or the new hodoscope routine 'switched on' alternately, and with both routines 'switched on'. The results were:

Hodoscope routine on, 'old' muon halo routines off;	1968 events kept.
Hodoscope routine off, 'old' muon halo routines on;	1964 events kept.
Both routines on;	1962 events kept.

This implies that both routines are cutting almost exactly the same events. During the analysis, both routines were used.

The pt and xf distribution of showers flagged as muon halo is shown in figs. 4.6a and b, and their position on the calorimeter is shown in fig. 4.7. This distribution can be understood qualitatively; the charged muons will be deflected by the Omega field, though as most muons will have similar momenta they will be concentrated in one region of the calorimeter, specifically the upper, outer corner of quadrant 4.

4.4.2 The Efficiency of the Muon Halo Routines.

These Muon halo routines removed approximately 90% of the muon halo but also vetoed some events which contained genuine direct photons. A study of this problem was made at the University of Geneva [51], and the correction factors required, which vary with pt and xf, are shown in a 3-dimensional plot as fig. 4.8.

4.5 Identifying π^0s.

Having obtained a sample of events containing at least one photon with pt > 2 GeV/c, we can move on to the task of finding photon pairs with reconstructed masses within a specified range of the accepted π^0 mass. The reconstructed mass of the shower pair coming closest to this value in each event of the whole '86 data sample is plotted in fig. 4.9. The π^0 peak is pronounced above a linear background. Before a shower pair was accepted as a π^0, it had to pass several criteria, as described below.

Figure 4.10 shows the asymmetry A for all reconstructed photon pairs, where A is given by

$$A = |E_1 - E_2| / (E_1 + E_2),$$

where E_1 and E_2 are the energies of the two photons. This distribution should be flat but as can be seen there is a peak at high A. This background of highly asymmetric photon pairs is caused by direct photons of average energy (say 30 GeV) having reconstructed masses in the π^0 mass range by chance when combined with one of the many low energy photon showers in the calorimeter. Pairs with A > 0.90 were therefore rejected and the remaining π^0s corrected for the known loss of 10%.

In the analysis of the runs previous to 1986, much work was done on fitting the background under the π^0 peaks, particularly by Richard Lucock [52], who developed a fitting formula. Though this formula was used to calculate the background to π^0s found during a search for double direct gammas (see chapter 7), the increase in statistics for 1986 caused the importance of background when evaluating π^0 numbers to decrease. The π^0 mass peaks in each pt/xf bin were very tightly defined and the background could be subtracted by hand bin by bin. A sample reconstructed mass distribution for the range $4.5 < pt < 4.75$ GeV/c, $-0.05 < xf < +0.05$ is shown in fig 4.11, and it can be seen that the π^0 peak dominates the background in the region of interest (the limits of which were taken as 70 to 200 MeV/c^2). A linear background was assumed.

The raw numbers of π^0s found (after subtraction of this background) are shown in table 4.1. Though trigger problems forced the direct photon study to be confined to the region above pt = 4.5 GeV/c, they did not affect the π^0 signal. Statistics in the lower bins were high, while in the top 6-7 GeV/c bin, there were 183 entries, giving a $\sqrt{n}$ error of only 7%. The efficiency corrections to these figures are discussed in section 5.4 and a fit made to their distribution in section 6.5.

4.6 The η.

No special study of the η particle (which decays to two photons with a branching ratio of 39% [53]) is made in this thesis, but for completeness the relevant region of the reconstructed mass spectrum is shown in fig. 4.12. The η mass peak is clearly visible but the signal is only a factor of two greater than the background. A detailed study of the η, including a determination of its cross section, has been made by other members of the WA70 collaboration [54].

4.7 Isolating the Direct Photon Signal.

Removing the background to the direct photon signal is more difficult than that for the π^0, as there is no mass peak and consequently fitting programs cannot be used.

It is particulary important, therefore, to isolate as clean a sample as possible before proceeding to the question of detection efficiency.

The data remaining after the cuts described above in sections 4.3-4.5 (including the 'strict' halo cuts) were resubjected to the routine of section 4.3, which cut on the pt of the trigger shower. Previously this cut was at 2 GeV/c, but since we are no longer interested in π^0 events and direct photons with comparatively low pt, this was increased to 4 GeV/c. This basic cut removed approximately 50% of the remaining events immediately, and the numbers of candidate direct photon events remaining in each bin after it are shown in table 4.2

Next, the possibility of trigger showers being one half of a $\pi^0 \rightarrow \gamma\gamma$ decay in which the other photon has missed the calorimeter was tackled by imposing a fiducial cut on the shower position.

Assuming that the trigger photon had come from a π^0 decay of asymmetry 0.5 (i.e. $E_1 = 3 \times E_2$), the distance between the two photons striking the calorimeter, D, was calculated. The trigger shower was then required to to be (D+2) cm from the quadrant edges. The separation distance of the decay photons from the π^0s detected during the '84 and '85 data-taking runs is shown in fig. 4.13 (solid line), together with the Monte Carlo prediction (dashed line). This cut removed 7% of the remaining events.

The next cut was based on the width of the trigger shower in the first (front) calorimeter segment. While the shower for most of the remaining events had a width of < 3 cm in segment one, photons with pt > 4 GeV/c arising from

asymmetric π^0 decays and muons, identified by the cuts described above, have width distributions with tails extending beyond 3 cm.

A cut on shower width greater than 3 cm was therefore imposed. It eliminated approximately 1% of "good" π^0 showers, 3% of good direct photons but over 10% of the remaining muon halo events.

If the two photons from a $\pi^0 \rightarrow \gamma\gamma$ decay struck the calorimeter closer than 3 cm apart, they could not be resolved and appeared as one unusually wide shower. These showers, which otherwise have all the characteristics of direct photon showers, were also eliminated by this cut.

Next, a further check for π^0 and η decay photons was made. Though the asymmetry limit specified above to identify a π^0 was 0.90, if a trigger shower could be combined with another photon shower in the quadrant to give a reconstructed mass in the range 70-200 MeV/c^2, it need only have an asymmetry < 0.95 for the trigger shower to be rejected. This was done to ensure as clean a sample of direct photons as possible. Only showers with an energy greater than 600 MeV were combined with the trigger shower, as a study of photon pairs with reconstructed masses between 70 and 200 MeV/c^2 in which the lower energy photon had an energy < 600 MeV showed no visible peak at 135 MeV/c^2.

The η peak was considerably smaller than the π^0 peak and had a much smaller signal/background ratio. Care therefore had be taken not to reject too much in this region as many genuine direct photons would have been lost with the η. Much of the background beneath the peak was caused by very asymmetric photon pairs accidentally having reconstructed masses in the region of the η mass by chance, and care must be taken not to reject too many good direct photon events while removing the background from η decays. To further this aim a lower energy limit was placed on the lower energy decay photon. No peaks in the reconstructed mass plot could be seen when this limit was placed at 2 GeV/c,

though when set any higher a small peak at the η mass could be discerned. A few asymmetric $\eta \rightarrow \gamma\gamma$ decays will be passed as direct photon events, but it must be recognised that there is no perfect solution to this problem and the 2 GeV/c limit is designed to optimise both direct photon detection efficiency and η rejection. The asymmetry limit for an η was set at 0.95 and the mass limits were 470 to 630 MeV/c^2.

Hadrons and leptons also produced showers in the calorimeter. The hadrons were dealt with at an earlier stage of the analysis (section 4.3), but showers produced by electrons and muons are still present. These particles, being charged, are detected in the MWPC which stands directly in front of the calorimeter, and if a MWPC space point was found within 3 cm of a trigger shower the event was rejected.

Charged particles also leave signals in the inner Omega detectors and in most cases will have associated TRIDENT tracks. These TRIDENT tracks were extrapolated to the front face of the calorimeter to check that they did not intersect it at or near a candidate direct photon shower.

As described in section 3.2, TRIDENT groups tracks into two classes; those which can be extrapolated back to the vertex ('vertex tracks') and those which cannot ('extra tracks'). The extra tracks had to pass certain 'quality requirements' before they could be used to veto photon showers.

Some matching tracks may be background caused by chance track alignment with a photon candidate. Rather than simply reject all those showers with a nearby track, matching the momentum of the track p with the energy of the shower E allowed a further check. The ratio p/E should be close to 1.0 for a genuine match. If a TRIDENT track intersected the calorimeter less than 6cm from a direct photon shower and had a p/E ratio of over 0.5 the event was rejected.

One final cut was made to reduce the muon halo contamination, and this was a

cut based on the balance of transverse momentum in an event. First, an axis is defined in the direction of the transverse momentum of the trigger shower, Pt. If the experiment could detect all charged and neutral particles perfectly, the summed transverse momentum pt_{other} of the other particles in an event should be equal to -Pt, and the vector sum $pt_{total} = Pt + pt_{other}$ should be equal to 0. In a muon halo event, which is essentially a normal ($pt_{total} = 0$) event with a superimposed muon shower ($pt = pt_m$, say), pt_{total} will be approximately equal to pt_m. We define the quantity $F = pt_{total} / Pt$, and note that in 75% of the events already classed as halo by the preceding cuts, F was greater than 0.8. For an event to be accepted as containing a direct photon, F was required to be less than 0.8.

The number of events on a typical tape passing each cut is shown as table 4.3. The pt and xf distributions of the direct photon events remaining at this point in the analysis are shown in figs. 4.14a and 14b respectively.

Having isolated as clean a direct photon sample as possible, with negligible muon contamination, and having clearly defined the cuts used to produce it, we must consider any remaining backgrounds to the direct photon signal, the number of genuine direct photons removed by the above cuts, and the acceptance of the detector for direct photons. These topics are all dealt with in the next chapter.

Chapter Four Figures and Tables.

Figure 4.11 Reconstructed $\gamma\gamma$ mass for one pt/xf bin, specifically $4.5 < pt < 4.75$ GeV/c, $-0.05 < xf < +0.05$.

Figure 4.12 Reconstructed $\gamma\gamma$ mass spectrum in the region of the η, whole data sample.

Figure 4.13 Separation of π^0 decay photons at the calorimeter as measured in the '84/'85 data (solid line), and as predicted by the Lund Monte Carlo (dashed line).

Figure 4.14a Pt distribution of direct photons remaining after cuts described in chapter 4.

Figure 4.14b Xf distribution of direct photons remaining after cuts described in chapter 4.

Table 4.1 Raw numbers of π^0s.

Table 4.2 Numbers of direct photons remaining after second pt cut.

Table 4.3 Event numbers passing each cut.

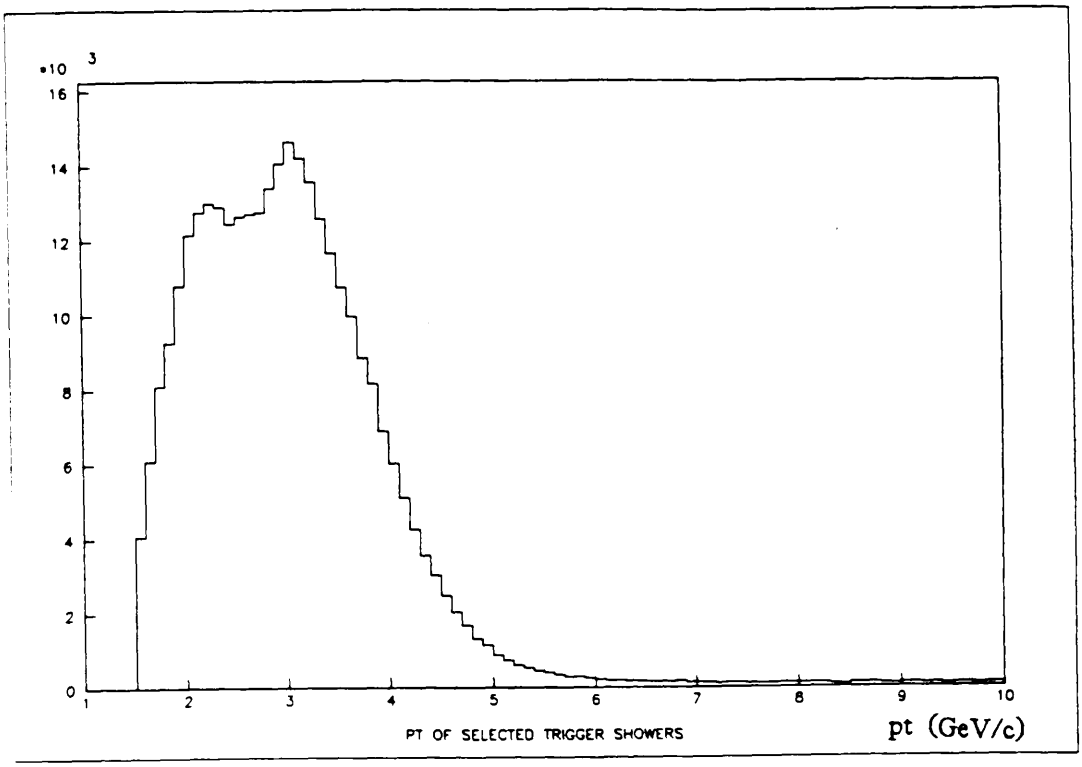

Figure 4.1

Calorimeter geometrical acceptance for photons

(The asterisks denote forbidden kinematical regions)

Pt (GeV/c)	3.13	3.38	3.63	3.88	4.13	4.38	4.63	4.88	5.13	5.38	5.63	5.88	6.13	6.38	6.63	6.88	7.13	7.38	7.63	7.88
Xf −0.95	0.00	0.00	0.00	0.00	0.00	0.00	0.00	0.00	****	****	****	****	****	****	****	****	****	****	****	****
Xf −0.85	0.00	0.00	0.00	0.00	0.00	0.00	0.00	0.00	0.00	0.00	0.00	0.00	0.00	0.00	0.00	0.01	0.02	****	****	****	****
Xf −0.75	0.00	0.00	0.00	0.00	0.00	0.00	0.00	0.00	0.00	0.00	0.00	0.00	0.01	0.02	0.05	0.10	0.15	0.21	0.28	0.38	0.48
Xf −0.65	0.00	0.00	0.00	0.00	0.00	0.00	0.00	0.00	0.01	0.03	0.07	0.13	0.17	0.24	0.30	0.39	0.48	0.56	0.64	0.68
Xf −0.55	0.00	0.00	0.00	0.00	0.00	0.02	0.06	0.10	0.17	0.24	0.31	0.40	0.53	0.60	0.66	0.72	0.76	0.80	0.84	0.88
Xf −0.45	0.00	0.00	0.03	0.07	0.15	0.25	0.35	0.46	0.57	0.65	0.72	0.77	0.83	0.86	0.89	0.93	0.95	0.97	0.98	0.99
Xf −0.35	0.12	0.22	0.38	0.51	0.62	0.72	0.79	0.84	0.88	0.92	0.95	0.97	0.98	0.99	0.99	0.98	0.98	0.99	0.98	0.98
Xf −0.25	0.69	0.82	0.87	0.91	0.95	0.97	0.98	0.99	0.98	0.98	0.98	0.99	0.98	0.98	0.98	0.98	0.98	0.98	0.98	0.98
Xf −0.15	0.98	0.98	0.99	0.98	0.98	0.98	0.98	0.98	0.98	0.98	0.98	0.98	0.98	0.98	0.98	0.98	0.97	0.98	0.98	0.98
Xf −0.05	0.98	0.98	0.98	0.98	0.98	0.97	0.97	0.98	0.97	0.97	0.97	0.98	0.97	0.98	0.97	0.98	0.98	0.97	0.97	0.98
Xf 0.05	0.96	0.96	0.96	0.97	0.97	0.97	0.97	0.97	0.96	0.97	0.97	0.97	0.97	0.96	0.97	0.97	0.97	0.97	0.97	0.97
Xf 0.15	0.95	0.95	0.95	0.96	0.96	0.96	0.96	0.96	0.96	0.96	0.96	0.96	0.96	0.97	0.96	0.96	0.96	0.96	0.97	0.96
Xf 0.25	0.92	0.93	0.93	0.95	0.94	0.94	0.94	0.95	0.94	0.95	0.95	0.95	0.96	0.95	0.96	0.95	0.96	0.96	0.96	0.95
Xf 0.35	0.86	0.88	0.90	0.92	0.91	0.92	0.93	0.93	0.93	0.94	0.93	0.94	0.95	0.95	0.95	0.95	0.95	0.95	0.95	0.95
Xf 0.45	0.47	0.65	0.76	0.84	0.87	0.88	0.91	0.91	0.91	0.92	0.92	0.92	0.93	0.93	0.93	0.94	0.94	0.94	0.94	0.95
Xf 0.55	0.09	0.19	0.34	0.52	0.65	0.75	0.82	0.85	0.88	0.91	0.91	0.91	0.92	0.93	0.93	0.93	0.92	0.93	0.92	0.93
Xf 0.65	0.00	0.01	0.06	0.13	0.25	0.38	0.54	0.66	0.78	0.81	0.85	0.88	0.89	0.90	0.90	0.91	0.91	0.91	0.91	0.92
Xf 0.75	0.00	0.00	0.00	0.01	0.04	0.12	0.19	0.29	0.43	0.56	0.65	0.73	0.79	0.82	0.86	0.88	0.89	0.91	0.91	0.92
Xf 0.85	0.00	0.00	0.00	0.00	0.00	0.00	0.01	0.03	0.09	0.15	0.26	0.39	0.53	0.65	0.75	0.79	0.84	****	****	****	****
Xf 0.95	0.00	0.00	0.00	0.00	0.00	0.00	0.00	0.03	****	****	****	****	****	****	****	****	****	****	****	****	****

Figure 4.2

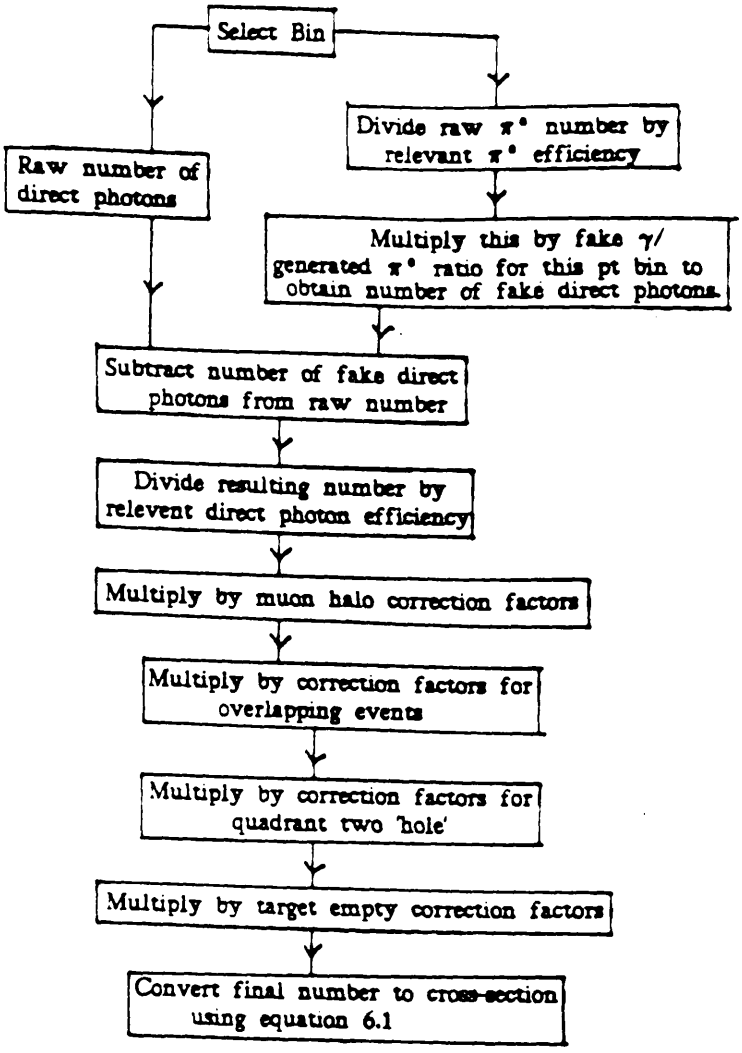

Figure 4.3

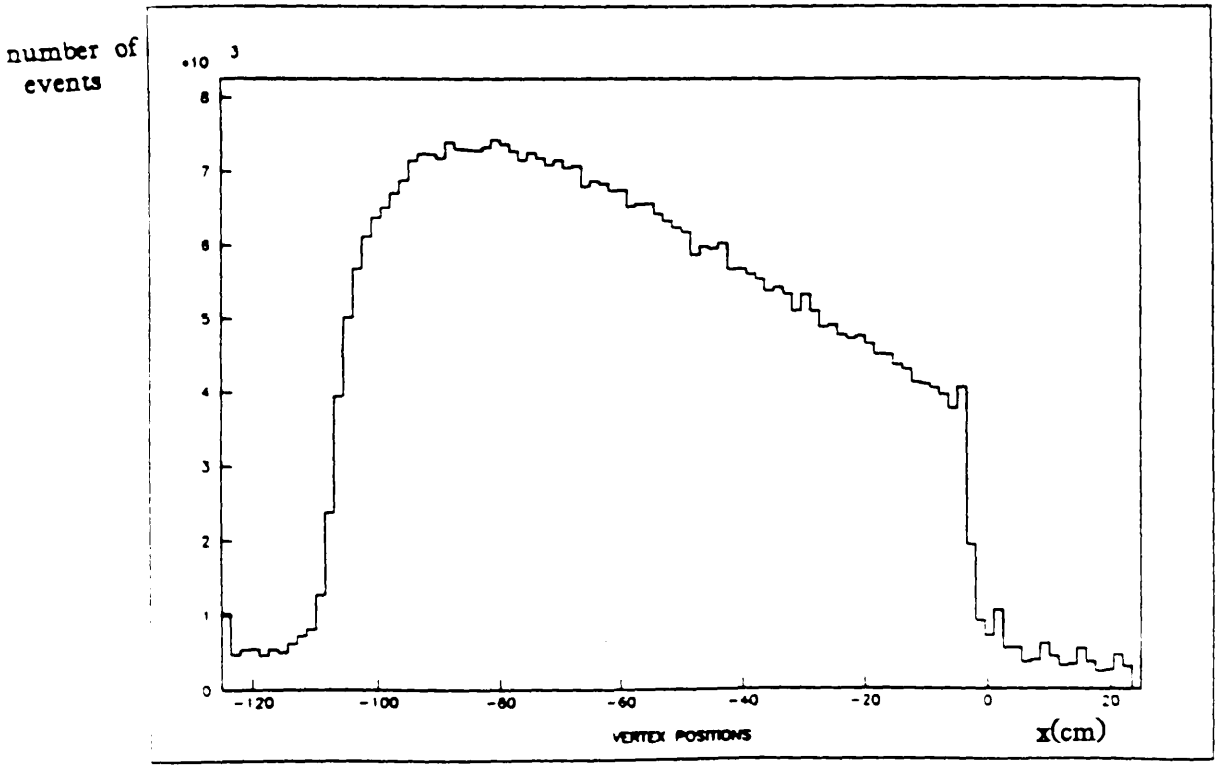

Figure 4.4

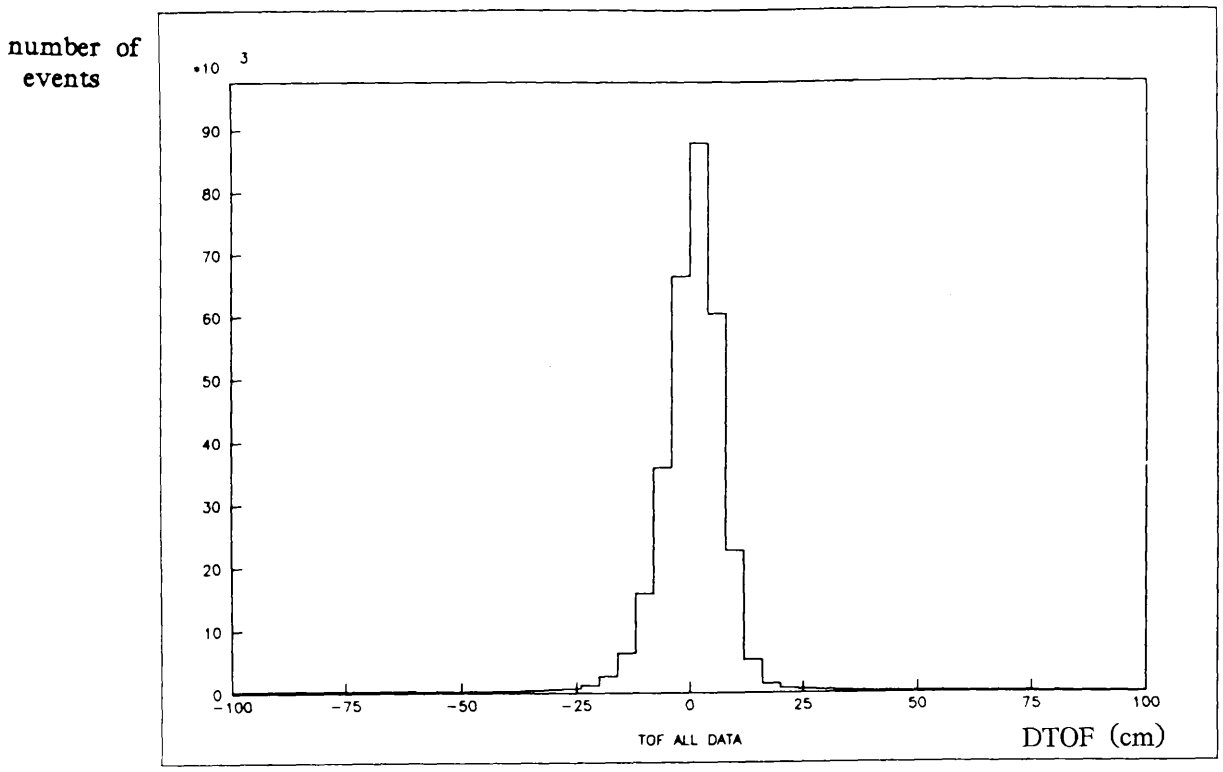

Figure 4.5a

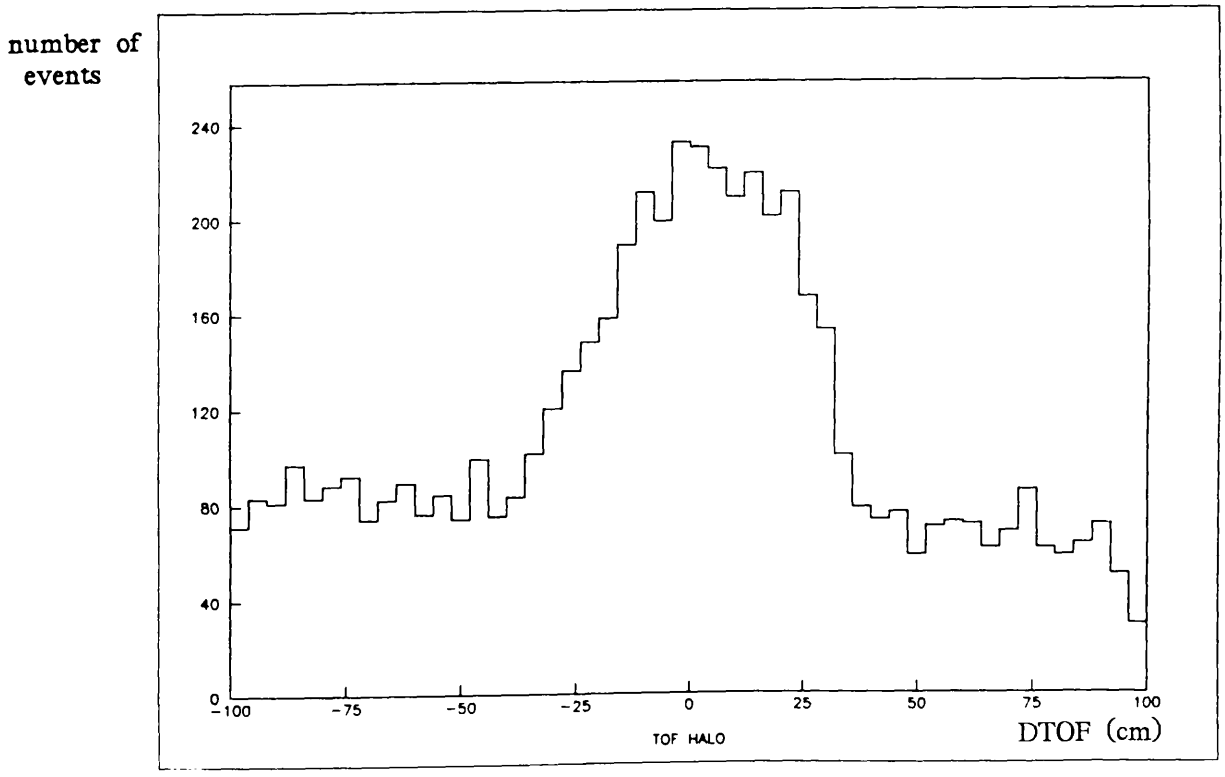

Figure 4.5b

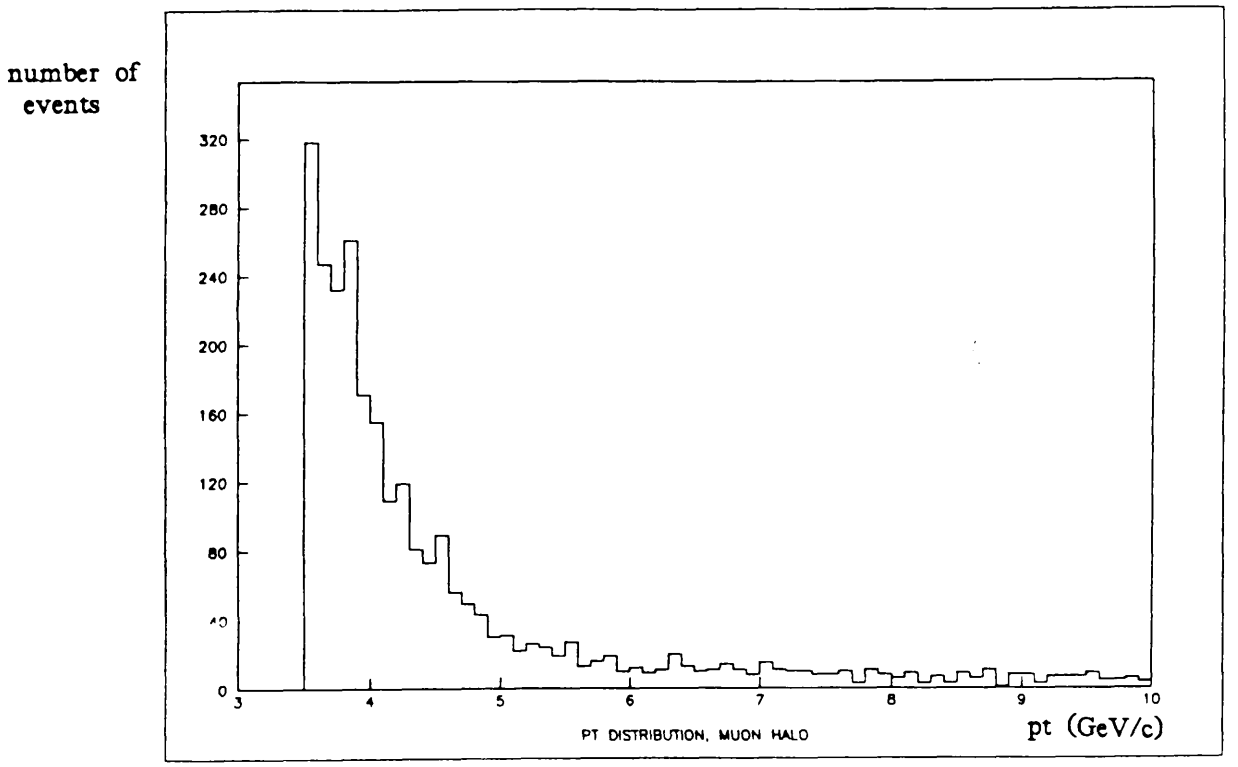

Figure 4.6a

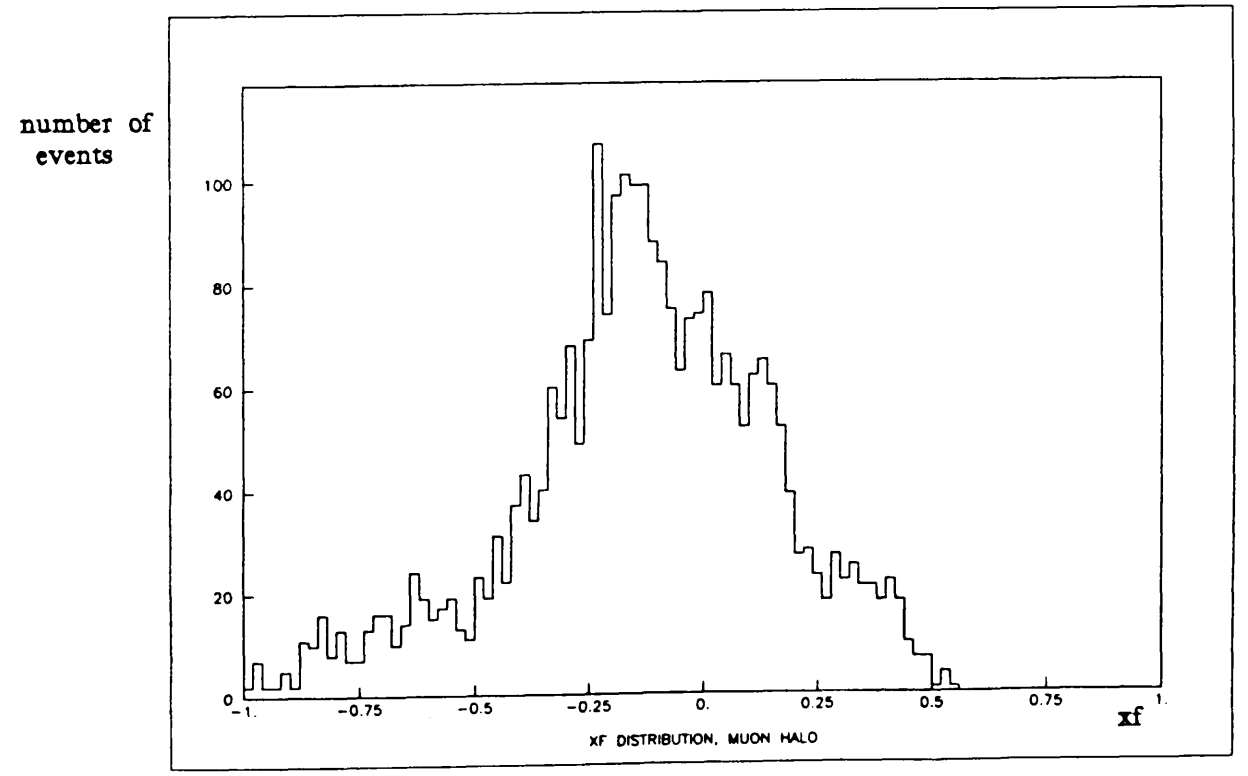

Figure 4.6b

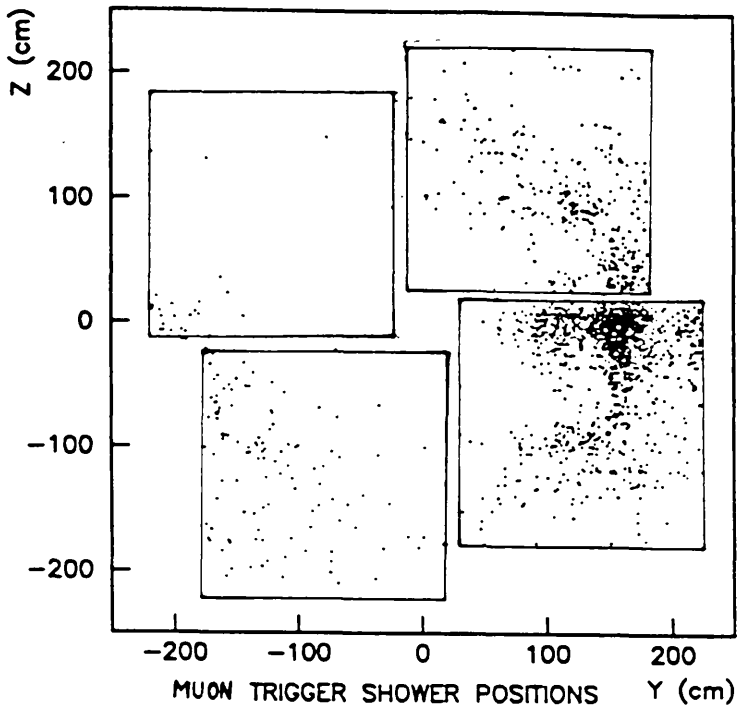

Figure 4.7

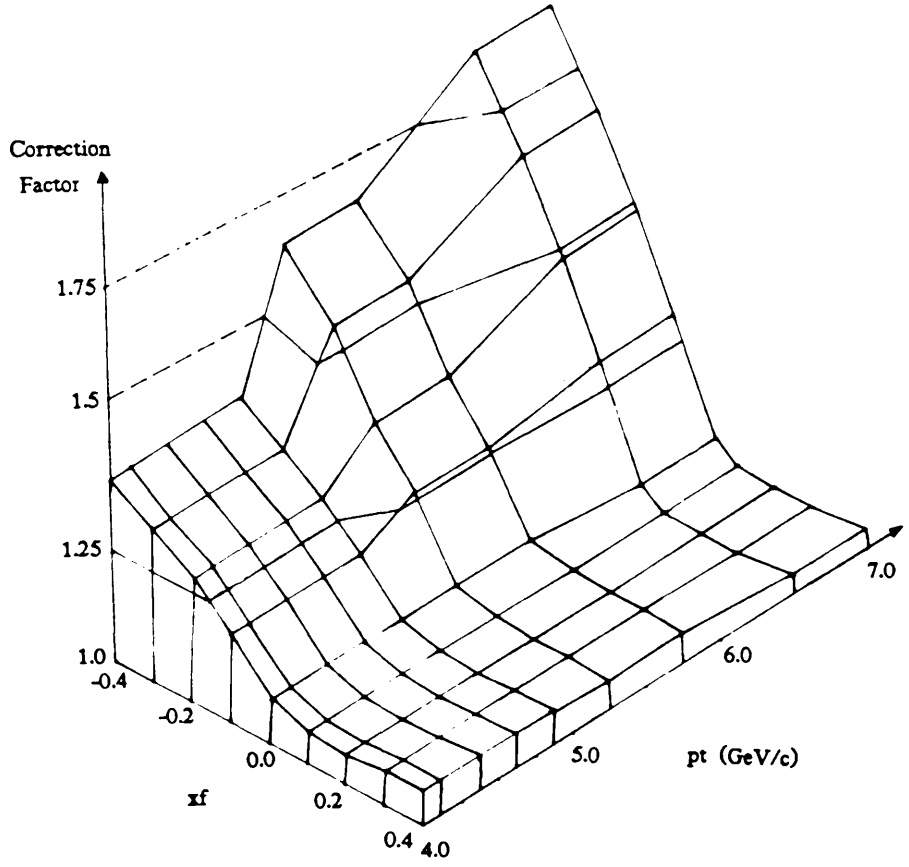

Figure 4.8

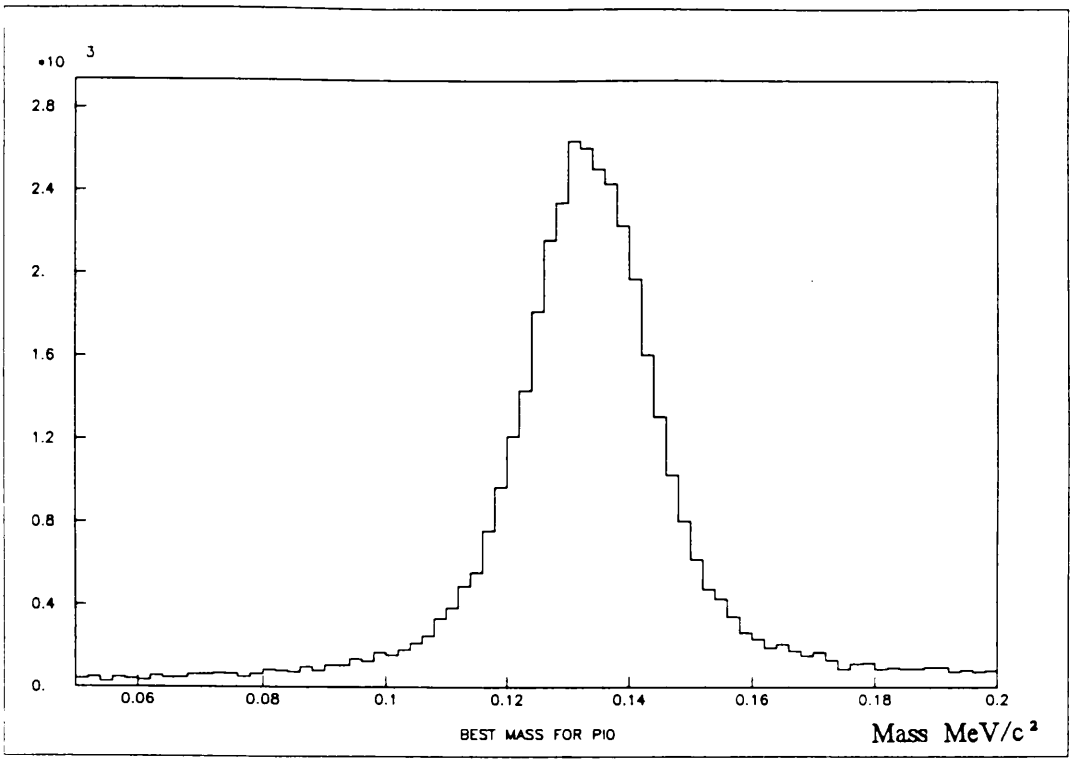

Figure 4.9

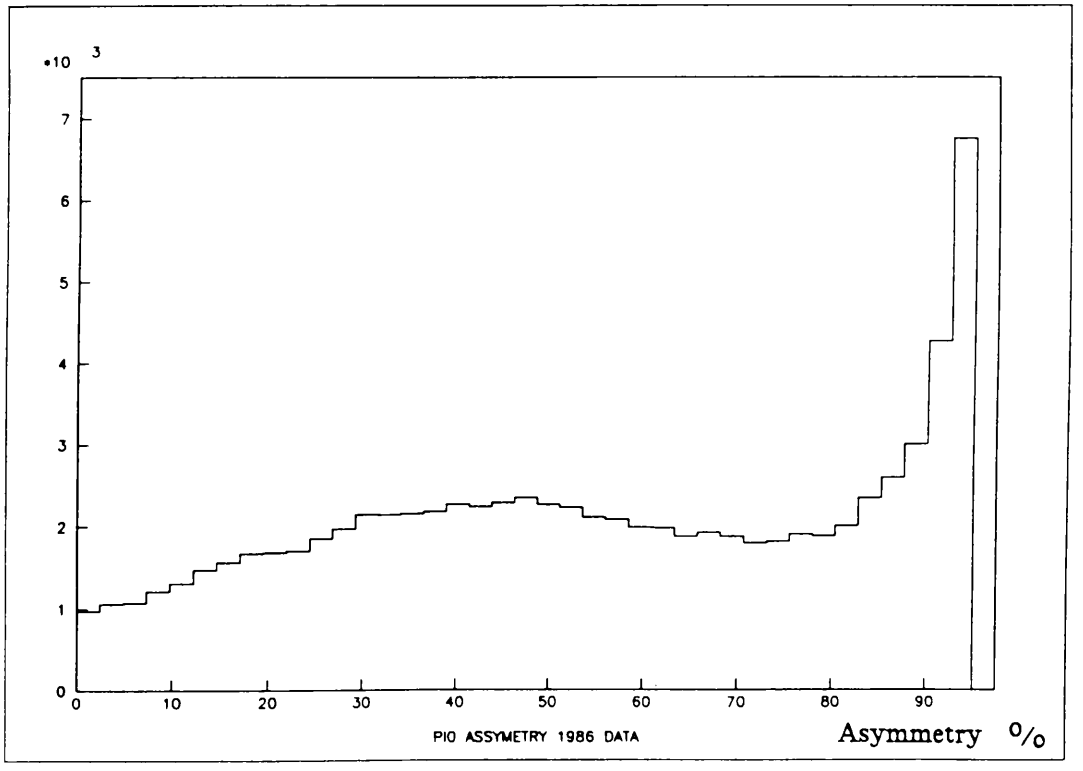

Figure 4.10

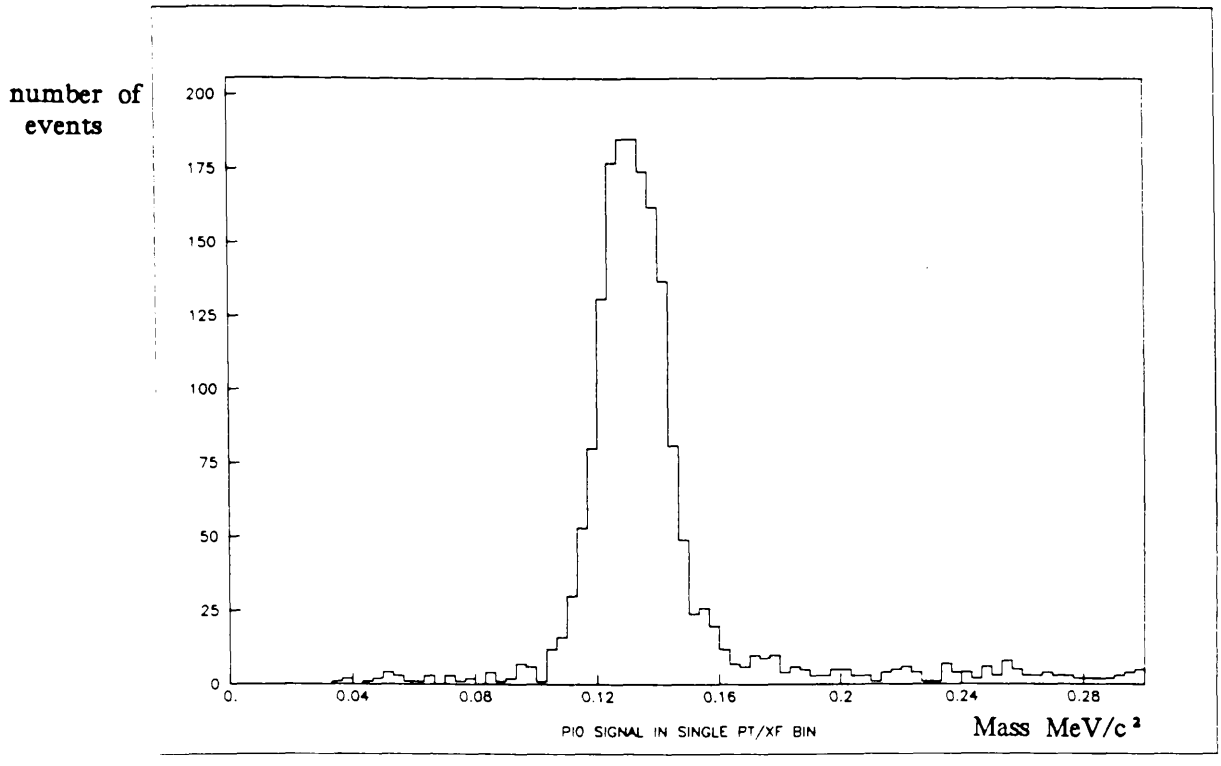

Figure 4.11

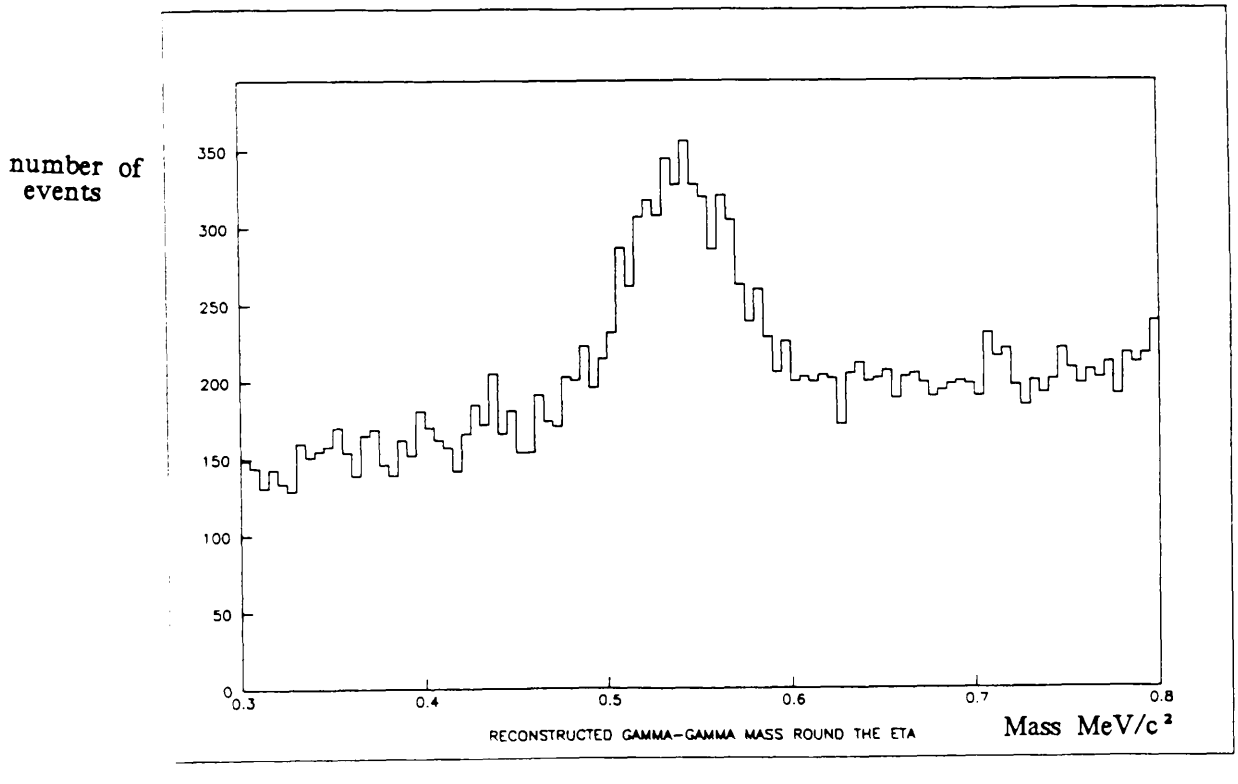

Figure 4.12

Table 4.1 - Raw Numbers of π°s.

xf \ Pt (GeV/c)	4.	4.25	4.5	4.75	5.0	5.5	6.0	7.0
-0.45	93	92	50	52	68	54	21	
-0.35	765	566	334	208	188	50	22	
-0.25	2847	1653	922	435	407	113	39	
-0.15	3628	2217	1165	678	553	131	43	
-0.05	3207	2243	1303	748	527	129	58	
+0.05	2752	2036	1215	691	529	165	56	
+0.15	1679	1495	937	509	476	100	43	
+0.25	884	698	441	240	212	57	16	
+0.35	735	472	287	158	136	31	14	
+0.45								

Table 4.2 - Raw Numbers of Direct Photons.

xf	Pt (GeV/c) 4. – 4.25	4.25 – 4.5	4.5 – 4.75	4.75 – 5.0	5.0 – 5.5	5.5 – 6.0	6.0 – 7.0
-0.45 – -0.35	174	157	94	67	69	17	16
-0.35 – -0.25	179	143	111	96	93	27	19
-0.25 – -0.15	334	335	235	148	154	66	38
-0.15 – -0.05	581	456	310	210	188	56	44
-0.05 – +0.05	656	538	375	218	198	78	43
+0.05 – +0.15	894	623	365	201	170	78	28
+0.15 – +0.25	698	489	306	178	170	73	8
+0.25 – +0.35	226	184	128	81	82	38	8
+0.35 – +0.45	27	33	20	18	20	15	10

Table 4.3 - Events passing each cut for one tape.

Tape 980974 stored at Rutherford Appleton Lab. This tape holds 5 runs, 3320-3324. It is typical of the 37 data tapes taken in 1986

Total events on tape;	15039.
Unreadable events on tape:	1.
Events into cutting routines;	15038.
After shower multiplicity cut;	15038.
After vertex cuts;	12618.
After first pt cut (1.5 GeV/c);	12499.
Highest pt is charged particle;	1703.
After fiducial cut;	10055.
After 'gentle' halo cuts;	9371.

Direct Photon cutting routines.

After second pt cut (3.5 GeV/c);	2266,
After second fiducial cut;	2165.
After segment one width cut;	2160.
After 'strict' halo cuts;	2031,
After second π^0 search:	1027.
After second eta search;	815.
After TRIDENT track matching cuts;	655.
After BMWPC hit matching cuts;	612.
Remaining candidate direct photon events:	612.

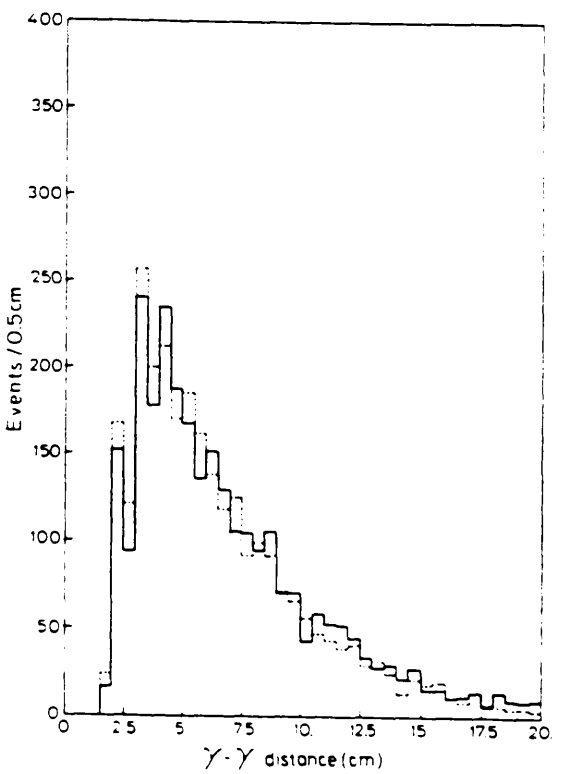

Figure 4.13

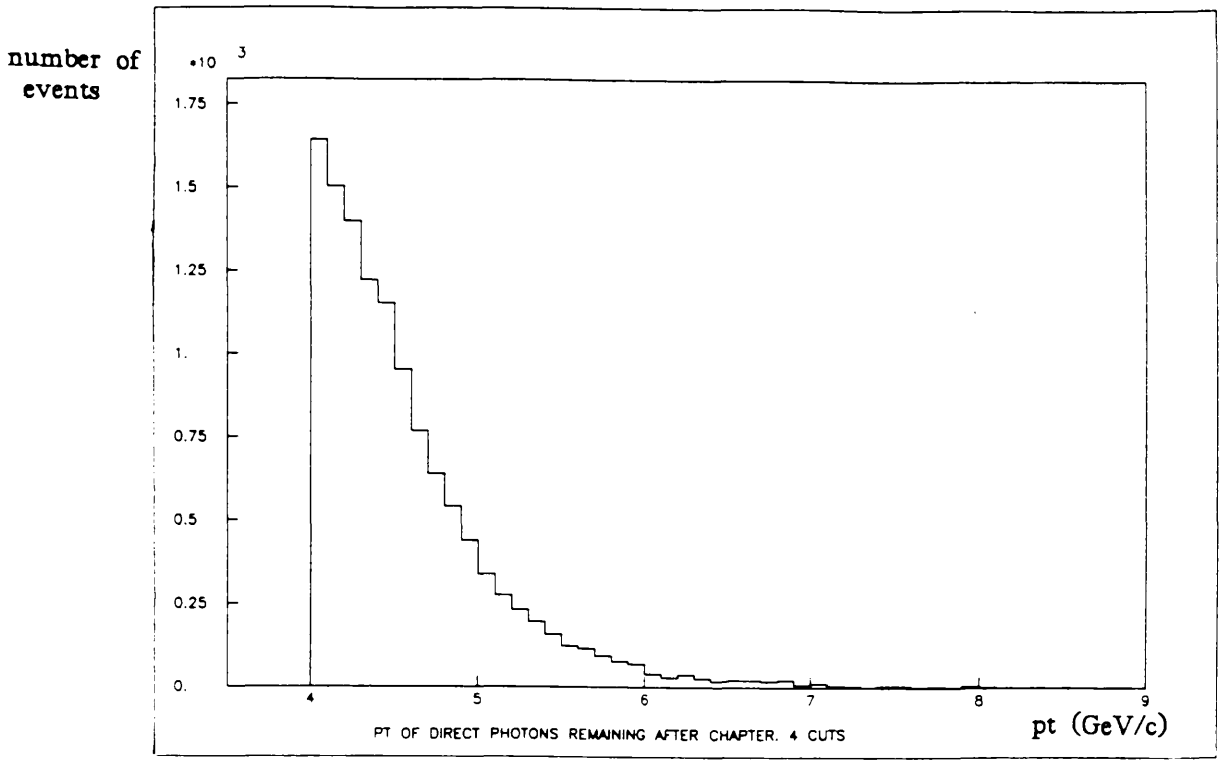

Figure 4.14a

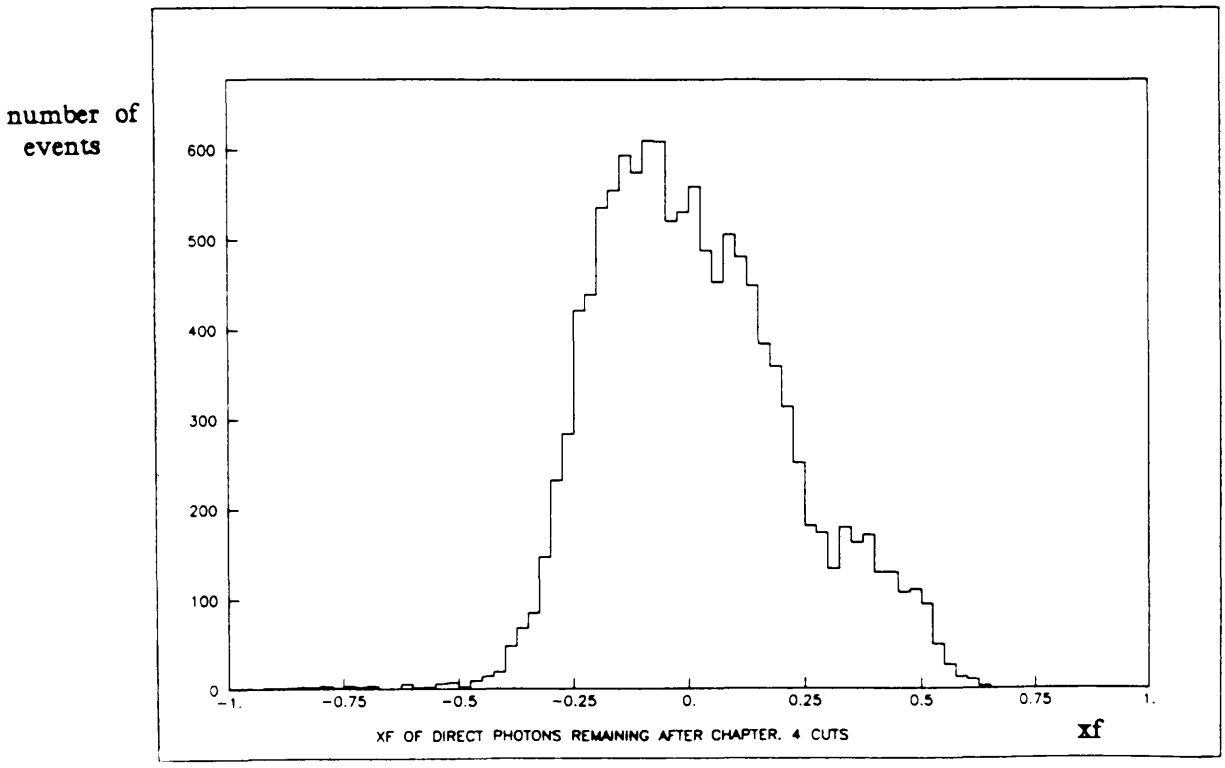

Figure 4.14b

CHAPTER 5

Backgrounds and Efficiencies.

5.1 Using the Lund Simulated Data.

The calculation of backgrounds and efficiencies mainly used data simulated by the Lund Monte Carlo program. An explicit calculation of the losses due to the inefficiencies of each element of the detector would have been extremely difficult if not impractical, and would have incurred a large systematic error. Similarly, calculating the efficiency of the various stages of the off-line analysis individually (while practical) would have been less accurate than running the complete set of analysis programs on well understood simulated data.

The subprocess responsible for a particular event, and by extension the particles leaving the interaction region, are known for Monte Carlo events. By passing such data through the entire analysis chain, and by comparing the numbers of π^0s and direct photons found with the numbers input we can measure the combined acceptance and efficiency for any type of particle for any specified kinematic region. In practice the regions chosen are congruent with the xf/pt bins used in the analysis of the real data. In some bins at high pt and high xf the statistics are low and the numbers in two or more adjacent bins have been combined.

This calculation is not, however, perfect. The Monte Carlo programs took no account of the muon halo, and the losses associated with it had to be dealt with separately. Overlapped events - in which two distinct events have occurred at approximately the same time - are also not represented in the Monte Carlo data. Both problems are discussed below.

The question of systematic errors is also dealt with in this chapter.

5.2 The Background to the Direct Photon Signal.

The largest source of fake direct photons were π^0 or η decays in which the meson was not reconstructed, leading to one of the two decay photons being wrongly identified as a direct photon. To investigate this, the events generated by the Lund program using only the first seven subprocesses listed in section 3.3.3 were used. We shall refer to this data as set A, and the other data (the direct photon producing subprocesses 8 and 9) as set B.

As the two sets of subprocesses were not run in conjunction, the problem of normalising the fake direct photons (as seen in set A) to the real direct photon signal (simulated only in set B) arose. It was solved in the following way:

1) The set A events were analysed for π^0s and direct photons in exactly the same way as the real data, including the muon halo cuts.

2) The number of direct photons found by the analysis was divided by the number of π^0s found for each pt/xf bin. This ratio was typically 0.1 or less.

3) The number of π^0s found in the real data was multiplied by the ratio described in (2). This gave the number of fake gammas in the real data.

Historically, the ratio used in the collaboration to quantify the direct photon background was fake gammas/generated π^0s, rather than fake gammas/observed π^0s. This figure is readily obtainable from the MC data. The ratio varies little with pt but considerably with xf. The ratio fake gammas/generated π^0s versus xf is shown in fig. 5.1a. The size of the error bars is dependent on the number of Monte Carlo events available. Although there were 219,000 such events at Glasgow, approximately twice this number were available at the University of

Geneva, and the same ratio as measured by them appears as fig. 5.1b [55]. The two are consistent, but the Geneva figures have smaller errors.

Before we can use the Geneva figures in the analysis, the compatibility of the two sets must be demonstrated. The direct photon analysis programs used at Geneva were different from those used at Glasgow, and this will make a small difference to the number of direct photons seen. However, as the direct photon cross-sections measured by the Glasgow group (using the Glasgow figures for gamma/generated π^0) were in good agreement with those measured by Geneva, this error should be negligible compared with the statistical errors. The number of generated π^0s on a particular tape is the same in both analyses. Increasing statistics by including the Geneva Monte Carlo data was therefore assumed to be a valid procedure which reduced the statistical error on the fake direct photon numbers substantially.

One disadvantage of using the ratio fake gammas/generated π^0s rather than fake gammas/observed π^0s is that the former must be convoluted with the pion efficiencies (see below) before the proportion of fake direct photons in the observed direct photon signal can be calculated. However in the lower pt region where the background is most important a large sample of low pt Monte Carlo π^0 events allows us to measure the π^0 efficiencies accurately. The error introduced by this (typically 10% in the fake gamma/observed π^0 ratio) is smaller than the error that would have been incurred if the Geneva group's Monte Carlo events had not been used (approximately 60% in the ratio). The final fake gamma/generated π^0 ratio is shown as fig. 5.1c, and the resultant numbers of corrected direct photons (before the application of the correction factors described below) are shown in table 5.1.

5.3 The Signal to Background Ratio for Direct Photons.

The direct photon signal/background ratio is approximately 1.0 at a pt of 4 GeV/c, but by 5.5 GeV/c it is close to 6.0 or 7.0. This is primarily because the π^0 cross-section falls more steeply with pt than that of the direct photon, but also because π^0 reconstruction becomes easier as the energies of the decay photons increase. (Both direct photons and π^0s are more easily detected towards high pt as they stand out above low pt showers). Fig. 5.2 shows the signal/background ratio versus pt. The method of background subtraction for π^0s is described above in section 4.5.

Having calculated the number of genuine direct photon and π^0 events observed we must now examine the detector efficiency for each.

5.4 Direct Photon and π^0 Efficiencies and Acceptances.

The acceptance refers to the proportion of generated particles which the detector is geometrically capable of observing. Major inaccessible areas were caused by the gaps between quadrants and by the beamhole. In '86 a small calorimeter (the 'plug') was installed in the beamhole gap but the data from it was not well understood at the time of this analysis. Some photons with particularly high negative xf will not be seen as they will miss the calorimeter.

Similar comments apply for π^0s, the acceptance for which is more sensitive to the dead inter-quadrant areas as only one of the two decay photons need strike the calorimeter here for the π^0 to be unobserved.

Even though a direct photon or π^0 was geometrically observable it was not always satisfactorily identified due to coalesced showers, trigger faults, etc.

In this analysis geometrical acceptance and detector efficiency have been considered together. Acceptance times efficiency will be referred to simply as

efficiency from now on for brevity.

Calculating efficiencies using the Lund data was, in principle, simple (with provisos for the muon halo and overlapping events). Since we know the absolute number and pt and xf distribution of the events we pass through the detector simulation, production process and analysis programs, and the same quantities for the particles observed, by comparing 'events in' by 'events out' we can calculate the efficiency.

The efficiencies are calculated for finite kinematic regions congruent with the data bins for convenience. The results for direct photons and π^0s are shown in numerical form in table 5.2 and 5.3, and graphically against xf and pt in figures 5.3a,b and 5.3c,d respectively.

An efficiency of more than 100% is recorded in two bins with pt = 4.5 → 5.0 GeV/c, xf = +0.05 → -0.15. This is due to the pions in one xf bin being reconstructed with too low an xf, thereby moving them one bin towards negative xf. The bins above these two towards positive xf have a slightly lower efficiency than expected. As long as this effect is real and manifested in the data these calculated MC efficiencies will negate the effect. This effect has been caused by surfeits of one and five events in the two bins and it seems clear that these bins merely have very high efficiencies. When corrections for muon halo, overlapping events etc. are taken into account, the effective efficiencies will drop 25-40%. The direct photon and π^0 efficiencies as measured by the collaboration during the '85 analysis are plotted in figures 5.4a and 5.4b.

5.5 Correcting for the Muon Halo.

The Muon halo is not simulated in the Monte Carlo, and its effects on the data must be considered explicitly. It can affect the final direct photon and π^0 numbers in two ways. Firstly, the presence of a muon shower in a genuine event

may cause it to be rejected by the cuts not associated with the muon halo. Secondly, the cuts designed to reject muons may reject genuine direct photons and π^0s, principally because of TOF cuts. This latter problem is solved by including the halo cutting routines in the analysis of the Monte Carlo Data. Calculating the correction factors for the first case, however, is more complicated.

Two methods were used. One involved analysing the data with and without the cutting routines. The other involved a tape of data which had been specially processed without TOF cuts.

A study of the effect of the combined gentle muon cuts and routines which used the muon hodoscope data (almost equivalent, as mentioned above in section 4.4.1, to the strict muon halo cuts in the Glasgow analysis programs) was carried out by the University of Geneva, also using the specially produced tape method [61]. They found the correction factors for direct photons and π^0s to vary between 1.65 and 1.4 over the pt/xf plane, the largest correction being necessary in the high negative xf/high pt area. (The correction factors are shown in fig. 4.8.)

5.6 Overlapping Events.

A feature of real data which cannot be simulated by the Monte Carlo is overlapping events. These arise when two interactions occur so close together in time that the showers they produce are recorded as being from the same event. This can confuse the MICE and TOF cutting routines and results in some good events being rejected. Merely examining the numbers of 'good' events seen with the MICE and TOF cuts switched off is not satisfactory as large numbers of muon halo showers will then be present in the data to confuse the signal. If, however, the study is restricted to low pt events where muon halo is not such a problem (and of course can be allowed for to a first approximation), this method is reliable

enough to allow the effect to be measured. A study at Geneva [56] found the appropriate correction to be 1.10 ∓ 0.01 for both direct photons and π^0s.

5.7 The Quadrant 2 'Hole'.

Another overall correction factor was that necessitated by an area of insensitivity in quadrant two of the calorimeter. This was discovered by plotting the ϕ distribution of the direct photons identified using the cuts above (fig. 5.5 shows the ϕ distribution for the pt bin 4.5 → 4.75 GeV/c). One expects a uniform ϕ distribution, and no previous experiment has found otherwise. However, as can be seen, there is a significant shortfall of direct photon showers in quadrant two. (The dips are caused by the dead areas between quadrants.)

The cause of this 'hole' has not been identified precisely (a direct examination of the relevant scintillator tubes was impossible because the calorimeter was sealed) but an observed slow leak of the scintillator fluid was a possible cause. Evidence for this explanation was that the shortfall in identified showers was particularly acute in one half of the ϕ range covered by quadrant two. This could be accounted for by postulating the failure of the uppermost horizontal (y-direction) channels. When scintillator liquid leaked from a quadrant, the uppermost tubes would empty first. The quadrant was periodically refilled with scintillator fluid but this action did not reverse the impaired performance of the detector.

A. Maxwell of Glasgow worked on this problem for the '84 analysis and concluded that a correction factor of 1.06 [46] was appropriate for both direct photons and π^0s. An examination of the '86 ϕ distribution however, indicated that the problem had worsened (as one would expect if the leak hypothesis was correct), and the required correction factor had risen to 1.126 ∓ 0.004.

These final, corrected numbers must then be converted into cross-sections, as described in section 6.1.

5.8 Target Empty Corrections.

Beam particles can interact with the steel casing of the target and produce events which pass all levels of cuts and be accepted as 'good' events. They will not be included in the cross-section calculation (see below) and since the Monte Carlo simulates only the target and not the retaining structure around it this problem cannot be studied using the MC event sample. The direct photon numbers must therefore be reduced by the correct amount. Investigation of this at Liverpool [57] using specially prepared data tapes found that only three events per thousand were due to such interactions, but even so a correction factor of 0.997 ∓ 0.001 was adopted.

Following the introduction of a magnet behind the calorimeter to sweep away beam particles, the problem of spurious A1 and A2 counter hits was eliminated for the '86 run and no correction factor for this was needed.

5.9 Sources of Systematic Error.

The two largest sources of systematic error are the calibration of the absolute energy scale and the reliability of the Monte Carlo simulation.

a) The Energy Scale.

The cross-sections for direct photons and π^0s fall very steeply with pt and are very sensitive to changes in the absolute energy scale. A shift of 1% in the latter will introduce a corresponding change in cross-section of 10%.

As described above in section 2.9, the absolute energy calibration is made using the masses obtained from reconstructed ηs and π^0s. We can check this by comparing the momentum of TRIDENT tracks with the energy of the showers

produced by the same particles at the calorimeter. Measurements made at the time of the 1986 data-taking run showed a discrepancy of only 0.6%, which was equivalent to a systematic (pt dependent) error of around 5% in the cross-sections.

As described in section 2.8, electron beams were used to investigate the energy resolution, electrons with momenta of 10, 20 amd 50 GeV/c being targeted on fixed points on the calorimeter. As well as measuring the energy resolution for isolated showers quoted in section 2.8, it was also determined that the response of the calorimeter was linear with energy.

Knowledge of the absolute energy calibration at certain fixed points on the calorimeter must be complemented with the assurance that PM gains will not vary significantly across it. This was the purpose of the two calibration systems desribed in chapter two. No attempt was made to obtain the absolute energy scale of the calorimeter from the calibration systems. This subject has been discussed in detail elsewhere [38].

b) Uncertainties in the Monte Carlo.

A larger source of error is due to the unreliability of the Monte Carlo. An indication of this problem is apparent in that the shower multiplicity in the Lund events is on average one less that that observed in the data. If the Lund program is unreliable, errors will be introduced into the important fake gammas/generated π^0 ratio and direct photon and π^0 efficiencies. In short, the Lund program is only as good as the physics it contains.

A check on this was provided by the development of an independent Monte Carlo by the Milan WA70 group. This involved superimposing generated direct photons and π^0s onto shower distributions taken from real data. It thus had an average shower multiplicity one greater than that of the real data, and so naively might be thought to counterbalance the shortcomings of the Lund program to a first approximation. The Milan Monte Carlo also had the advantage of being faster

than the Lund Monte Carlo. The background estimates and efficiency measurements derived from this Monte Carlo were in good agreement with the Lund predictions and an upper limit of 15% was placed on the systematic error in the figures produced by the Monte Carlos. This was an overestimate and a study by the Geneva group showed that an error of 5-6% is more likely. For the purposes of this thesis, it was assumed to be 5%. This topic is dealt with in the calibration paper [38].

Chapter Five Figures and Tables.

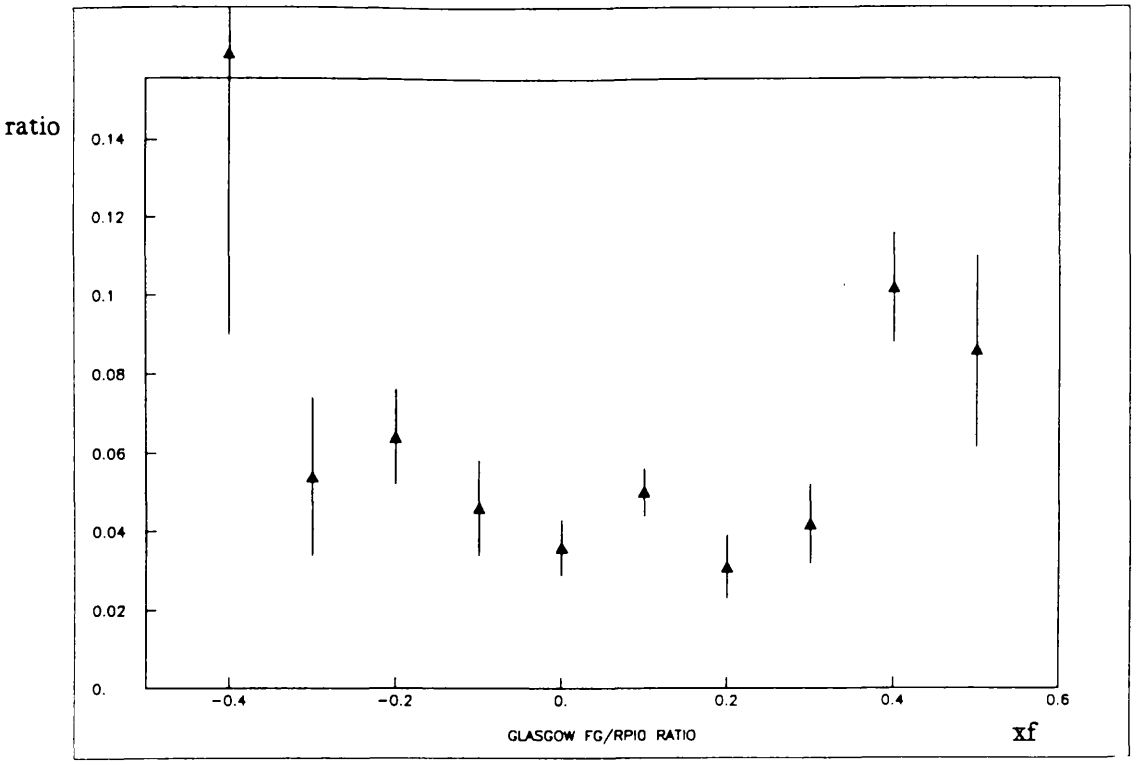

Figure 5.1a

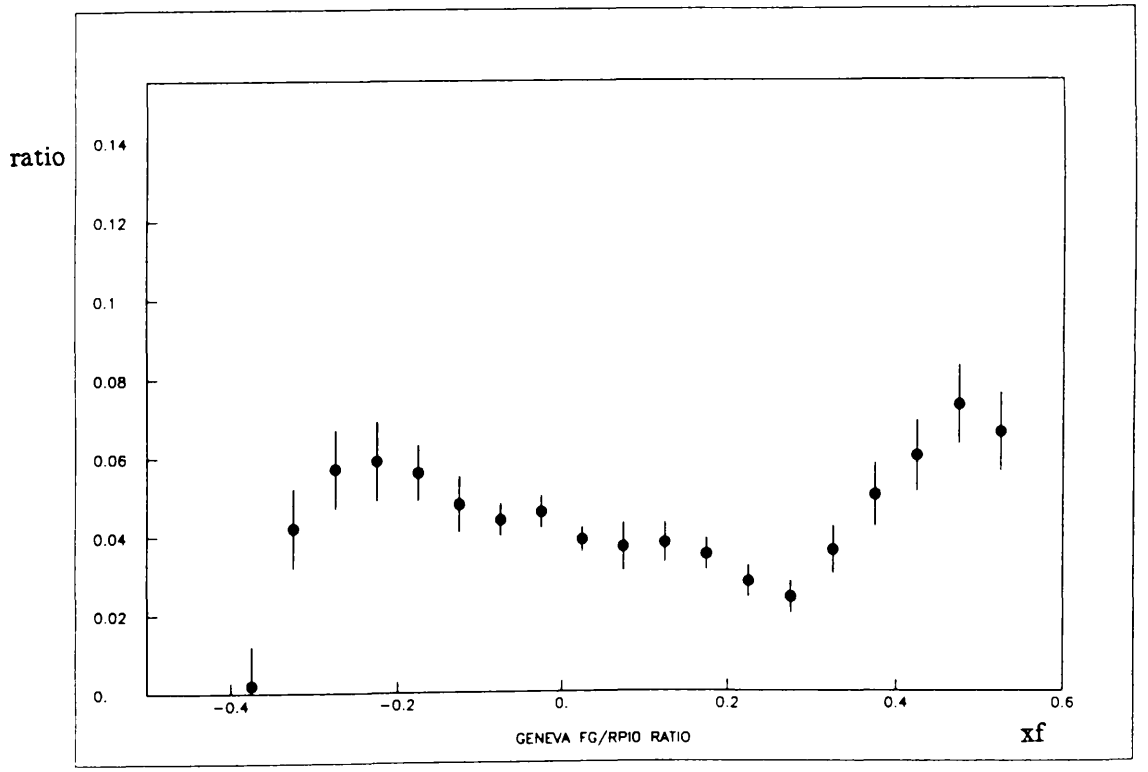

Figure 5.1b

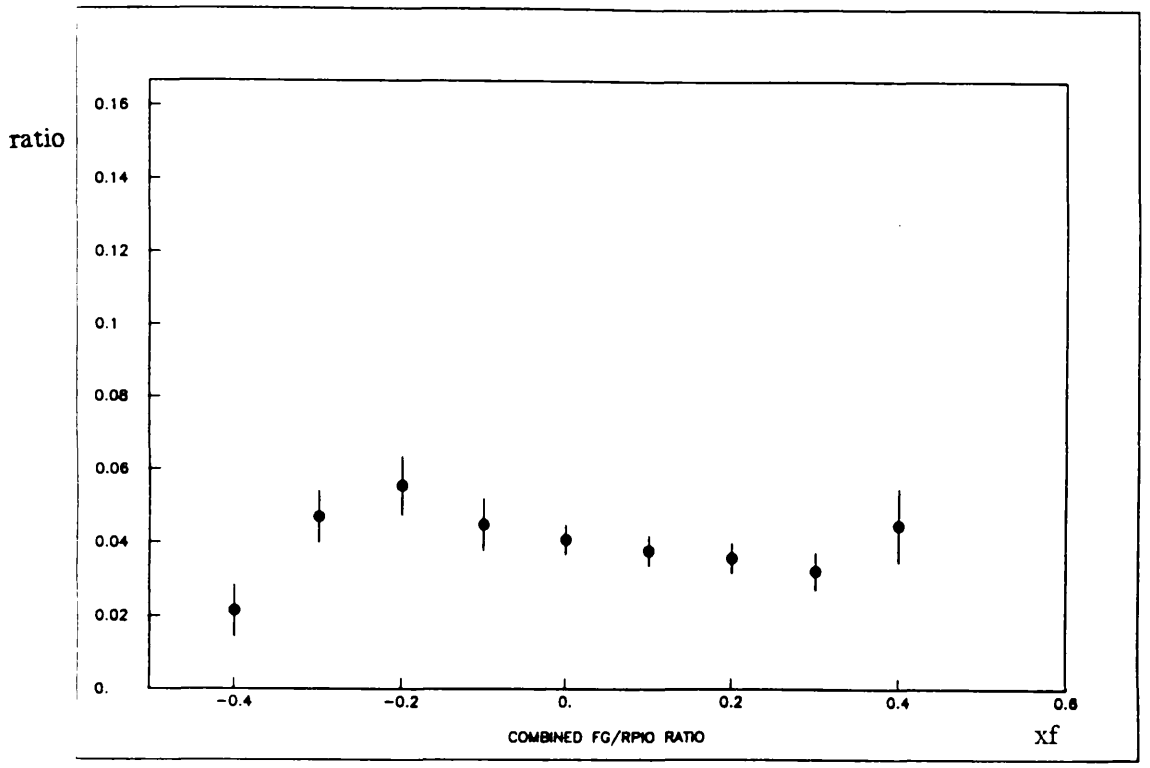

Figure 5.1c

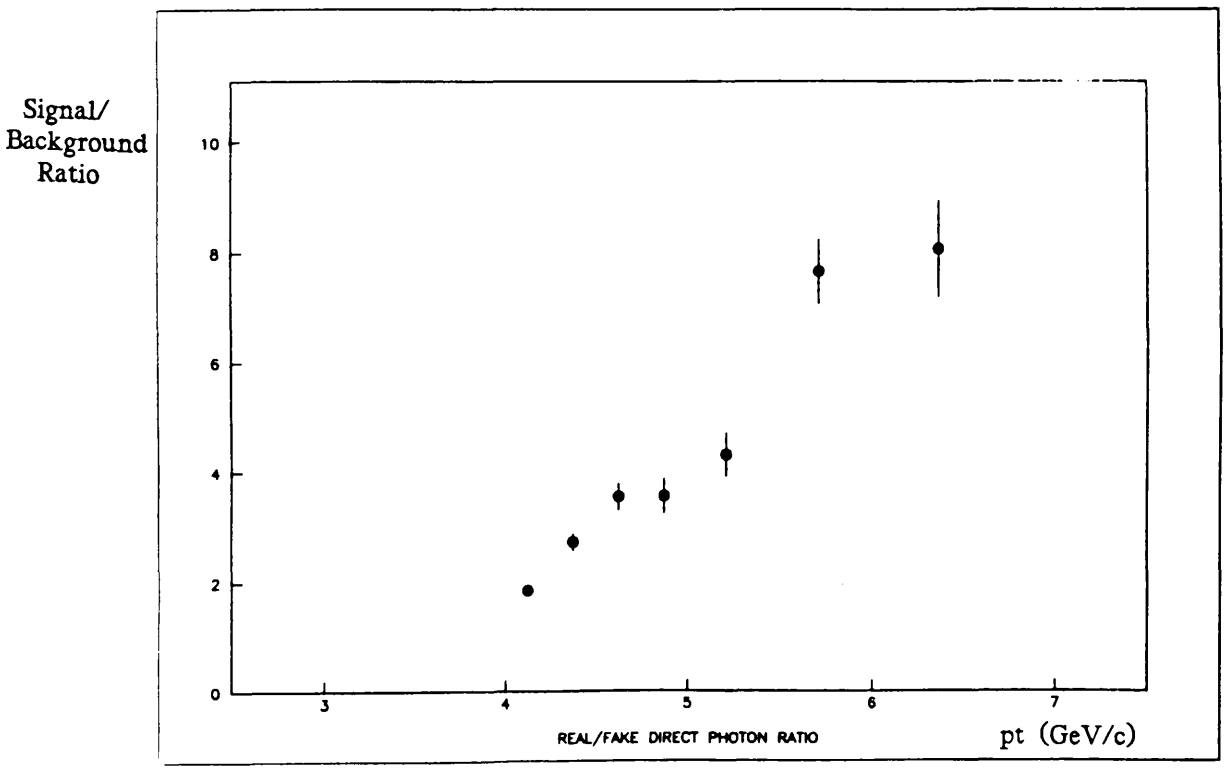

Figure 5.2

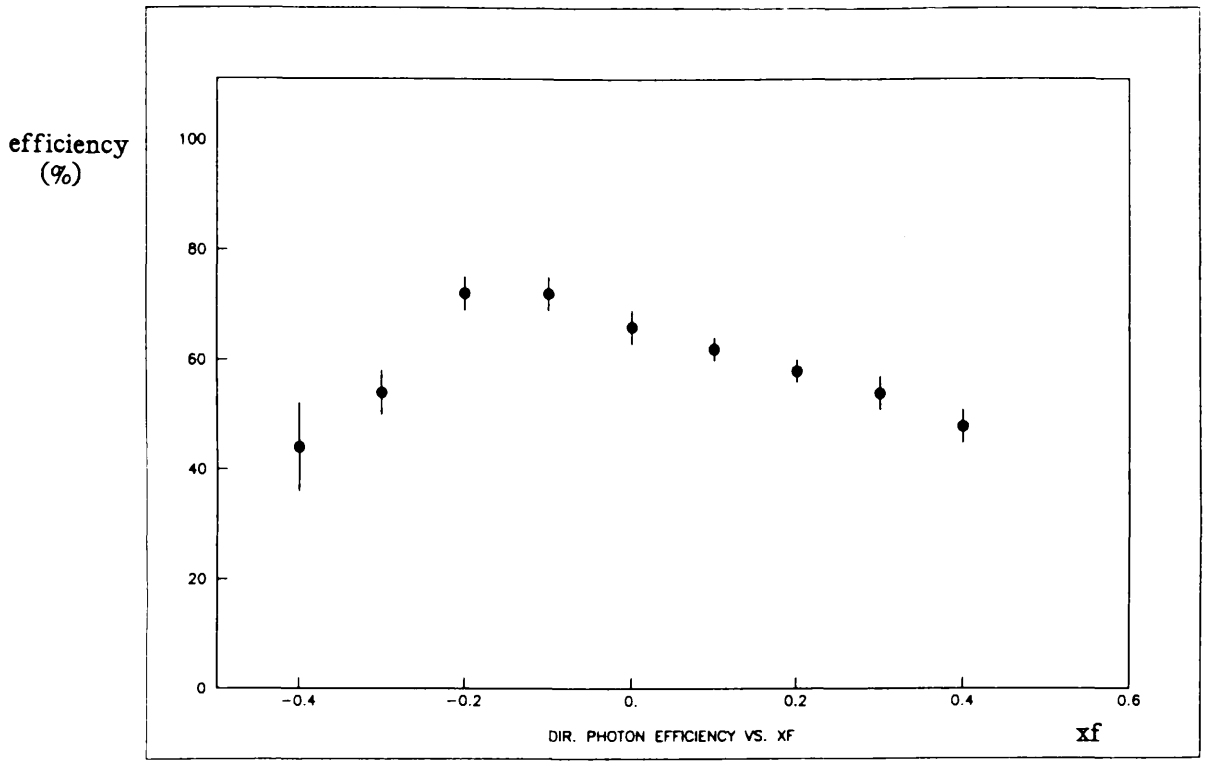

Figure 5.3a

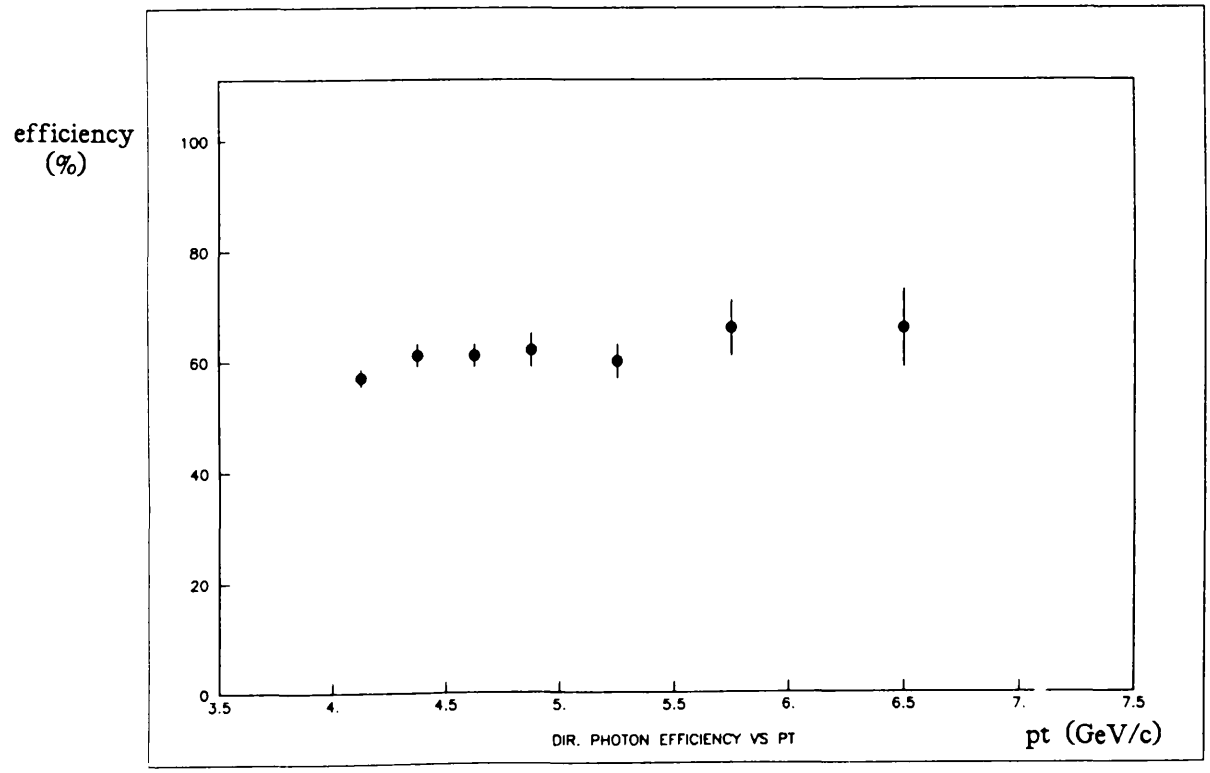

Figure 5.3b

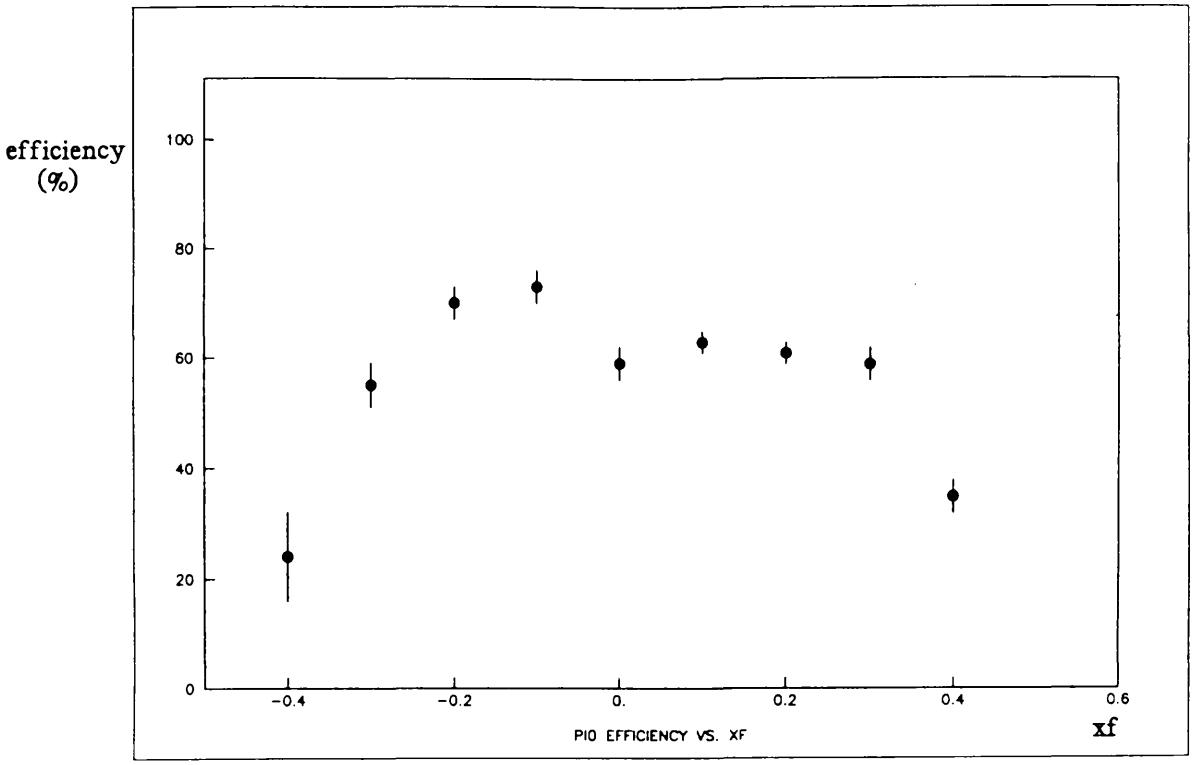

Figure 5.3c

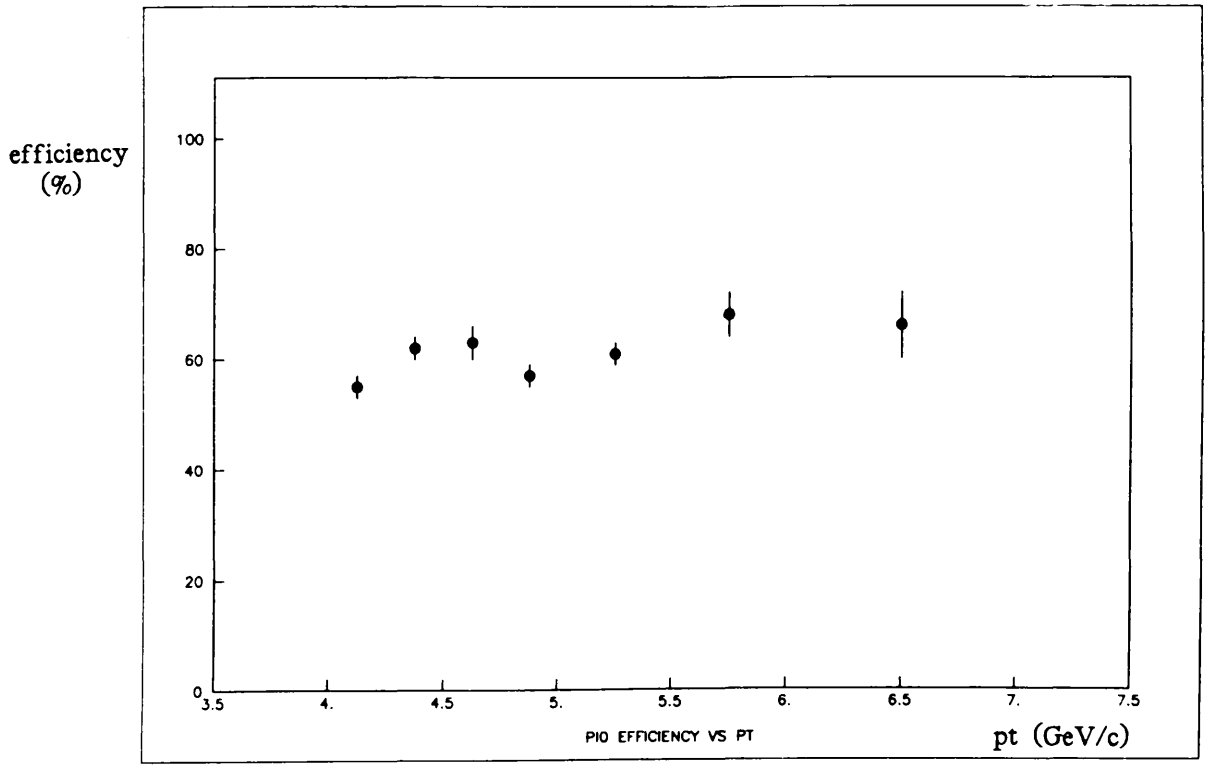

Figure 5.3d

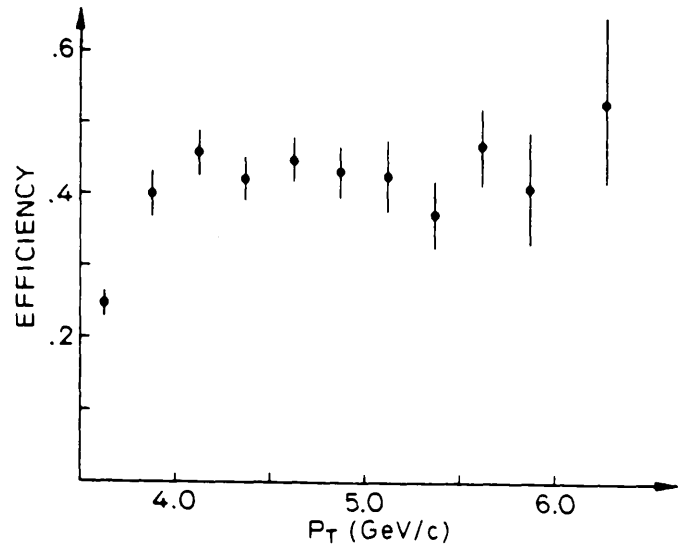

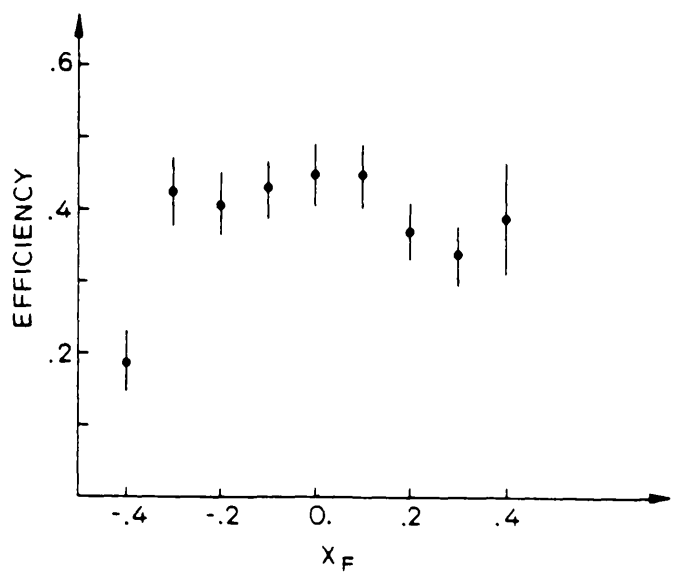

Figure 5.4a

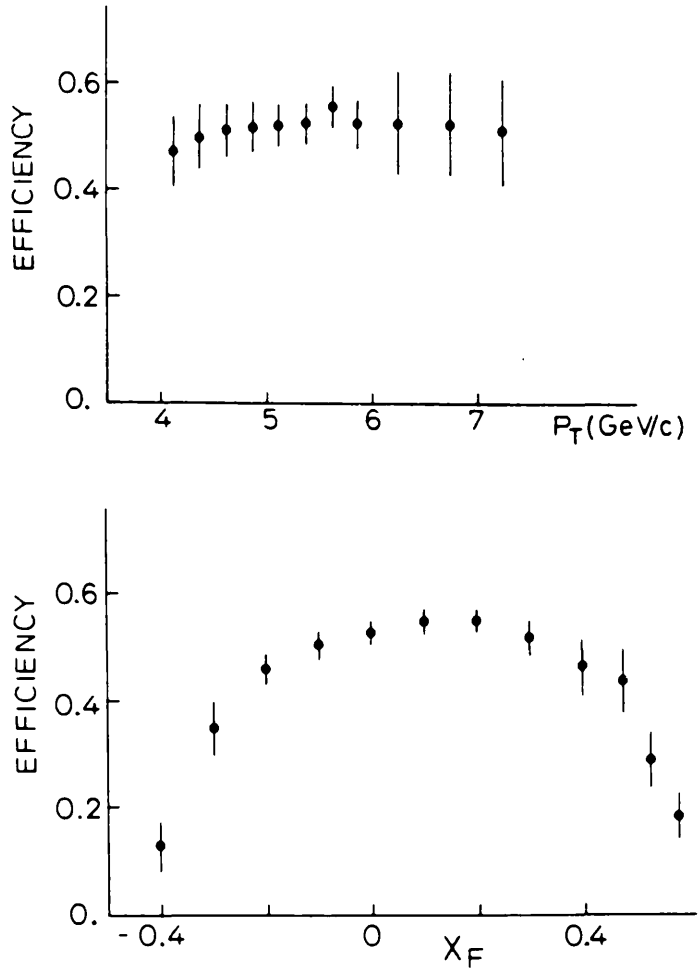

Figure 5.4b

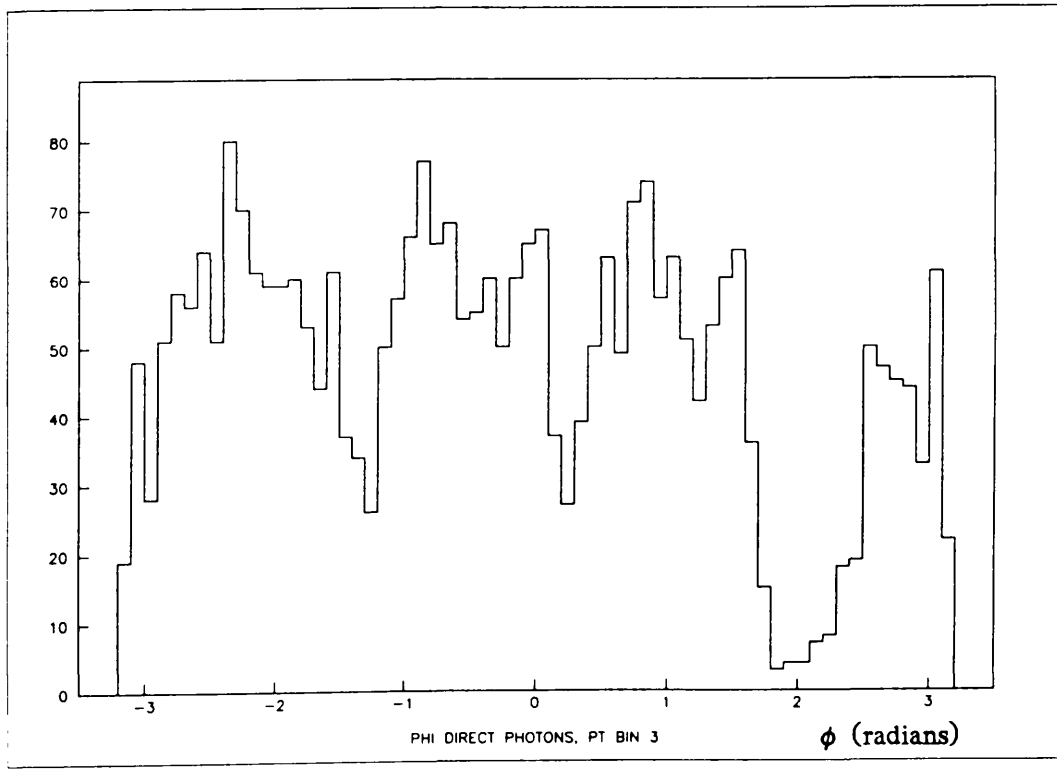

Figure 5.5

Table 5.1 Direct Photon Numbers after Subtraction of Fake Gammas.

xf	Pt (GeV/c) 4.5	4.75	5.0	5.5	6.0	7.0
-0.45						
	152.	106.	64.	4.	11.	
-0.35						
	200.	105.	125.	40.	37.	
-0.25						
	209.	187.	201.	68.	49.	
-0.15						
	398.	238.	203.	66.	64.	
-0.05						
	444.	242.	281.	92.	54.	
+0.05						
	413.	212.	214.	131.	28.	
+0.15						
	416.	297.	251.	113.	11.	
+0.25						
	185.	106.	137.	61.	10.	
+0.35						
	28.	30.	32.	16.	18.	
+0.45						

(Figures to nearest whole number)

Table 5.2 Direct Photon Efficiencies.

xf \ Pt (GeV/c)	4.5	4.75	5.0	5.5	6.0	7.0
-0.45	32.0	48.0	50.0			
-0.35	50.0	88.0	72.0	74.0	55.0	
-0.25	96.0	66.0	68.0	95.0	82.0	
-0.15	71.0	78.0	83.0	78.0	70.0	
-0.05	75.0	75.0	64.0	86.0	79.0	
+0.05	72.0	79.0	70.0	58.0	100.0	
+0.15	66.0	54.0	65.0	67.0	56.0	
+0.25	65.0	70.0	57.0	63.0	76.0	
+0.35	61.0.	55.0	57.0	79.0	52.0	
+0.45						

Efficiencies in percentages.

Table 5.3 π° Efficiencies.

xf \ Pt (GeV/c)	4.5	4.75	5.0	5.5	6.0	7.0
-0.45	26.0	35.0		33.0		
-0.35	87.0	82.0	76.0	91.0	85.0	
-0.25	101.0	72.0	79.0	86.0		
-0.15	105.0	81.0	77.0	73.0	78.0	
-0.05	80.0	66.0	68.0	89.0	62.0	
+0.05	55.0	62.0	67.0	77.0	90.0	
+0.15	55.0	57.0	81.0	76.0	64.0	
+0.25	71.0	57.0	56.0	73.0	74.0	
+0.35	52.0.	51.0	48.0	56.0	71.0	
+0.45						

Efficiencies in percentages.

CHAPTER 6

Single Direct Photon and π^0 Cross-sections.

Having computed the fully corrected event totals, we must now convert these to cross-sections. In this chapter we shall calculate the cross-sections for direct photons and π^0s and compare them with QCD predictions. They will also be compared with those found by previous experiments. Finally, a fit is attempted to describe the pt and xf dependences of the cross-sections, and the γ/π^0 ratio is presented and discussed.

6.1 Cross-section Formulae.

Two types of cross-sections are presented; differential cross sections ($d\sigma/dpt$) and invariant cross-sections ($Ed^3\sigma/dp^3$). The first is given by

$$\frac{d^2\sigma}{dxf\ dpt} = \frac{n_c\ m_p}{n_b\ \rho L \Delta xf \Delta pt}$$

where n_c = fully corrected number of particles seen in each bin,

m_p = the proton mass (938.28 MeV/c^2),

n_b = the total effective number of incident beam particles, corrected for attenuation along the target,

ρ = the density of the target (63 Kg/m^3),

L = the length of the target (1m),

Δpt = the pt range of the bin,

Δxf = the xf range of the bin,

while the second, obtained by integrating over xf, is given by

$$E\frac{d^3\sigma}{dp^3} = \frac{1}{\pi\sqrt{s}}\frac{E_{cms}}{pt}\frac{d^2\sigma}{dxf\ dpt}$$

where E_{cms} is the centre of mass energy of a particle with the mean pt and xf of the particles in the kinematic range of interest.

6.2 The Single Direct Photon Cross-section - Comparison with QCD.

The single direct photon differential cross-sections, calculated using the η_C for each bin and including all the corrections and background corrections described in chapters 4 and 5, are shown in table 6.1. The corresponding invariant cross-sections are shown in table 6.2. Fig. 6.1 shows the invariant cross-section for single direct photons with |xf| < 0.45 versus pt together with the predictions made by QCD using both set I and set II Duke and Owens structure functions. Set II are clearly ruled out by the WA70 results.

The direct photon cross-section for the pt range 7.0→8.0 GeV/c is shown on fig. 6.1. The large error bars on this point were caused by uncertainty about the effects of the muon halo above 7.0 GeV/c. The equivalent cross-section for π^0s is shown on fig. 6.6, and the resulting γ/π^0 ratio for the 7.0→8.0 GeV/c pt range in figs. 6.11a and 6.11b. These points were not used in the fits and parametrisations described below.

In table 6.3 the direct photon cross sections are shown again, but with xf intervals of 0.3 instead of 0.1. Figures 6.2a, b and c show the direct photon cross-sections for the xf regions -0.45 < xf < -0.15, |xf| < 0.15, and +0.15 < xf < 0.45 respectively. The central xf region shows a similar pattern to the integrated xf cross-section shown in fig. 6.1, i.e. the data points are slightly above the set I predictions while the set II predictions are ruled out. The set II predictions are

also ruled out by the positive xf bins, though the data points lie slightly below the exact set I prediction. In the three most negative xf bins, however, the '86 cross-section is considerably higher with respect to the set I/set II predictions than we would expect. Indeed, the cross-section here agrees closely with set II while set I are ruled out. This effect is not yet understood, though an independent (preliminary) analysis of the '86 data at the University of Geneva showed the same high measurements at high negative xf.

In figs. 6.3a-e, the direct photon cross-sections are shown against xf for the five pt bins 4.5 → 4.75, 4.75 → 5.0, 5.0 → 5.5, 5.5 → 6.0 and 6.0 → 7.0 GeV/c respectively. Also shown on these figures are the results of the parametrisations described below in section 6.5

Recently, Aurenche at al [58] compared complete beyond leading logarithm QCD calculations with the most precise high pt direct photon data ('84/'85 WA70 data [55], NA24 [30], R806 [59]) and Deep Inelastic Scattering (DIS) data (BCDMS) [60]. They found that as well as providing a measurement of Λ_{QCD}, the direct photon cross-section data could be used to constrain very effectively the gluon distribution function for the proton (specifically the parameter η_g in the chosen distribution function $xg(x) = (1-x)\eta g$). The value arrived at after a best fit to the 1984/'85 WA70 $pp \rightarrow \gamma X$ data was $\eta_g = 3.76 \mp 0.37$ at $Q^2=2$ GeV/c. The χ^2 of fits to the DIS and direct photon data as a function of η_g are shown in fig. 6.4.

Aurenche et al noted that the DIS data could be used to constrain the value of Λ_{QCD}, as well as providing a weak constraint on η_g. By combining the two (independent) sets of data they found that the uncertainty in measurement of all these parameters could be greatly reduced. The plot illustrating this is shown as fig. 6.5a. The dashed error ellipses indicate one standard deviation and the full ellipses take into account systematic errors added in quadrature to statistical errors. Taken together the data pinpoint the most likely region of the η_g /Λ_{QCD} plane

with much greater accuracy than the individual experiments can. This region is enlarged in fig. 6.5b and error ellipses corresponding to χ^2=1.0 and χ^2=4.61 (i.e. a confidence level of 90%) are shown. The value of Λ_{QCD} quoted by Aurenche et al is 230 $\mp$17 ($\mp$50) MeV, and that for η_g is 3.90 $\mp$ 0.11 (+0.8/-0.6).

6.3 Comparison with the 1984/85 Direct Photon Data: Normalisation.

To compare the absolute cross-sections measured in the '84/'85 runs with those from the present analysis, we use the binning of table 6.3. The '86 cross-sections for this binning, together with the ratio R= σ('86)/σ('84/'85) for each bin, are shown as table 6.4 (direct photons).

The absolute agreement between the two data sets is close in the central |xf| < 0.15 bins (i.e. the region with highest statistics), where the weighted average of R is 1.00 $\mp$ 0.017. In the two outer xf regions absolute agreement between the two data sets is not good at first sight; the weighted average for R is 0.934 $\mp$ 0.033 in the region with +0.15 < xf < +0.45 and 1.487 $\mp$ 0.043 in the region with -0.45 < xf < -0.15. This is to be expected however, bearing in mind the changes made to the muon halo correction factors for the '86 analysis.

In the '84/'85 analysis the correction factors were taken to vary little with xf, between 1.137 at high negative xf and 1.071 at high positive xf. The study by the University of Geneva group using specially processed tapes (see section 4.4.2) found the correction factors to vary considerably more than this, as illustrated in fig. 4.8. They were typically 1.03 at high positive xf and 1.3 or more at high negative xf. The average correction factor employed in the xf region from +0.45 to +0.15 was 1.023 and in the corresponding negative xf region 1.31. We would therefore expect the '86 cross sections in the three most negative xf bins to be a

factor of 1.31/1.137 = 1.15 higher than those measured in '84/'85, and in the three most positive xf bins 1.0234/1.071 = 0.955 lower. The latter of these expectations is fulfilled almost exactly, 0.938 $\mp$ 0.033 to 0.955, but the '86 cross-sections in the three most negative xf bins are still higher than those measured in '84/'85 by a factor of 1.28 $\mp$ 0.04. This is most easily explained by differences in the direct photon recognition efficiencies measured using Monte Carlo programs as described in chapter 5. The number of Monte Carlo events with very high or low xf is, of course, limited and the possible error in the efficiencies used for these regions are therefore large.

6.4 The π^0 Cross-section - Normalisation with '84/'85.

The differential cross-sections for the π^0s, after all corrections described in chapters four and five have been applied to the raw numbers, are shown in table 6.5 and the invariant cross-sections are shown in table 6.6. In fig. 6.6 the π^0 cross section integrated over xf is shown versus pt. A linear fit to the data points is also shown, though it is apparent that the slope increases after a pt of approximately 4.5 GeV/c. This is another effect of the '86 trigger problem.

Comparing the '86 π^0 cross-sections with those of the '84/'85 analysis clearly reveals a problem in the lower (pt = 4.0 → 4.5 Gev/c) region. The π^0 invariant cross-sections for the large (0.3) xf bins used in tables 6.3 and 6.4 above is shown in table 6.7, and the ratio $R=\sigma('86)/\sigma('84/'85)$ is shown in table 6.8 in the same large binning. The discrepancies get progressively worse towards positive xf and low pt. This corresponds to the area closest to the beamhole on the calorimeter. In the bin with a pt 4.0 to 4.25 GeV/c and xf +0.15 to +0.45 (the worst case) the ratio R is equal to 0.472. There is some evidence that the the pt region 4.5 to 4.75 GeV/c has also been affected by the trigger problem. This is provided by examining the weighted average of R for negative, central and positive xf for the bins above 4.5 GeV/c and 4.75 GeV/c. One would expect to see the effect of the

'86 halo correction factors manifested; an extra factor of 1.31 in the negative xf region and 0.93 in the positive xf region. In the central xf region the ratio R should be approximately 1.0. The weighted R averages are;

xf	-0.45→-0.15	-0.15→+0.15	+0.15→+0.45
R, pt > 4.5	1.046	0.890	0.869
R, pt > 4.75	1.278	0.967	0.864

The expected shifts are seen in the negative and central xf regions only above pt = 4.75 GeV/c. There is however, no change in the positive xf region.
For the π^0 parametrisation described below, the two lowest pt bins were not used.

The π^0 cross-sections are shown versus pt for the negative, central and positive xf regions in figs. 6.7a-c respectively. Linear fits to the points above pt=4.5 GeV/c are superimposed on each figure.

The π^0 cross sections for the five pt bins between 4.5 and 7.0 GeV/c are shown against xf in figs. 6.8a-e respectively. Also shown on these figures are the results of the parametrisation described in the next section.

6.5 Comparison with the 1984/85 Data: Parametrisation.

The parametrization used in the WA70 direct photon publications [88] for the '84/'85 data has been adopted. This is;

$$E(d\sigma^3/dp^3) = C(1-x_D)^m /(pt/p_0)^{2n}$$

where $x_D = \sqrt{((x_T^2 + (xf-x_0)^2))}$, $xt=2pt/\sqrt{s}$ and $p_0 = 1$ GeV/c.

A least squares fit was performed with C, x_0, m and n as free parameters. The result of the fits for both direct photons and π^0s are shown in tables 6.9 and 6.10, together with the parametrisations made of the '84/'85 WA70 direct

photon and π^0 data. It should be noted that these parameters are not orthogonal and the correlation matrix for direct photons and π^0s, for both data sets, are given in the figures.

The direct photon cross-section was found to fall more steeply with pt in the '86 data than in '85, with the parameter n equal to 3.61 $\mp$ 0.002 against 3.28 $\mp$ 0.19. The discrepancy may be accounted for by a small and possibly undetectable trigger problem in the '84/'85 data. The '84/'85 data extended downwards in pt to 4.0 GeV/c, while the '86 data is reliable only above 4.5 GeV/c, for the reasons described above in section 5.3. Any underestimation of the lower bins in the '84/'85 data will soften the pt dependence.

The '86 xf dependence is slightly harder than that of the '84/'85 data, the two values for the parameter m being 3.71 $\mp$ 0.02 and 3.34 $\mp$ 0.19. This is probably connected with a discrepancy in the parameter x_0, arising from the direct photon cross-section in the '86 data being displaced towards negative xf by approximately 0.09 with respect to the '84,'85 data sample. The x_0 parameter has moved from 0.056 $\mp$ 0.007 to -0.0305 $\mp$ 0.0045. The direct photon cross-section is plotted against xf for the two pt bins 4.5 $\rightarrow$ 5.0 GeV/c and 5.0 $\rightarrow$ 6.0 in figures 6.9a and 6.9b. The corresponding distribution from the '84/'85 analysis is also shown on fig. 6.9b, though the change in lower pt limit does not permit us to do the same for the first figure. In the direct photon case, the shift in xf indicated by the parametrisation would seem to be due principally to differences in the xf bin -0.25 $\rightarrow$ -0.15. The '86 cross-section in this bin is higher than that in the '84/'85 analysis, and causes the central peak to be extended downwards in xf, naively by the width of one bin i.e. 0.1. The shift measured quantitatively by the parametrisation was 0.0865. Though there may be an unknown, though small, systematic shift in xf, the difference between the two data sets is small enough to be ascribable to normal statistical variation.

QCD predictions are that the distribution should be peaked at a low positive xf.

In fig. 6.10 the cross-section variation in xf of figure 6.9b is shown with the predictions made using Duke and Owens set I and set II structure functions. Neither set fits the data well, set I being in good agreement in the central xf region and set II at low xf.

The parametrisations of the π^0 distribution (based on the upper five pt bins only) differ slightly in the pt dependence, 4.51 $\mp$ 0.04 ('86) against 4.84 $\mp$ 0.05 ('84/'85), though this could have been caused by the suspected trigger problem in the 4.5 to 4.75 GeV/c bin discussed above. The xf dependences do not agree well, 4.77 $\mp$ 0.10 ('86) to 3.82 $\mp$ 0.07 ('84/'85). The value of m reached when all seven pt bins are included was 4.12 $\mp$ 0.08, considerably closer to the '84/'85 value. The trigger problem in the 4→4.5 GeV/c region may only effect the shape of the cross-section with respect to pt, leaving its xf dependence preserved.

The midpoint of the xf distribution shows a similar small shift towards negative xf as seen in the direct photon parametrisations, -0.027 $\mp$ 0.001 ('86) to +0.063 $\mp$ 0.002 ('84/'85).

In short, the parametrisation of the '86 data does not show the improvement over the '84/'85 parametrisation which one might have expected given its statistical superiority because the trigger problem has caused the two lowest bins, which contain the highest statistics and therefore have the lowest errors, to be discarded. These bins were included in the parametrisation of the '84/'85 data, with a consequential lowering of errors.

In summary, the direct photon and π^0s parametrisations of the '84/'86 and '86 data sets are compatible apart from a small systematic shift in the cross-section of approximately 0.075 towards negative xf. This was possibly due to either the trigger threshold problem or the quadrant two 'hole'.

The '86 parametrisation, based on data with an inherent statistical superiority, has statistical errors smaller than that of '84/'85, and while the wings of the xf

distributions may have systematic problems, the central xf region is entirely compatible with the '84/'85 data and statistically dominates over the wings. The '86 data is an improvement on that of '84/'85.

6.6 The γ/π^0 Ratio.

In fig. 6.11a the γ/π^0 ratio is shown against pt. As expected from theory, it rises continuously with pt. Also shown, as figure 6.11b is the '86 measurment with that of '84/'85. In '84/'85, the higher pt bins had very large statistical errors and the γ/π^0 ratio was observed to fall between the bins 5.0 → 5.5 GeV/c and 5.5 → 6.0 GeV/c. The '86 measurement benefited from increased statistics allowing the pt range to be extended 8.0 GeV/c.

6.7 Comparison with Contemporary Direct Photon Experiments.

In fig. 6.12 the WA70 direct photon cross-section is shown vs. pt together with the results from the experiment NA24, which used π^-,π^+ and proton beams on a carbon target at a $\sqrt{s}$ of 24.3 GeV. NA24 was essentially an upgrade of the NA3 apparatus. Their data (published in 1987 [30]) was not accurate enough to allow a reliable judgement between Duke and Owens set I and set II structure functions. Their resuts are compatible with the WA70 results presented here, though their statistical errors are 5-6 times larger. The statistical error bars on the WA70 points are too small to be seen on the scale used in fig. 6.12. Background from $\pi^0 \rightarrow \gamma\gamma$ decays was a large problem for NA24 at transverse momenta of less than 4 GeV/c and the errors on their lower data points are larger than those in the mid pt range.

The γ/π^0 ratio observed varies with the $\sqrt{s}$ of the experiment, so direct comparison between experiments is not possible.

ellipses are at 1 standard deviation.

Figure 6.5b Error ellipses corresponding to $\Delta\chi_{TOT}{}^2=1$ and $\Delta\chi_{TOT}{}^2=4.61$ (90% confidence level). The dashed contour is the $\Delta\chi_{WA70}=1$ contour shown in figure 6.5a.

Figure 6.6 π° invariant cross-section versus pt, xf<0.45.

Figure 6.7 π° invariant cross-sections versus pt,
a) for -0.45 < xf < -0.15,
b) for -0.15 < xf < 0.15, and
c) for 0.15 < xf < 0.45.

Figure 6.8 π° invariant cross-sections versus xf,
with parametrisation (dashed line),
a) for pt bin 1, 4.5 < pt < 4.75 GeV/c,
b) for pt bin 2, 4.75 < pt < 5.0 GeV/c,
c) for pt bin 3, 5.0 < pt < 5.5 GeV/c,
d) for pt bin 4, 5.5 < pt < 6.0 GeV/c, and
e) for pt bin 5, 6.0 < pt < 7.0 GeV/c.

Figure 6.9 Direct photon invariant cross-sections versus xf,
a) for 4.5 < pt < 5.0 GeV/c, '86 data,
b) for 5.0 < pt < 6.0 GeV/c, '86 data and '84/'85 data, and
c) for 5.0 < pt < 6.0 GeV/c, '86 data, together with QCD predictions made using Duke and Owens set I and set II structure functions.

Figure 6.9b Direct photon invariant cross-sections versus xf,

Figure 6.10 Direct photon invariant cross-sections versus xf,

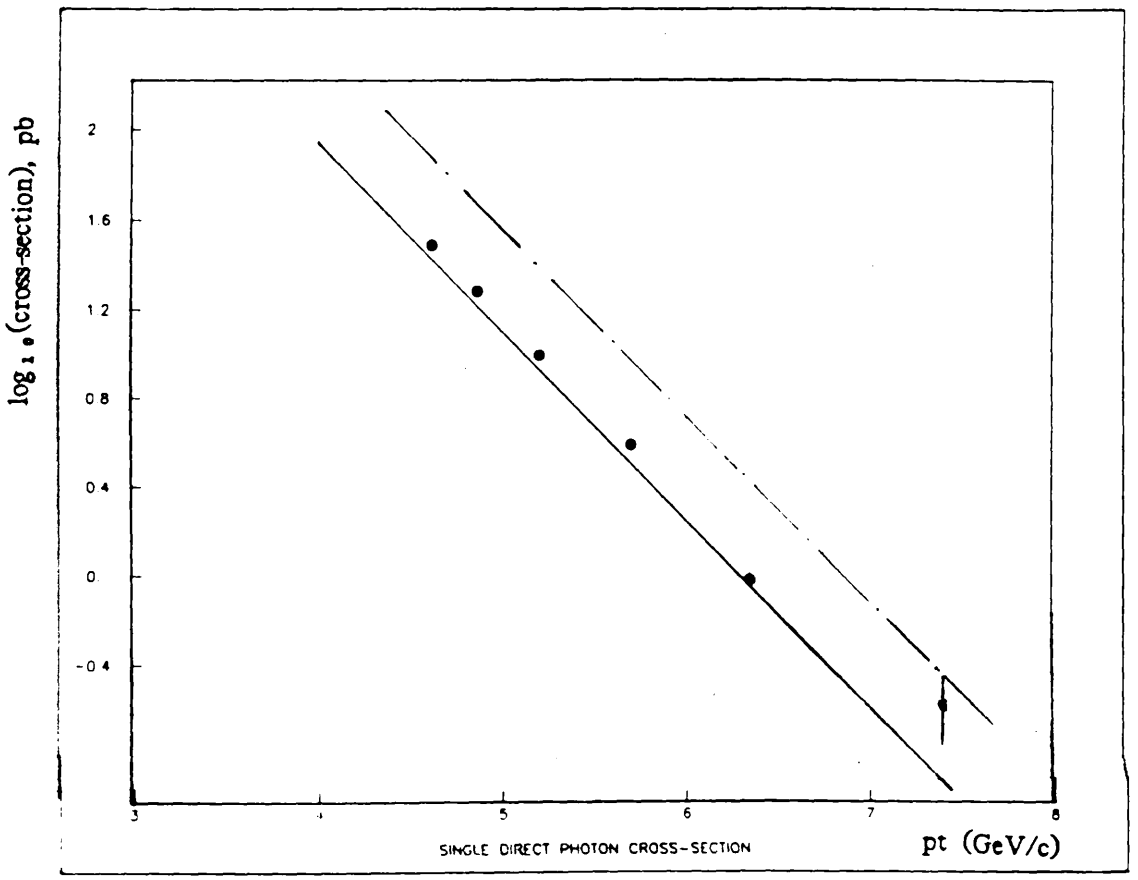

Figure 6.1

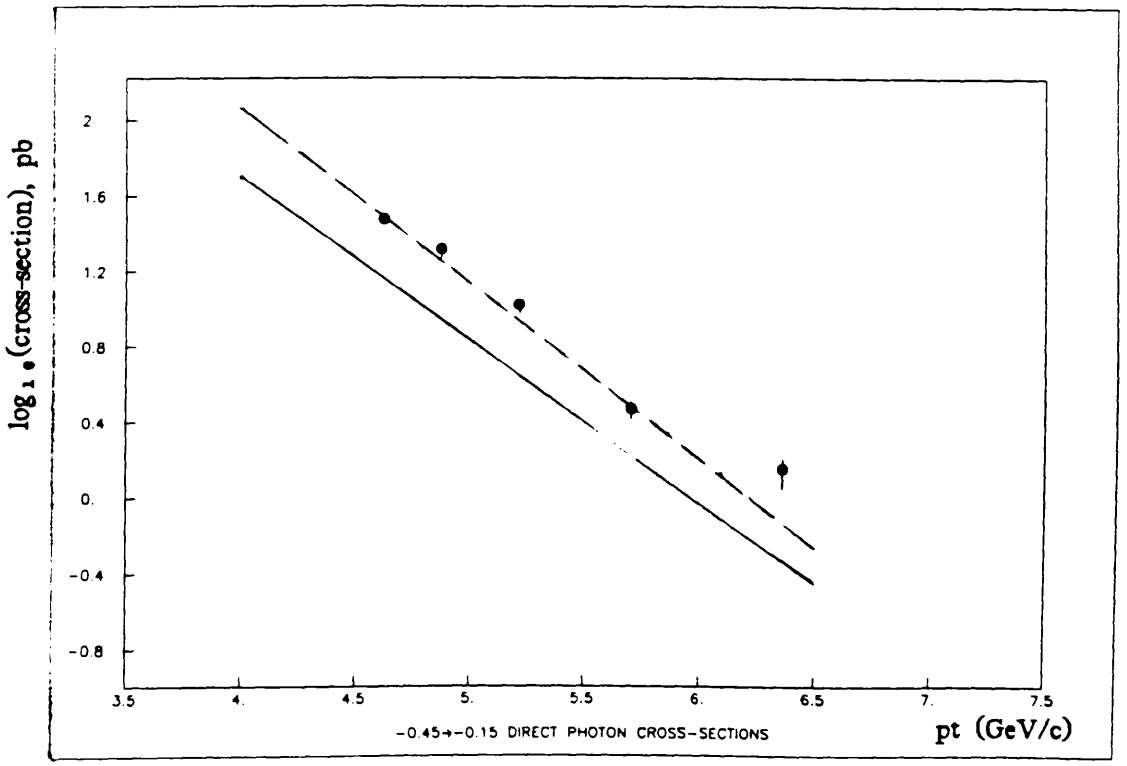

Figure 6.2a

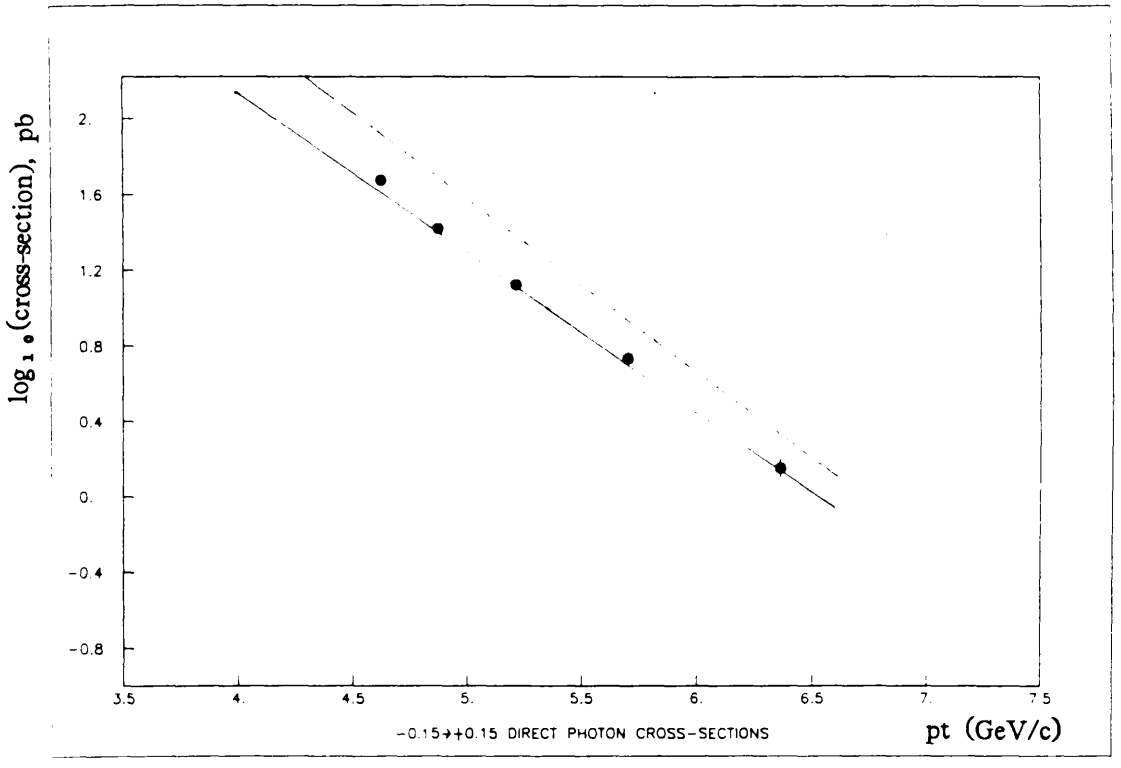

Figure 6.2b

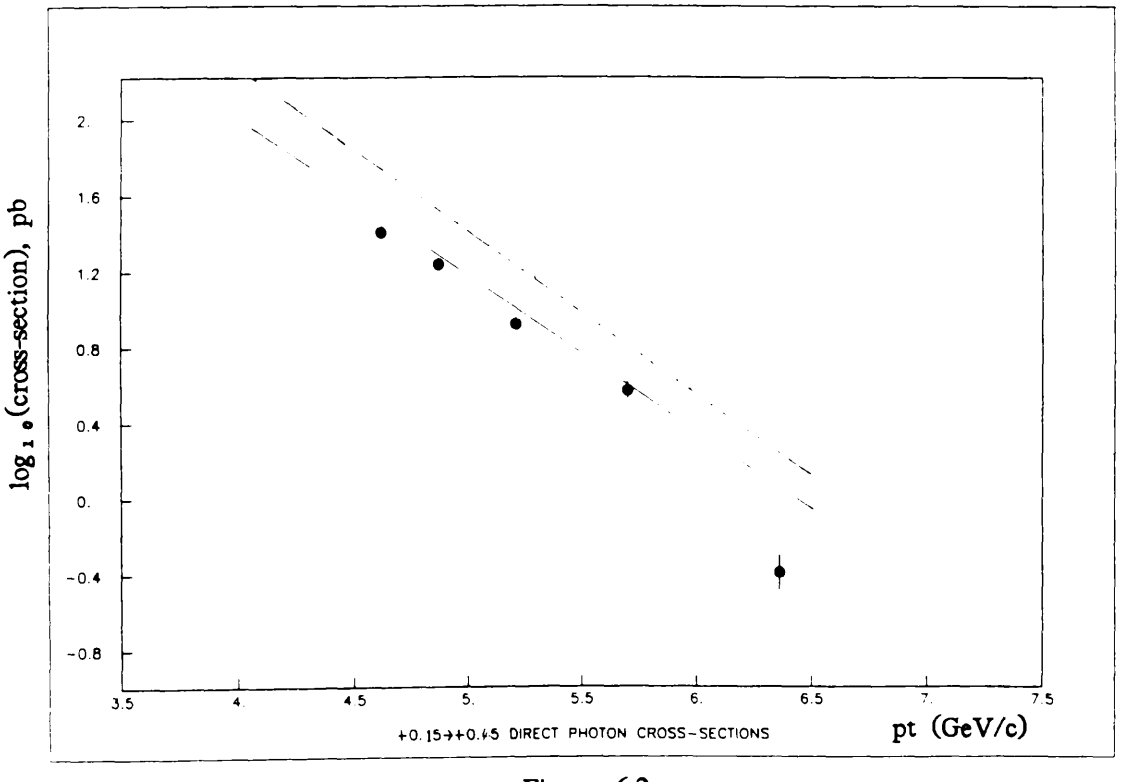

Figure 6.2c

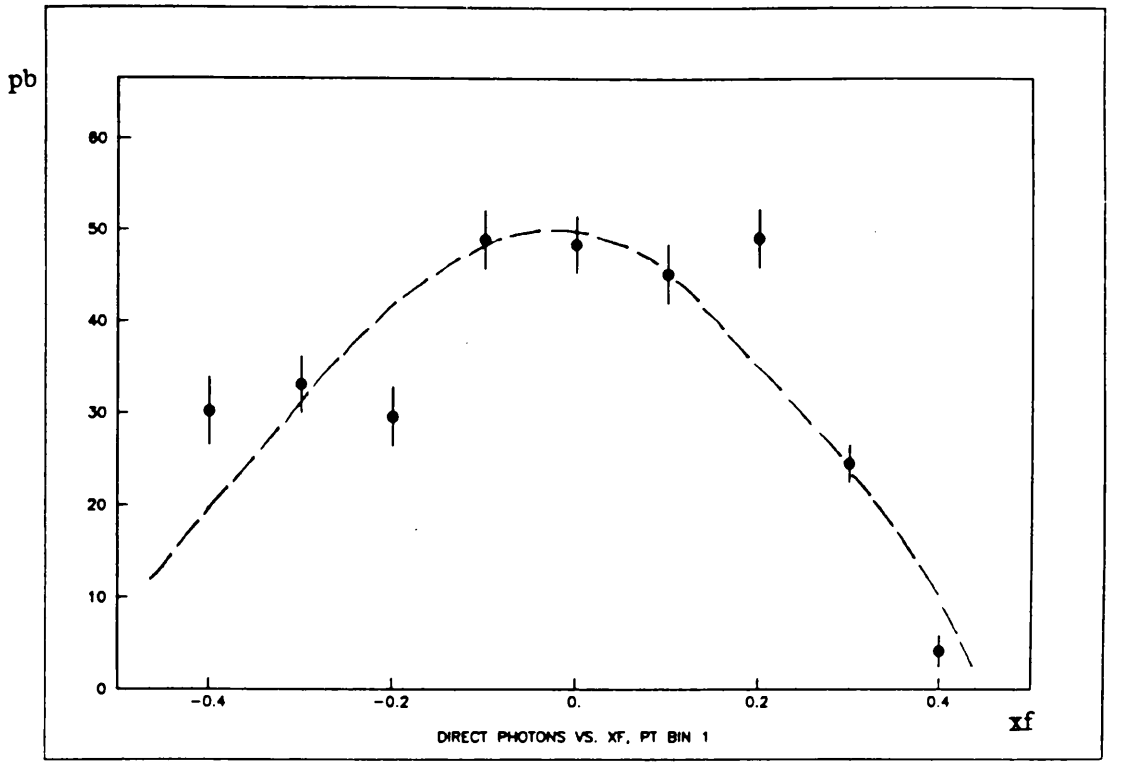

Figure 6.3a

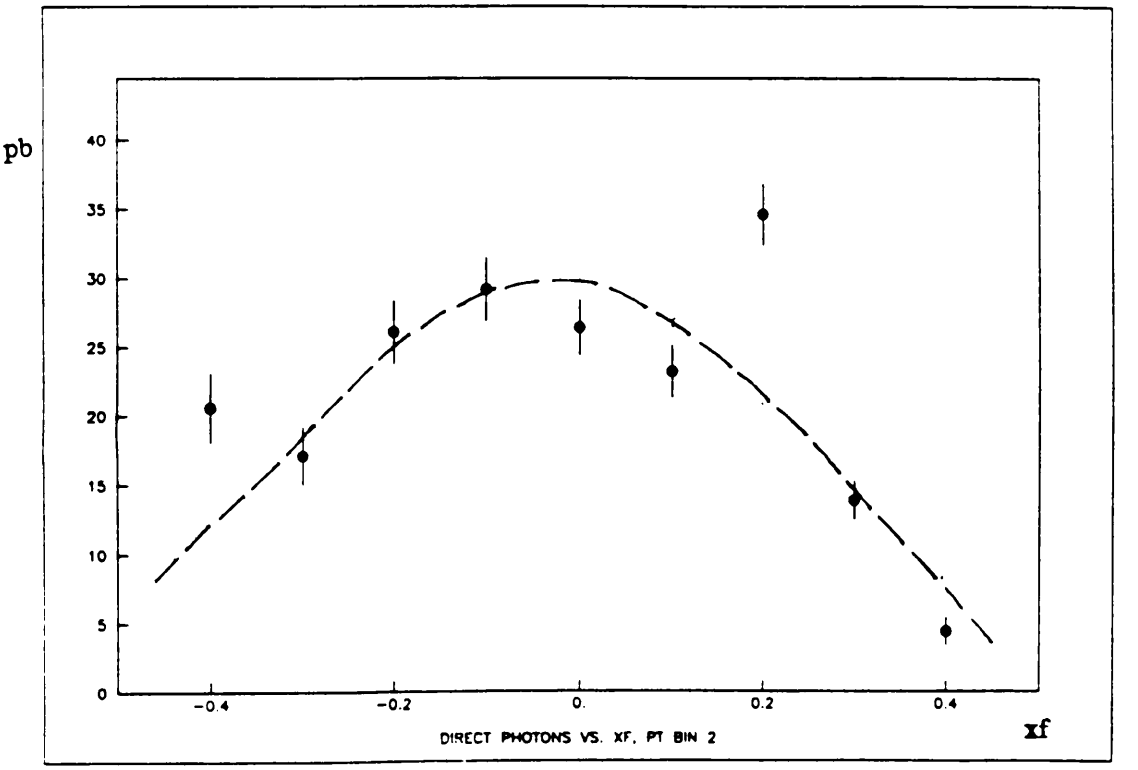

Figure 6.3b

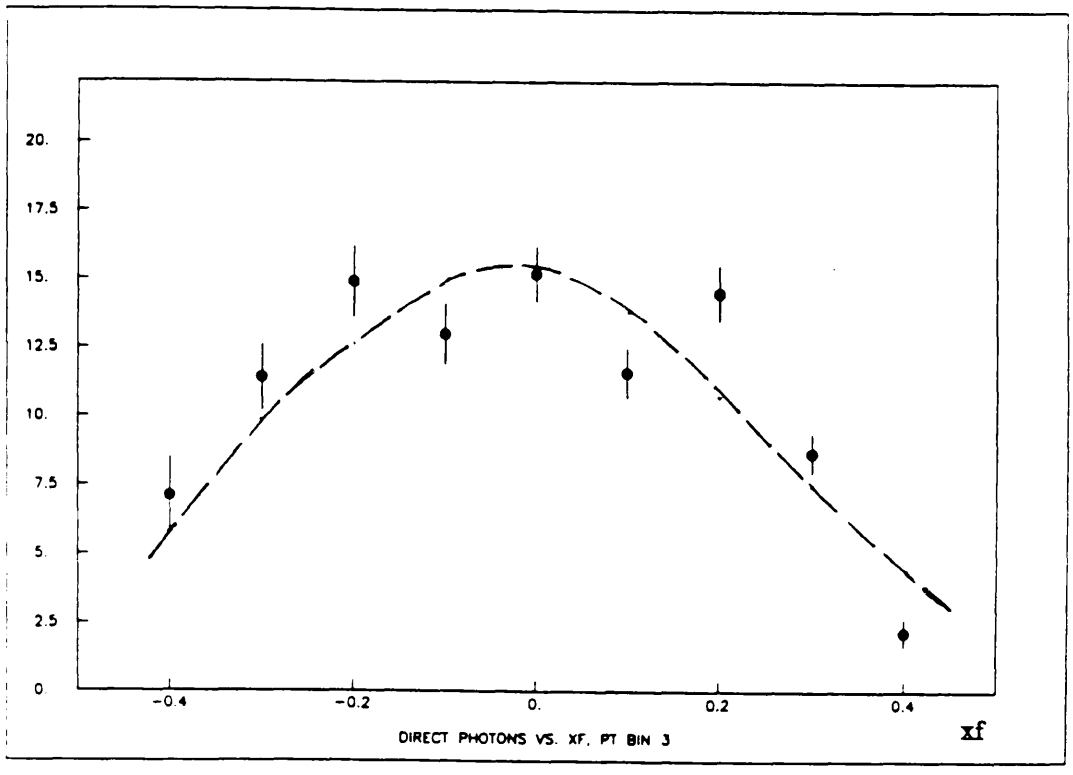

Figure 6.3c

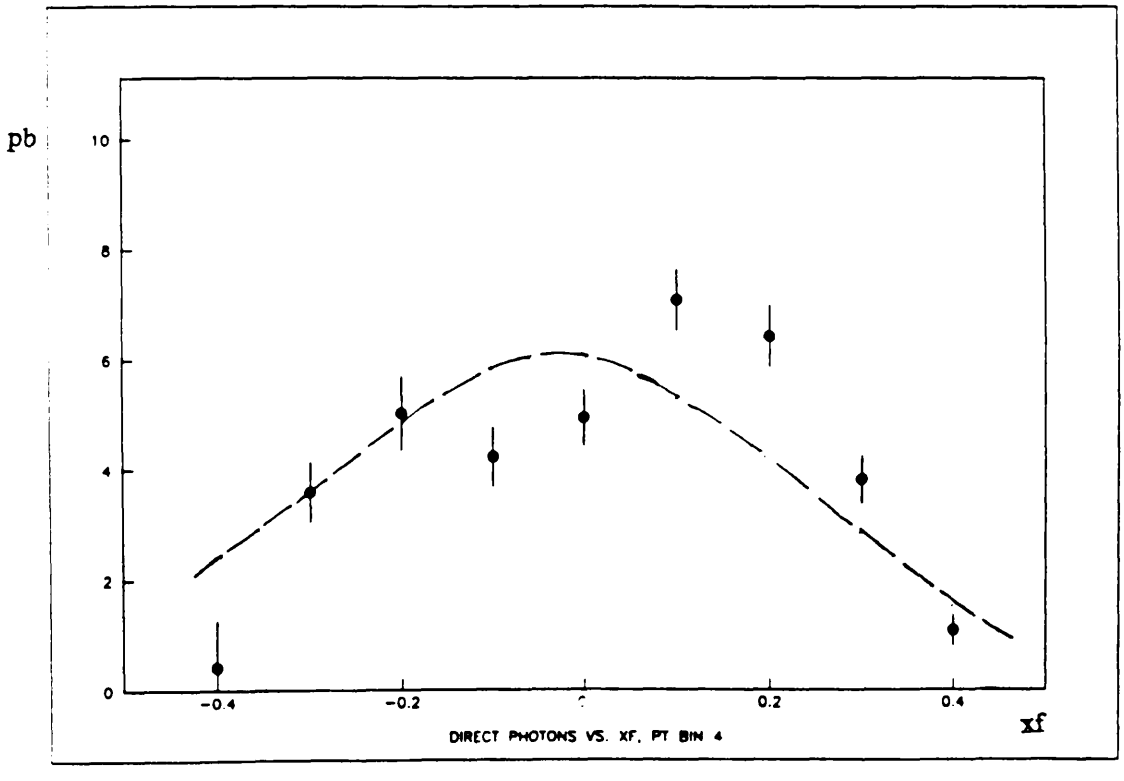

Figure 6.3d

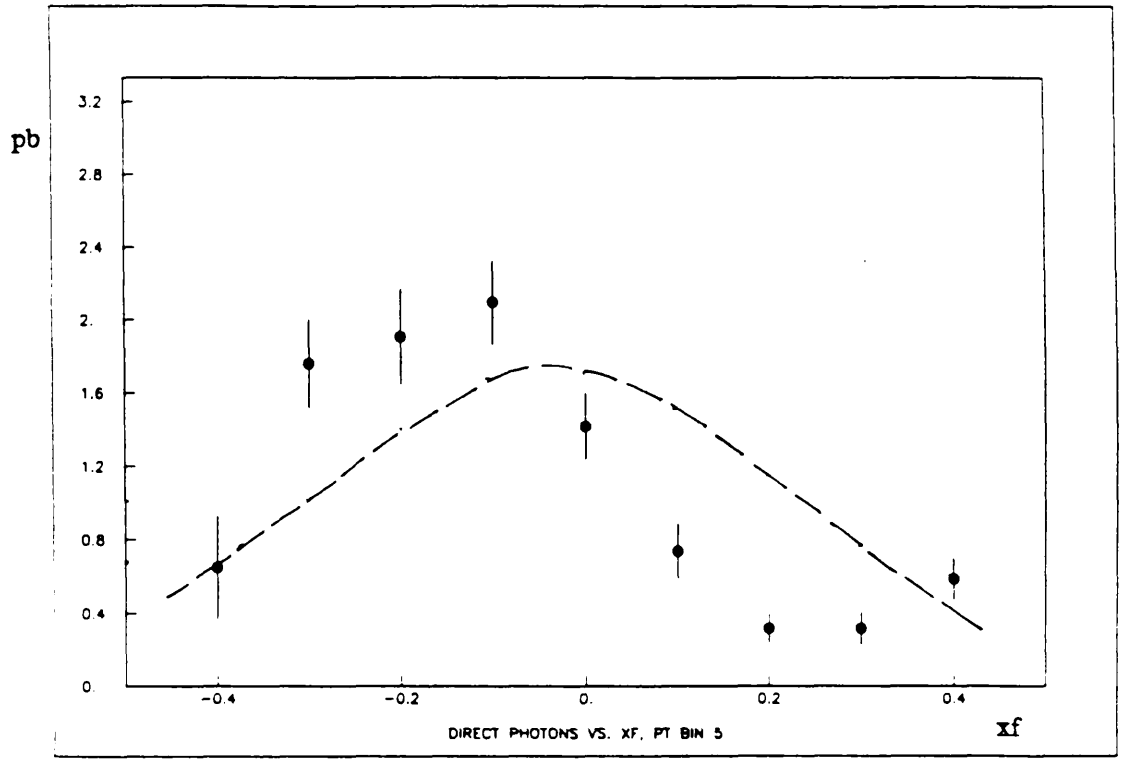

Figure 6.3e

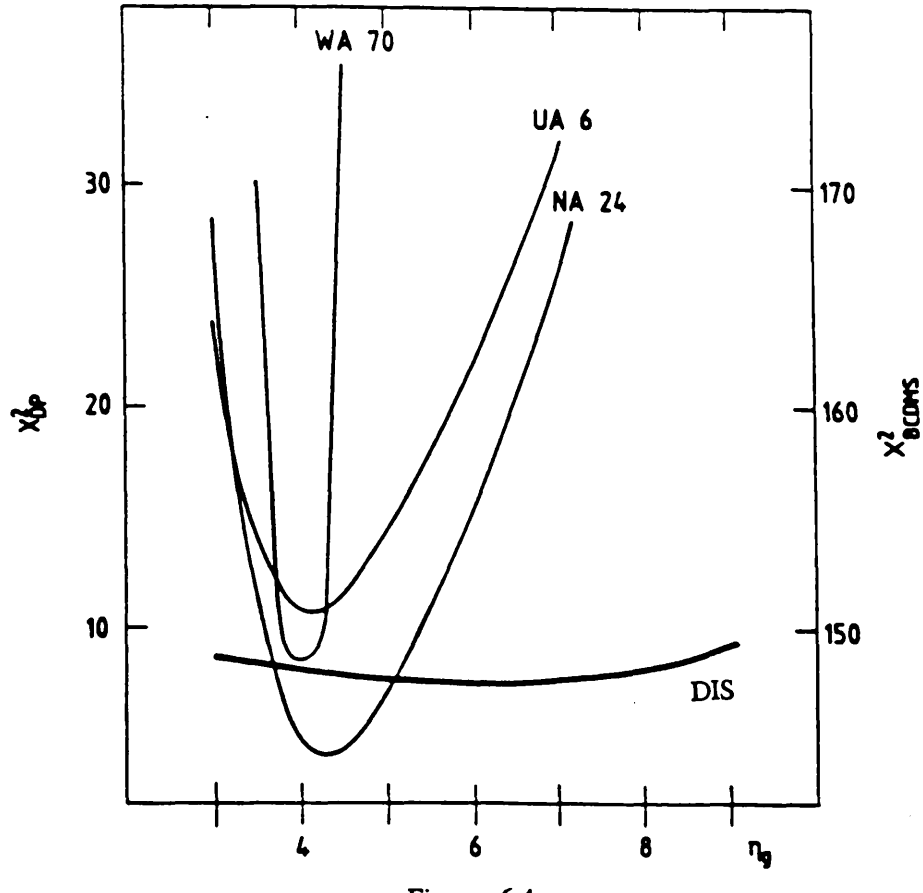

Figure 6.4

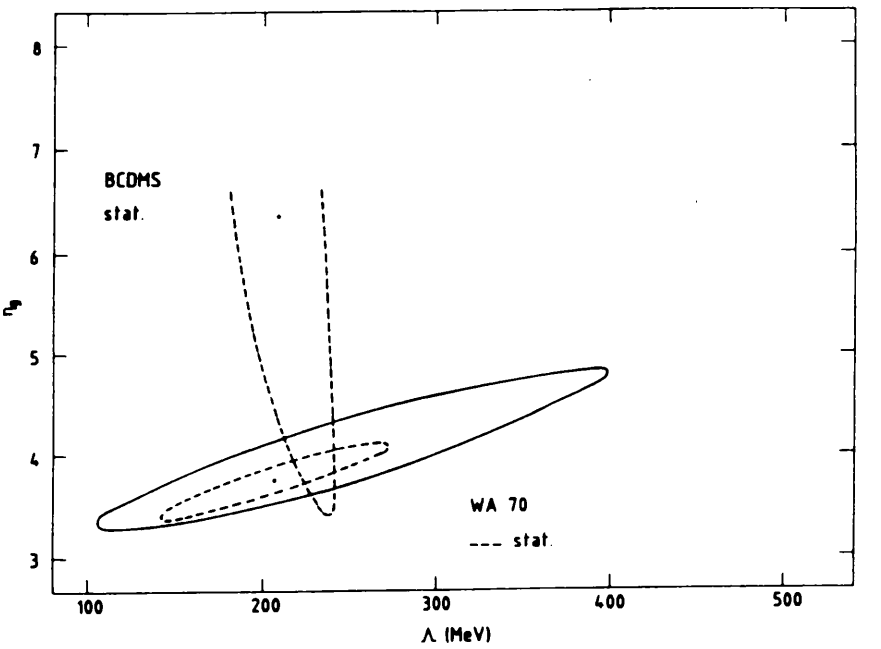

Figure 6.5a

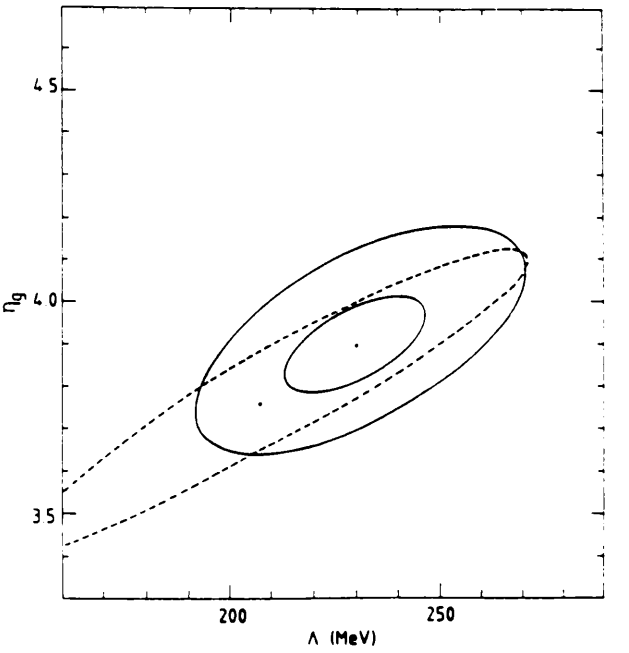

Figure 6.5b

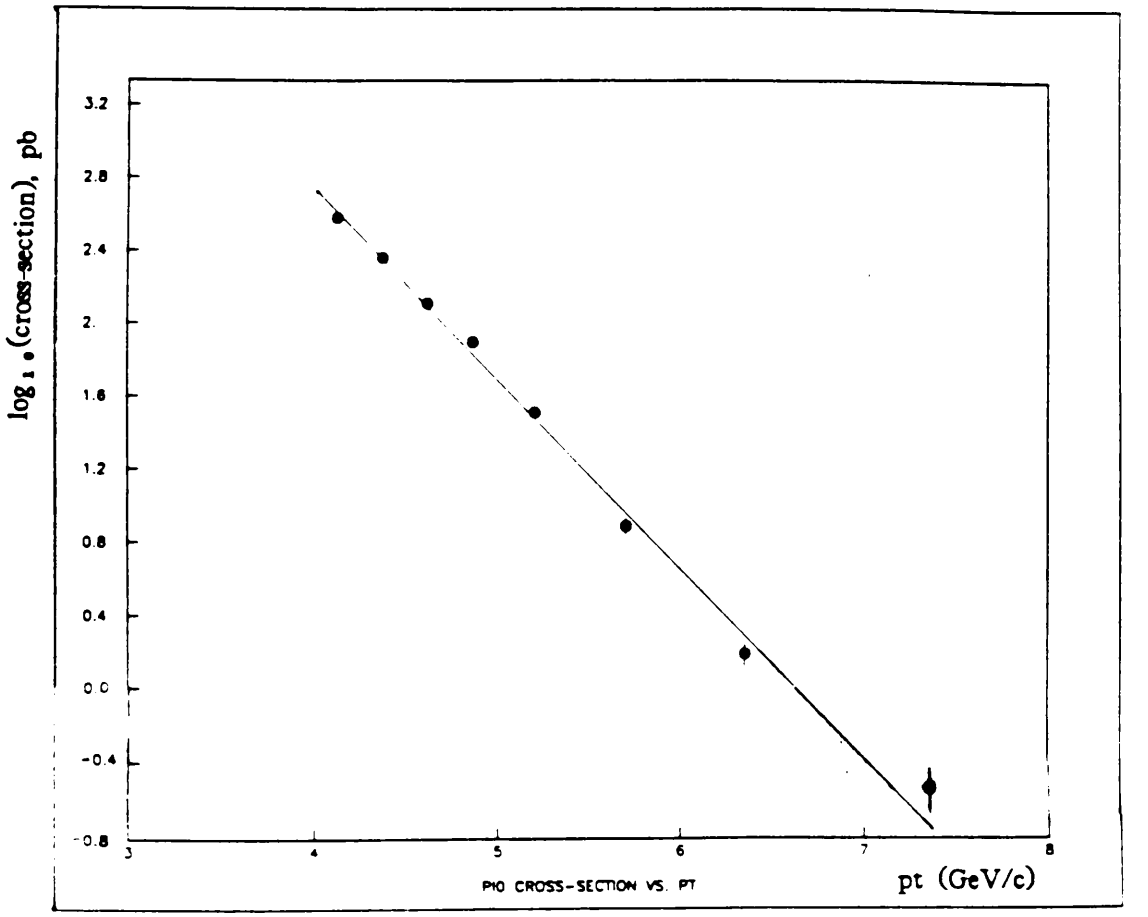

Figure 6.6

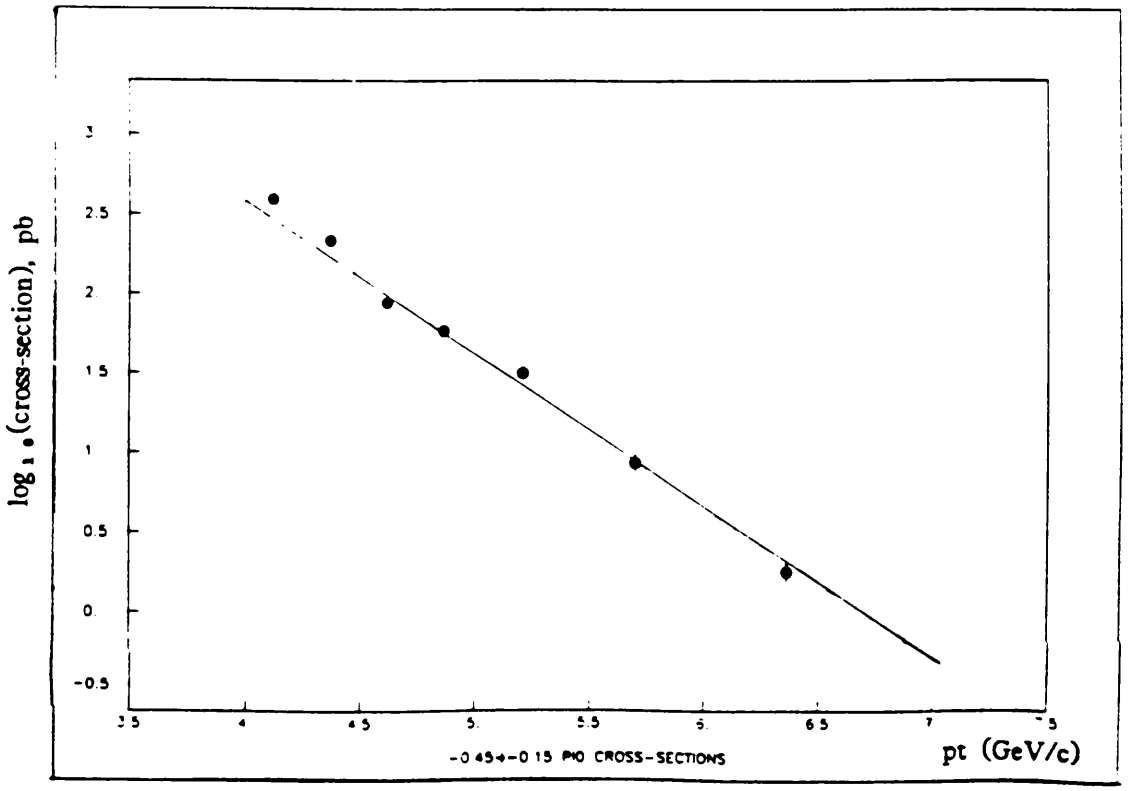

Figure 6.7a

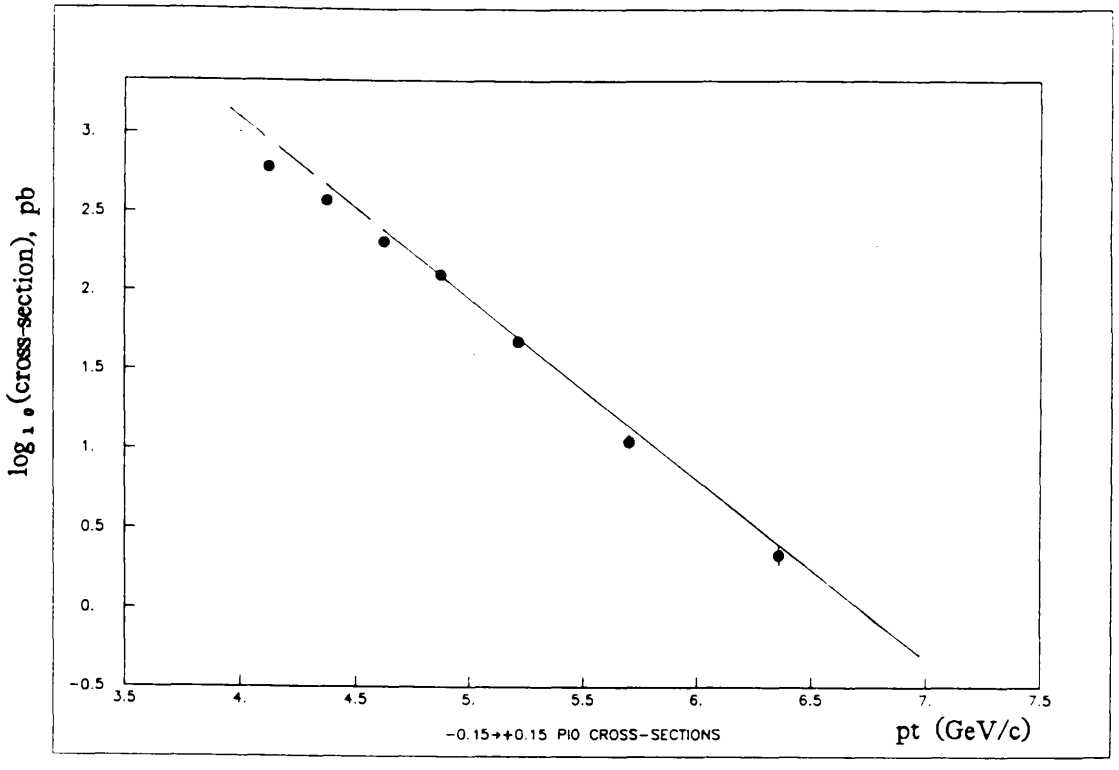

Figure 6.7b

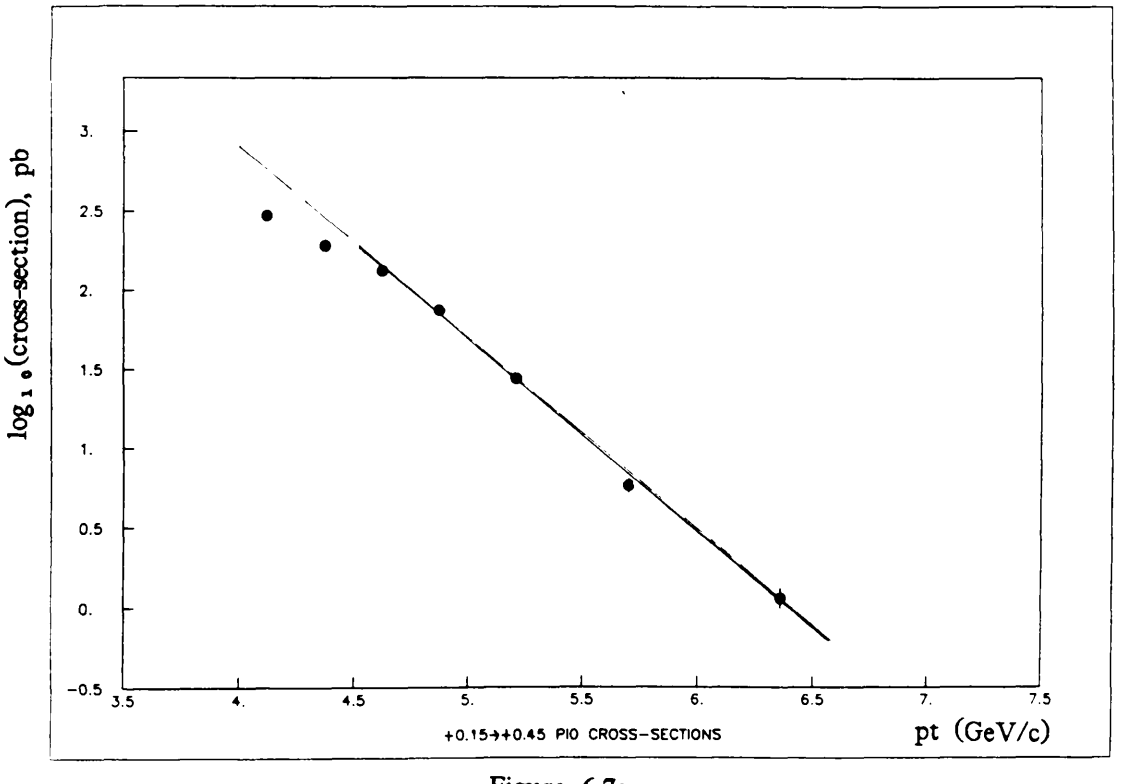

Figure 6.7c

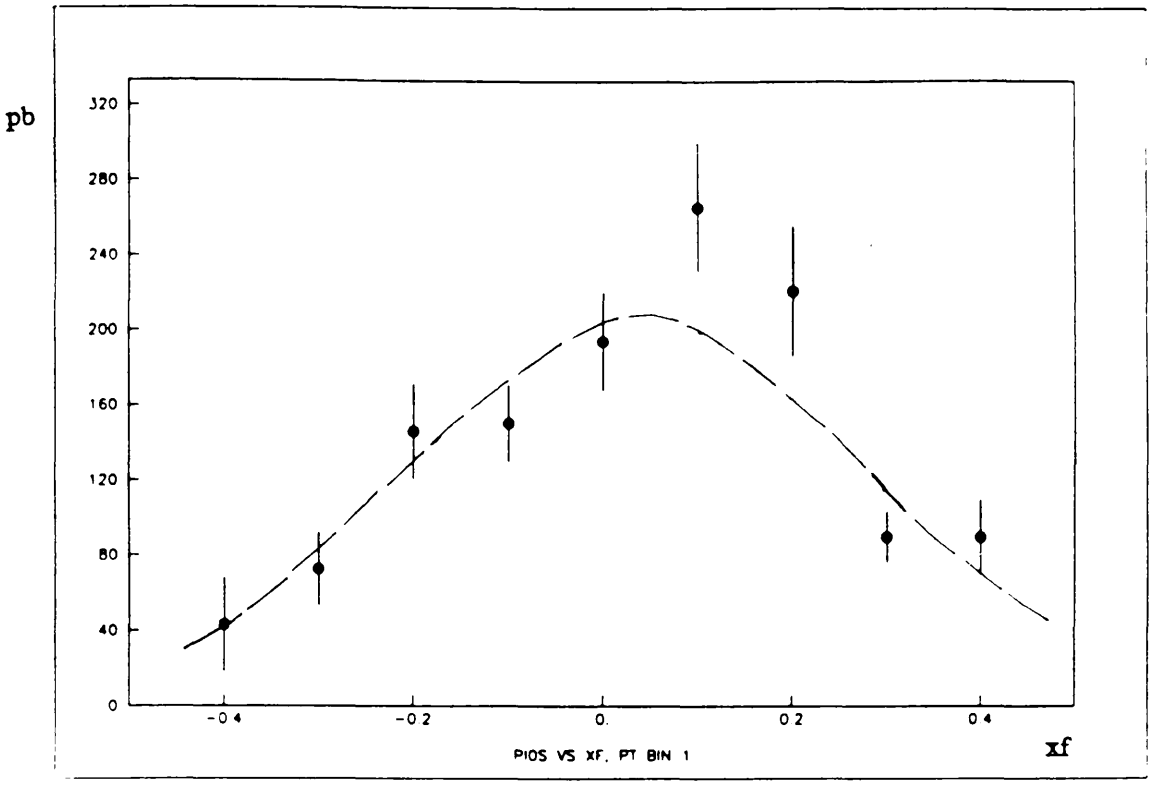

Figure 6.8a

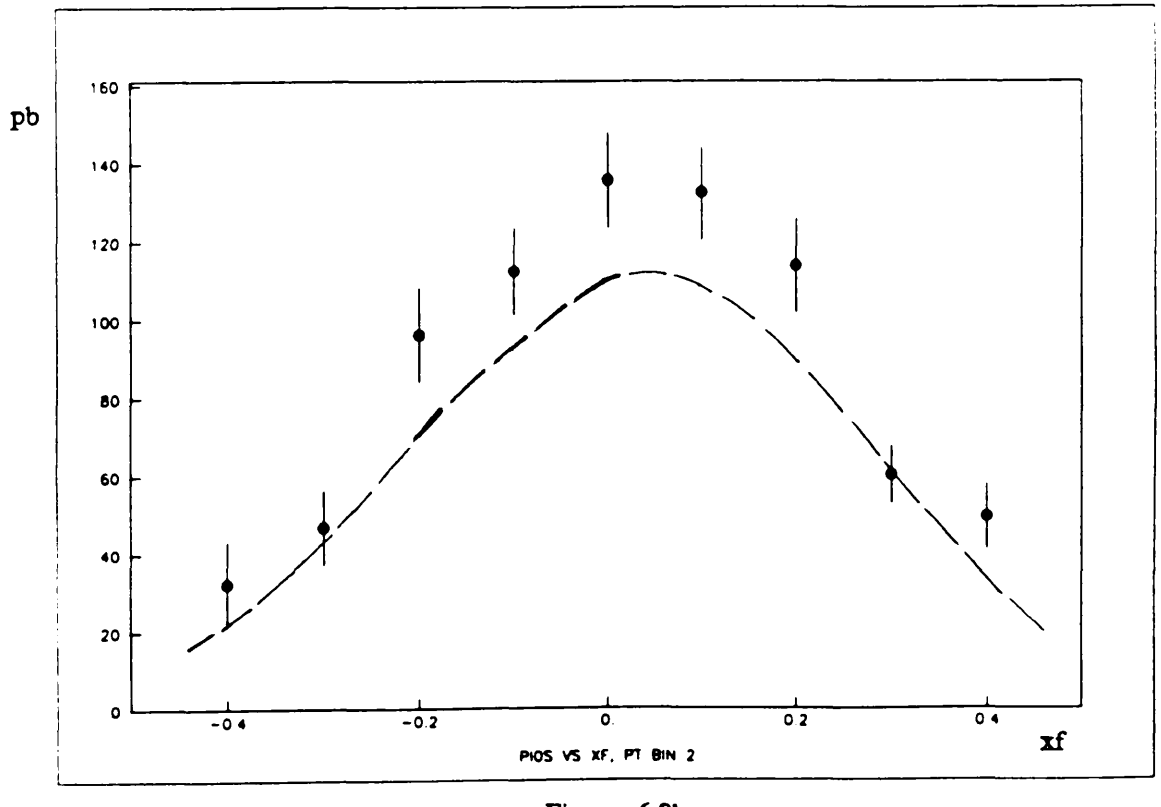

Figure 6.8b

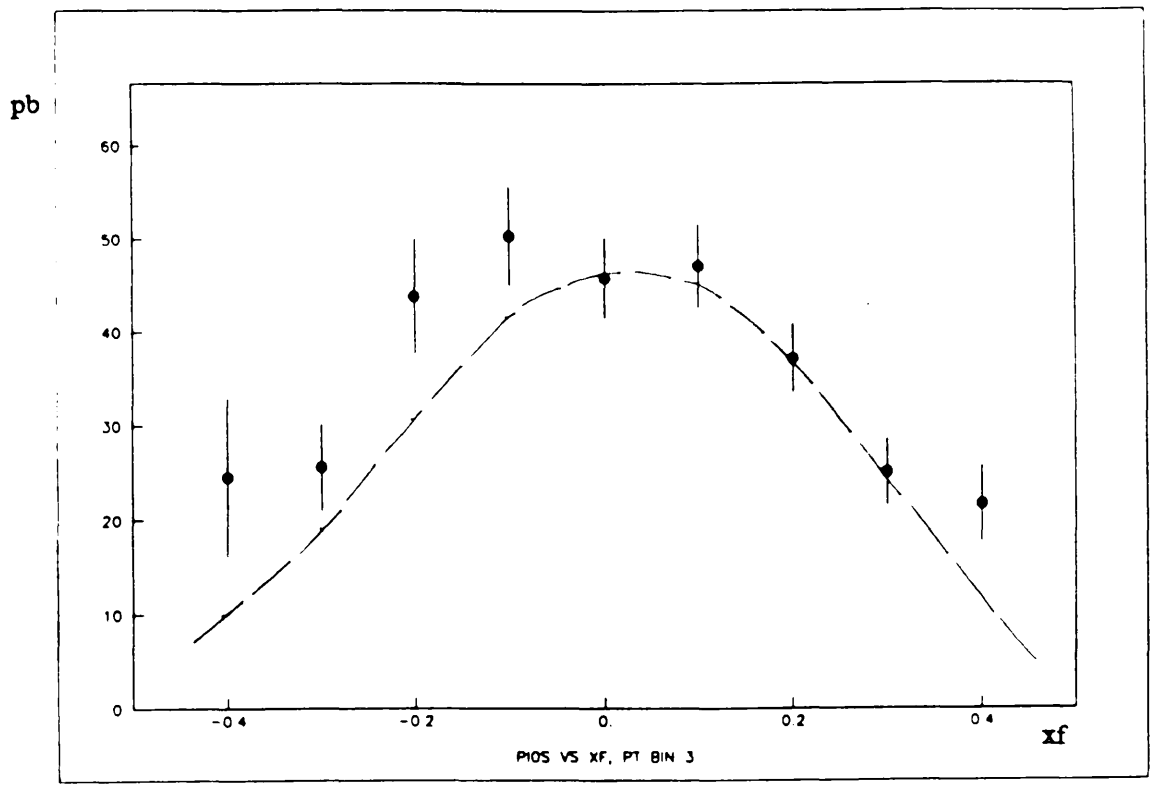

Figure 6.8c

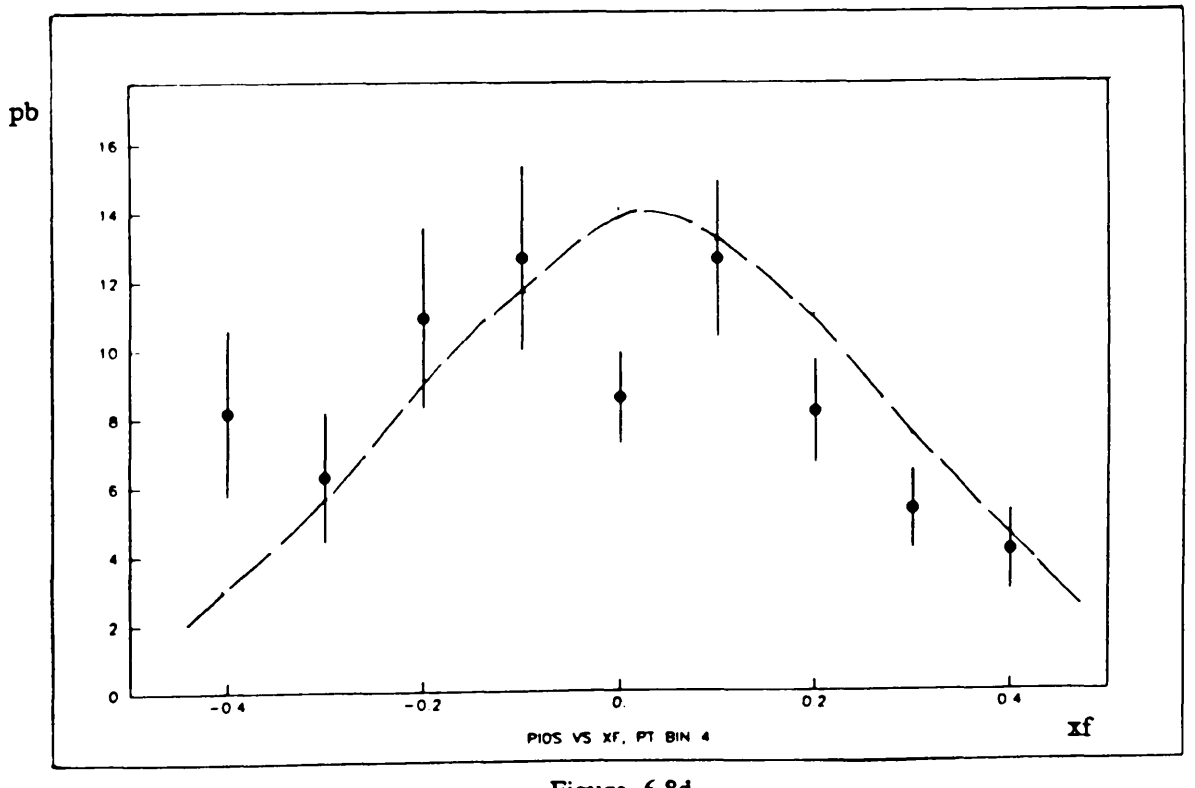

Figure 6.8d

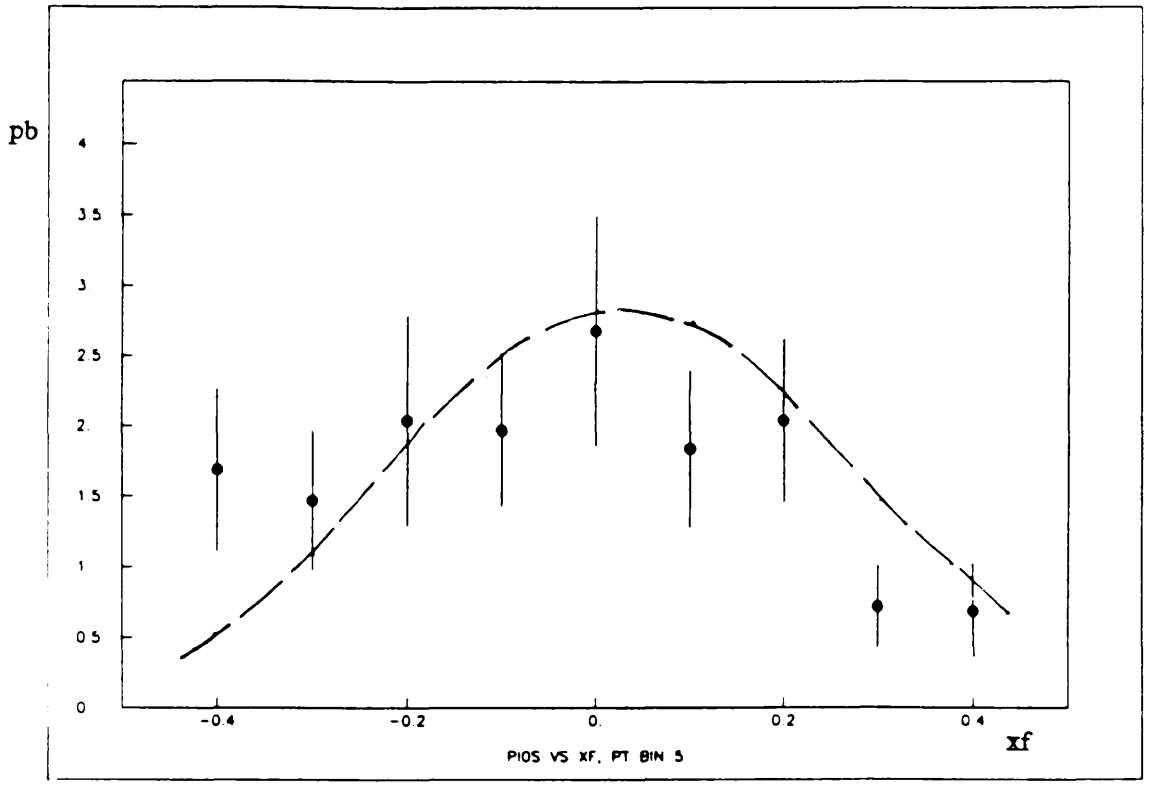

Figure 6.8e

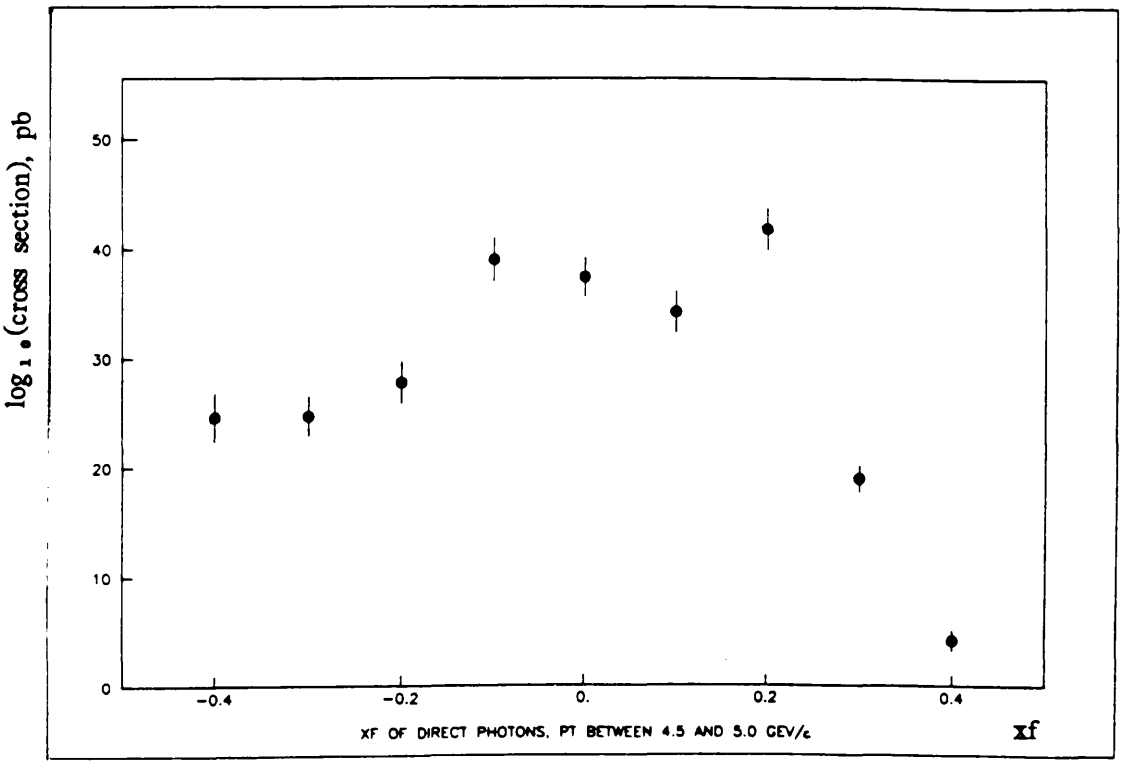

Figure 6.9a

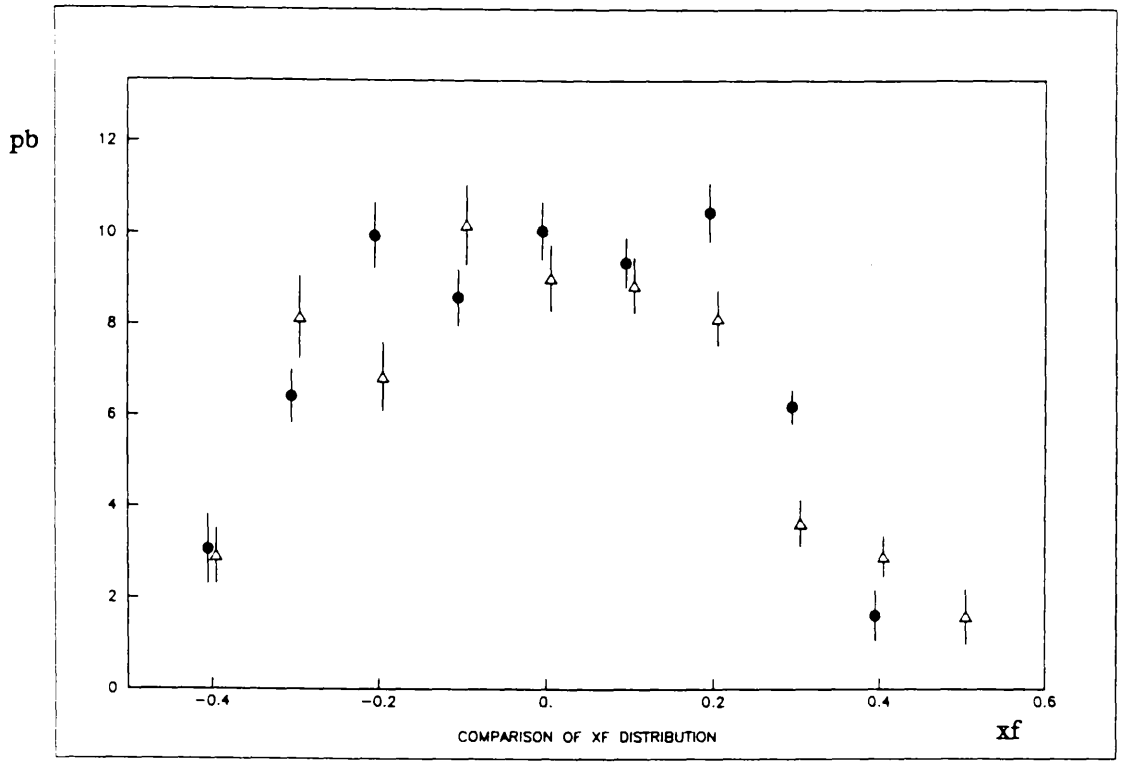

Figure 6.9b

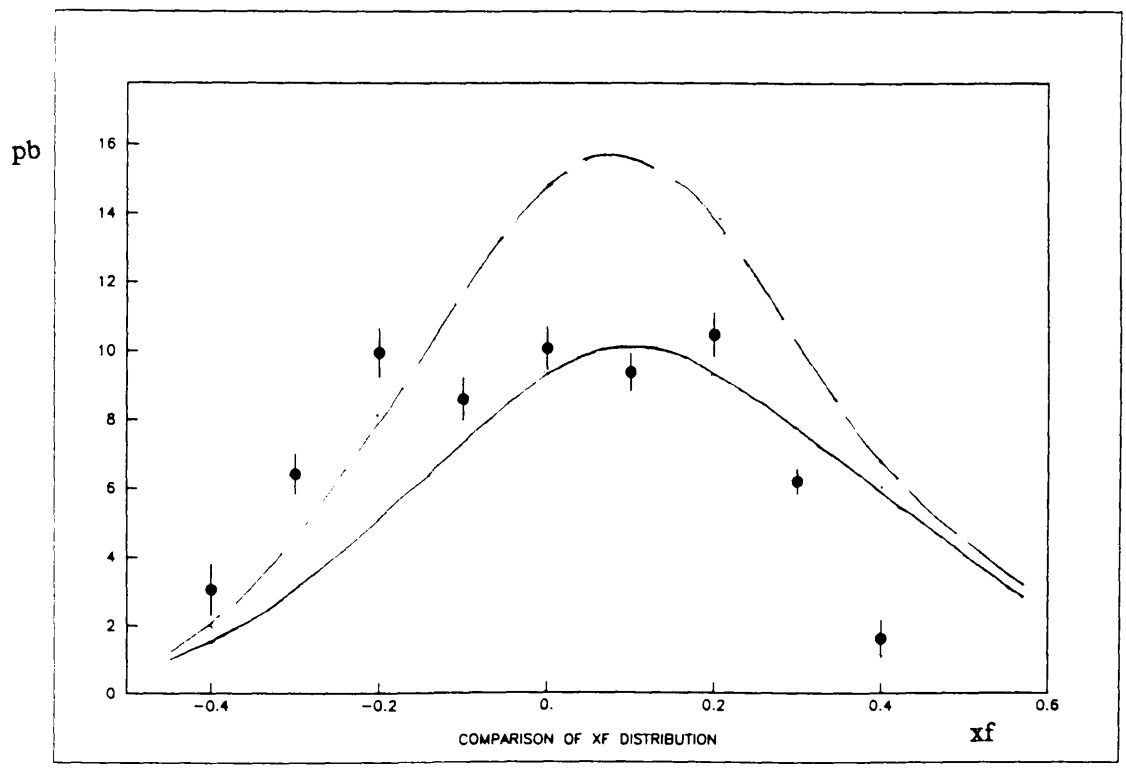

Figure 6.10

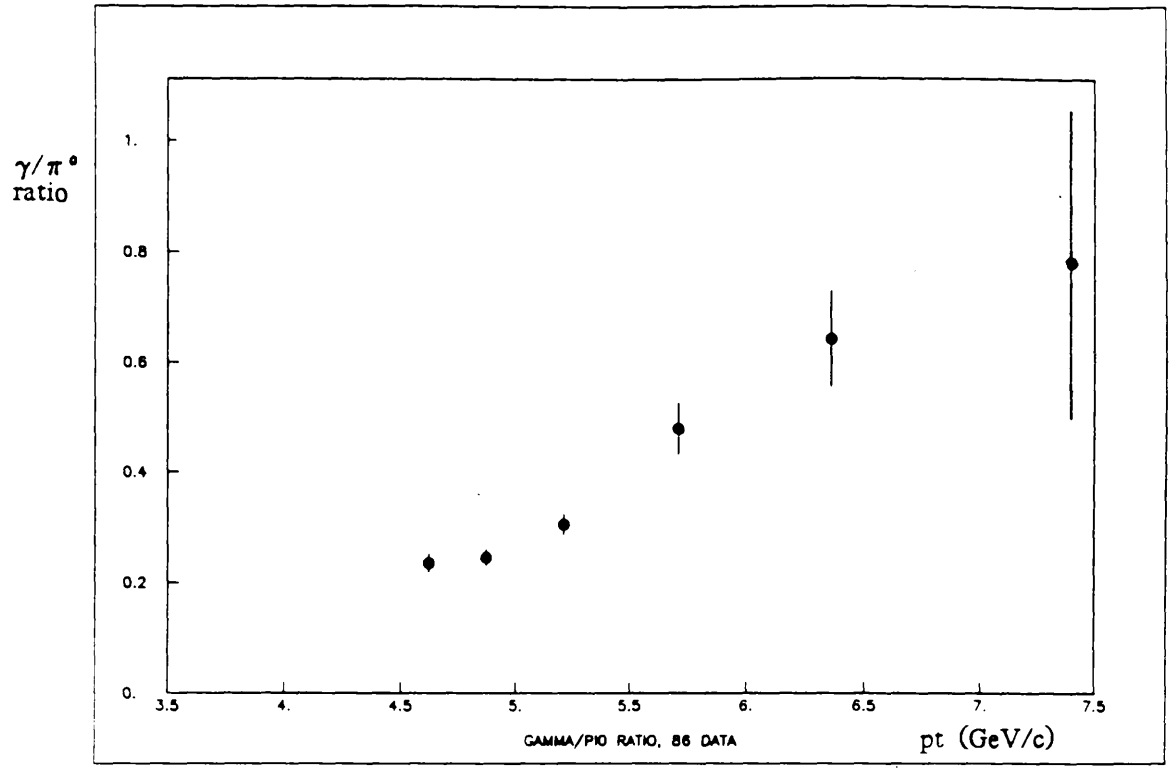

Figure 6.11a

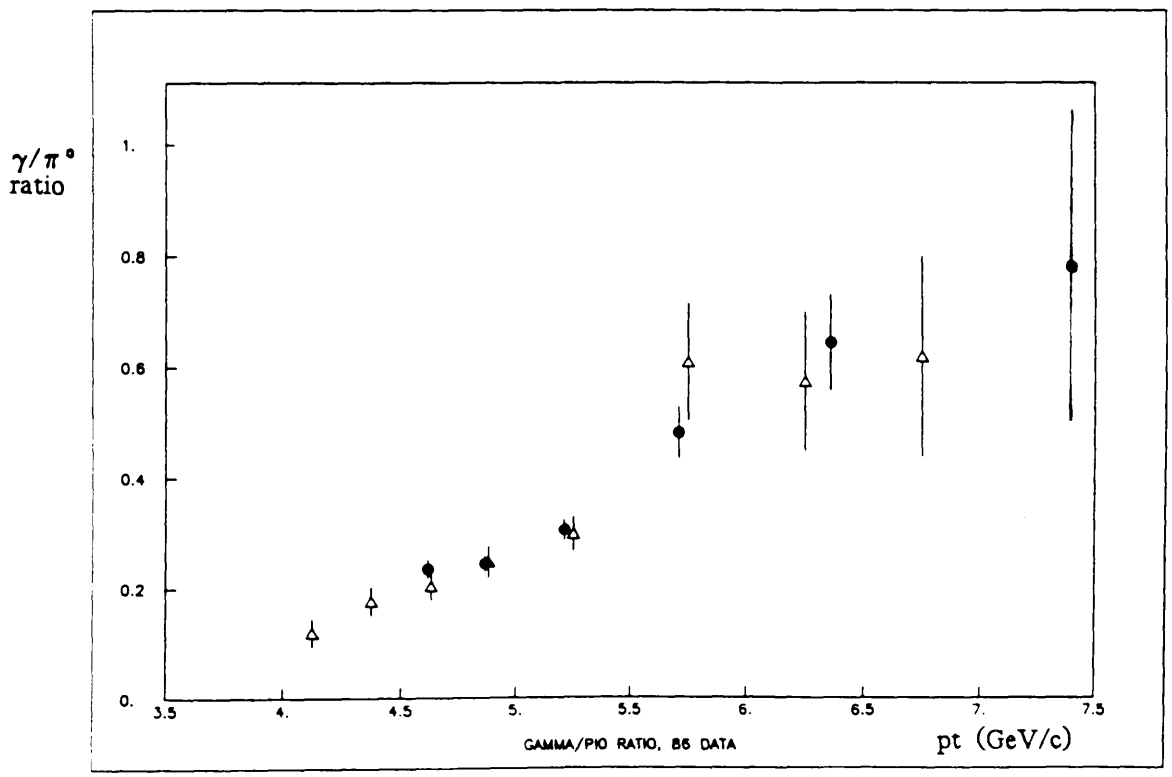

Figure 6.11b

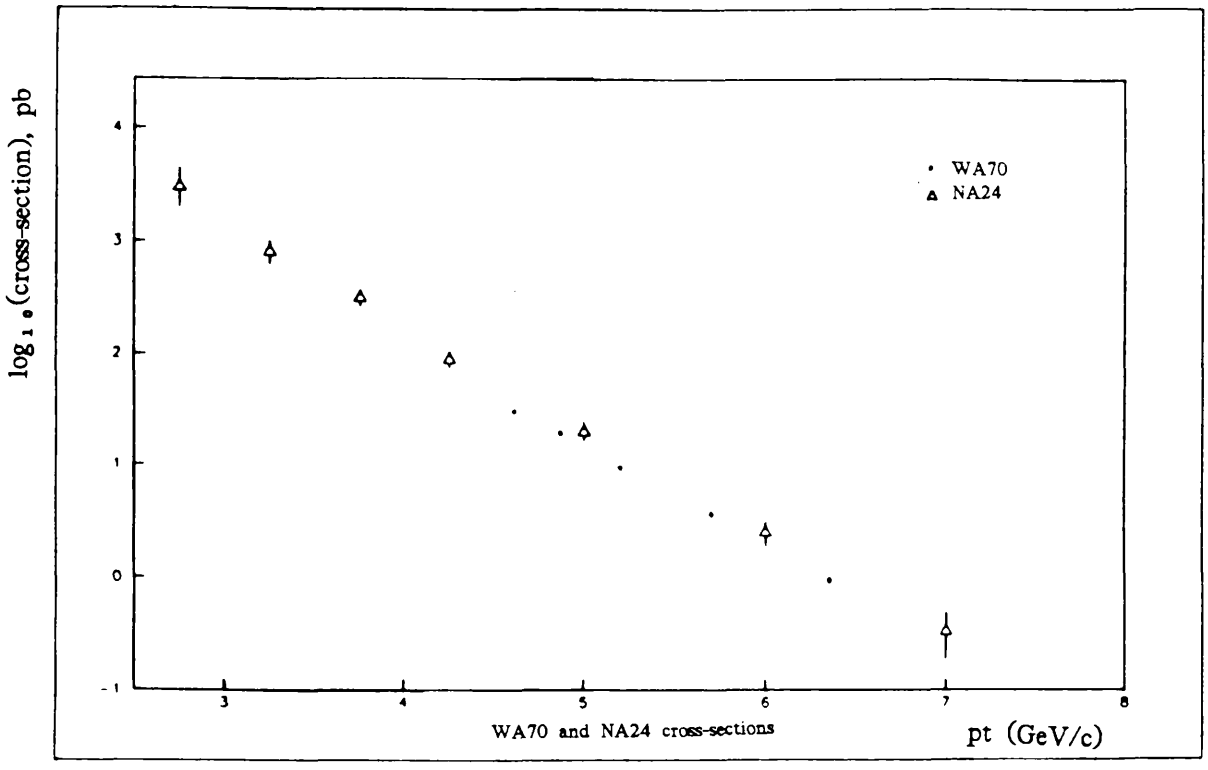
log 10 (cross-section), pb
WA70
NA24
WA70 and NA24 cross-sections
pt (GeV/c)

Figure 6.12

Table 6.1 Direct Photon Differential Cross-Sections.

xf	Pt (GeV/c) 4.5 – 4.75	4.75 – 5.0	5.0 – 5.5	5.5 – 6.0	6.0 – 7.0
-0.45	1541. 189. 111.	1084. 131. 78.	368. 73. 26.	25.0 15. 2.	40. 17. 3.
-0.35	1914. 181. 138.	1005. 123. 72.	634. 69. 46.	225. 34. 16.	111. 15. 8.
-0.25	1908. 203. 137.	1706. 152. 123.	981. 83. 71.	335. 44. 24.	130. 17. 9.
-0.15	3418. 225. 246.	2041. 162. 147.	912. 77. 66.	298. 37. 21.	149. 16. 11.
-0.05	3479. 221. 251.	1896. 146. 137.	1091. 70. 79.	355. 37. 26.	102. 13. 7.
+0.05	3161. 225. 228.	1624. 135. 117.	819. 62. 59.	499. 40. 36.	53. 11. 4.
+0.15	3170. 205. 228.	2264. 143. 163.	956. 65. 69.	429. 37. 31.	22. 6. 2.
+0.25	1421. 117. 102.	818. 83. 59.	525. 45. 38.	236. 27. 17.	20. 5. 1.
+0.35	215. 85. 16.	231. 52. 17.	121. 26. 9.	61. 16. 4.	35. 6. 2.
+0.45					

Format is: Cross-Section (pb)
±Statistical error
±Systematic error

Table 6.2 Direct Photon Invariant Cross-Sections.

xf	Pt (GeV/c) 4.5	4.75	5.0	5.5	6.0	7.0
-0.45						
	29.3 3.6 2.1	20.2 2.4 1.5	6.7 1.3 0.8	0.44 0.88 0.03	0.67 0.29 0.05	
-0.35						
	32.7 3.1 2.4	16.9 2.1 1.2	10.5 1.1 0.8	3.63 0.54 0.26	1.74 0.24 0.13	
-0.25						
	29.6 3.2 2.1	26.1 2.3 1.9	14.9 1.3 1.1	5.02 0.67 0.36	1.91 0.26 0.14	
-0.15						
	48.9 3.2 3.5	29.2 2.3 2.1	13.0 1.1 0.9	4.23 0.53 0.30	2.10 0.23 0.15	
-0.05						
	48.4 3.1 3.5	26.4 2.0 1.9	15.16 0.98 1.09	4.94 0.52 0.34	1.42 0.18 0.10	
+0.05						
	45.2 3.2 3.3	23.2 1.9 1.7	11.6 0.9 0.8	7.09 0.56 0.51	0.75 0.15 0.05	
+0.15						
	49.1 3.2 3.5	34.6 2.2 2.5	14.5 1.0 1.0	6.43 0.56 0.46	0.32 0.08 0.02	
+0.25						
	24.3 2.0 1.7	13.7 1.4 1.0	8.7 0.7 0.6	3.80 0.43 0.27	0.317 0.087 0.023	
+0.35						
	4.09 1.61 0.30	4.29 0.98 0.31	2.20 0.47 0.16	1.07 0.28 0.08	0.582 0.108 0.042	
+0.45						

Format is: Cross-Section (pb)
±Statistical error
±Systematic error

Table 6.3 Direct Photon Invariant Cross-Sections, Large xf Bins.

xf \ Pt (GeV/c)	4.5	4.75	5.0	5.5	6.0
-0.45	30.07 1.93 2.17	20.79 1.55 1.50	10.55 0.76 0.76	2.98 0.38 0.21	1.43 0.18 0.10
-0.15	47.43 2.05 3.41	26.32 1.42 1.90	13.26 0.72 0.95	5.42 0.43 0.39	1.41 0.16 0.10
+0.15	25.39 1.61 1.83	17.28 1.35 1.24	8.34 0.63 0.60	3.72 0.37 0.27	0.405 0.093 0.029
+0.45					

Format is: Cross-Section (pb)
±Statistical error
±Systematic error

Table 6.4 Ratio of '86 and '84/'85 Direct Photon Cross-Sections.

xf \ Pt (GeV/c)	4.5	4.75	5.0	5.5	6.0
-0.45	1.41	1.44	1.94	0.87	1.66
-0.15	1.03	0.99	1.02	0.79	0.69
+0.15	0.88	0.72	0.84	0.94	0.33
+0.45					

Ratio is ('86 cross-section)/('84/'85 cross-section)

Table 6.5 π^0 Differential Cross-Sections.

xf	Pt (GeV/c) 4.5 – 4.75	4.75 – 5.0	5.0 – 5.5	5.5 – 6.0	6.0 – 7.0
-0.45	2199. 1276. 158.	1696. 577. 122.	1321. 455. 95.	458. 136. 33.	98. 34. 7.
-0.35	4199. 1129. 302.	2760. 565. 199.	1544. 276. 111.	387. 116. 28.	92. 32. 7.
-0.25	9435. 1619. 679.	6289. 791. 453.	2884. 406. 208.	727. 175. 52.	138. 51. 10.
-0.15	10528. 1437. 758.	7866. 788. 566.	3546. 371. 255.	890. 190. 64.	139. 38. 10.
-0.05	13992. 1870. 1007.	9772. 876. 704.	3295. 307. 237.	617. 96. 44.	193. 59. 14.
+0.05	18595. 2418. 1338.	9276. 861. 768.	3318. 318. 239.	889. 160. 64.	130. 39. 9.
+0.15	14270. 2253. 1027.	7454. 791. 537.	2449. 243. 176.	543. 101. 39.	138. 39. 10.
+0.25	5217. 785. 375.	3549. 436. 256.	1509. 214. 109.	327. 70. 24.	45. 18. 3.
+0.35	4597. 1024. 331.	2585. 447. 186.	1171. 214. 84.	230. 66. 17.	40. 19. 3.
+0.45					

Format is: Cross-Section (pb)
±Statistical error
±Systematic error

Table 6.6 π^0 Invariant Cross-Sections.

xf	Pt (GeV/c) 4.5	4.75	5.0	5.5	6.0	7.0
-0.45	41.8 ±24.2 3.0	31.6 10.7 2.3	23.9 8.2 1.7	8.0 2.4 0.6	1.66 0.57 0.12	
-0.35	71.8 19.3 5.2	46.4 9.5 3.3	25.5 4.6 1.8	6.24 1.87 0.45	1.46 0.50 0.11	
-0.25	146.3 25.1 10.5	96.2 12.1 6.9	43.8 6.2 3.2	10.9 2.6 0.8	2.04 0.75 0.15	
-0.15	150.6 20.6 10.8	112.5 11.3 8.1	50.4 5.3 3.6	12.7 2.7 0.91	1.98 0.54 0.14	
-0.05	194.5 26.0 14.0	135.8 12.2 9.8	45.8 4.26 3.3	8.58 1.33 0.62	2.68 0.82 0.19	
+0.05	265.9 34.6 19.1	132.7 12.3 9.6	47.1 4.5 3.4	12.6 2.3 0.91	1.84 0.56 0.13	
+0.15	221.2 34.9 15.9	114.0 12.1 8.2	37.2 3.7 2.7	8.16 1.51 0.59	2.04 0.58 0.15	
+0.25	89.2 13.4 6.4	59.6 7.3 4.3	24.9 3.5 1.8	5.27 1.13 0.38	0.71 0.29 0.05	
+0.35	87.4 19.5 6.30	48.1 8.3 3.5	21.2 3.9 1.5	4.02 1.15 0.29	0.68 0.31 0.05	
+0.45						

Format is: Cross-Section (pb)
±Statistical error
±Systematic error

Table 6.7 π^0 Invariant Cross-Sections, Large xf Bins.

xf \ Pt (GeV/c)	4.0 – 4.25	4.25 – 4.5	4.5 – 4.75	4.75 – 5.0	5.0 – 5.5	5.5 – 6.0	6.0 – 7.0
-0.45 to -0.15	385.4 22.4 27.7	213.4 17.7 15.4	86.6 6.6 6.3	58.1 4.1 4.2	31.1 2.6 2.2	8.38 1.05 0.60	1.72 0.28 0.12
-0.15 to +0.15	606.3 20.0 43.7	368.3 16.9 26.5	203.7 8.3 14.7	127.0 4.8 9.1	47.8 2.3 3.4	11.3 1.0 0.8	2.17 0.28 0.16
+0.15 to +0.45	297.8 12.5 21.4	190.9 10.5 13.7	132.6 7.0 9.5	73.9 4.4 5.3	27.8 1.7 2.0	5.82 0.60 0.42	1.14 0.17 0.08

Format is: Cross-Section (pb)
±Statistical error
±Systematic error

Table 6.8 Ratio of '86 and '84/'85 π^0 Cross-sections.

xf \ Pt (GeV/c)	4.5 – 4.75	4.75 – 5.0	5.0 – 5.5	5.5 – 6.0	6.0 – 7.0
-0.45 to -0.15	0.866	1.193	1.467	1.330	1.132
-0.15 to +0.15	0.828	0.948	1.060	0.808	1.46
+0.15 to +0.45	0.872	0.911	0.861	0.582	0.494

Ratio is ('86 cross-section)/('84/'85 cross-section)

Table 6.9 Parametrisation of Direct Photon Cross-Sections.

		m	n	x_0
'86, $\pi^- p \to \gamma X$		3.71 ∓ 0.02	3.61 ∓ 0.02	-0.0305 ∓ 0.0045
Correlation Matrix	C	0.030	-0.003	-0.056
	x	0.039	-0.049	
	n	0.013		

		m	n	x_0
'84/'85, $\pi^- p \to \gamma X$		3.34 ∓ 0.19	3.28 ∓ 0.11	0.0565 ∓ 0.007
Correlation Matrix	C	0.520	0.952	0.116
	x	0.188	0.150	
	n	0.754		

Table 6.10 Parametrisation of π^0 Cross-Sections.

'86, $\pi^- p \to \pi^0 X$

m	n	x_0
4.77 ∓ 0.10	4.51 ∓ 0.05	-0.027 ∓ 0.001

Correlation Matrix

C	0.186	0.936	0.104
x	0.119	0.064	
n	-0.169		

'84/'85, $\pi^- p \to \pi^0 X$

m	n	x_0
3.82 ∓ 0.07	4.84 ∓ 0.11	0.063 ∓ 0.002

Correlation Matrix

C	-0.311	0.960	-0.088
x	0.119	-0.110	
n	-0.561		

CHAPTER 7

The Production of Pairs of Direct Photons.

A search for double direct photons was made in the '86 data both in Glasgow and by M. Donnat in Geneva. The intention was to keep the two analyses as independent as possible, using the Glasgow analysis as a check. The principle problem was that the Monte Carlo sample of double high pt events used to calculate the background to the double direct photon signal was generated on the University of Geneva IBM 3090 (sect 3.5), and the background calculation used the numbers of double high pt events produced at Geneva using the *Geneva* analysis programs. This will be discussed as a source of bias and error below.

M. Donnat found 138 $\mp$ 22 double direct photon events in the full 1986 data sample, and measured the detection efficiency of his analysis programs at 34% for photons with pt > 2.75 GeV/c. The cross-section integrated over xf and $\Delta\phi$ ($\Delta\phi = \phi_1 - \phi_2$, ϕ_1 and ϕ_2 being the azimuthal angles of the two photons), and integrated from pt > 3.0 GeV/c was found to be

(69 $\mp$ 11.5) pb,

compatible with the beyond leading log calculation for the process $q\bar{q} \rightarrow \gamma\gamma$ of 57.8 pb.

7.1 The Cuts for Double High Pt Events.

To determine the direct photon signal with any assurance we must detect not only high pt double direct photon events but also high pt $\pi^0\pi^0$, $\gamma\pi^0$ and $\pi^0\gamma$

events. In the last two we differentiate between the highest pt particle being a π^0 or a γ. These event types dominate the $\gamma\gamma$ background.

(Throughout this chapter a double direct photon event with photons of say 4.5 and 3.5 GeV/c will be classed as a 4.5 GeV/c event. The higher pt 'trigger' particle will be denoted as having pt_1, while the 'away side' particle will have pt_2.)

As the WA70 experiment intended to measure the double direct photon cross-section above pt = 3 GeV/c, the background events referred to above must also be recorded. As these contain π^0s, we must set the trigger 4 pt threshold (see 2.11) lower than this to detect the decay photons from 3 GeV/c π^0s. Events were therefore required to have showers with transverse momenta greater than 1.8 GeV/c in opposite quadrants, 1 and 3 or 2 and 4, for trigger 4 to 'fire'. The event must also have passed the standard vertex and TOF cuts and the trigger shower in both quadrants must be non-hadronic as indicated by having less than 20% of its energy deposited in the third segment of the calorimeter and being at least 3cm from any points in the MWPC.

Having isolated events with two high pt photon candidates in opposite quadrants we must subject them to further cuts to identify $\pi^0\pi^0$, $\gamma\pi^0$, $\pi^0\gamma$ or $\gamma\gamma$ events. The cuts for each are listed below.

1) $\gamma\gamma$ events.

a) The trigger photon must have $pt_1 > 3$ GeV/c.

b) The away side photon must have $pt_2 > 2.75$ GeV/c.

c) The width of both showers in segment 1 must correspond to a single electromagnetic shower (i.e. < 2 cm).

d) neither shower must have an effective mass in the π^0 range 85 to 185 MeV/c^2 when combined with another photon in a pairing with asymmetry < 0.95.

e) neither shower must have an effective mass in the η range 450 to 650 MeV/c^2 when combined with another photon with E > 2 GeV/c in a pairing with asymmetry < 0.8.

f) Both showers had to lie within a fiducial region D + 2 cm from the quadrant edges where D is defined as in section 4.5.

2) $\pi^0\pi^0$ events.

a) The trigger π^0 must have pt_1 > 3 GeV/c.

b) The away side π^0 must have pt_2 > 2.75 GeV/c.

c) both showers must have an effective mass in the range 135 ∓ 50 MeV/c^2 when combined with a shower in their respective quadrants in a pairing with asymmetry < 0.9.

3) $\gamma\pi^0$ and $\pi^0\gamma$ events.

The cuts for γ's and π^0s described above were applied as appropriate for these events. In each case the trigger shower was required to have pt_1 > 3.0 GeV/c and the away side trigger pt_2 > 2.75 GeV/c.

It will be noted that if a trigger shower with pt_1 > 3.0 GeV/c passes the cuts for a direct photon, and the away side shower with pt_2 > 2.75 GeV/c passes the cuts for a photon shower but forms a π^0 in a pairing with asymmetry between 0.90 and 0.95 it will be accepted neither as a $\gamma\pi^0$ event or a $\gamma\gamma$ event, despite clearly being a double high pt event of some description. The author felt that such events should be classed as $\gamma\pi^0$ events but to make the Glasgow results as compatible as possible with the Geneva double direct photon study, such events were rejected. Only a very small number of events (four) fell into this category.

7.2 Calculating the Background Underneath the π^0 Peaks.

A fitting program was used to calculate the background under the π^0 peaks in the $\pi^0\pi^0$, $\gamma\pi^0$ amd $\pi^0\gamma$ events. This program used a function (consisting of linear, Breit-Wigner and Gaussian terms) developed by R. Lucock [52] to describe the π^0 signal + background shape in the '84 data. The background under the trigger side π^0 was found to be of 5% $\mp$ 1%, while that under the away side π^0 peak was found to be negligible (< 1%). The correction factors for $\pi^0\pi^0$, $\gamma\pi^0$ and $\pi^0\gamma$ events were taken as 0.944, 0.99 and 0.95 respectively.

7.3 Event Totals.

The numbers of $\gamma\gamma$, $\gamma\pi^0$, $\pi^0\gamma$ and $\pi^0\pi^0$ events found, and the number of events adjusted for background, is shown below.

event class	raw number	after background subtraction
$\gamma\gamma$	344	-
$\gamma\pi^0$	409	389
$\pi^0\gamma$	405	401
$\pi^0\pi^0$	2376	2242

Extrapolating the direct photon numbers down to pt = 3 GeV/c, the number of single direct photons with pt greater than this produced during the 1986 run was approximately 125,000 after efficiency calculations. As the double direct photon signal is expected from theory [15] to be down by a factor of ~200, and as we shall see the double direct photon detection efficiency is ~22% we expect to see 100-200 double direct photon events. The observed total of 344 events suggests that the signal to background ratio is ~1.

Before we investigate this background further we introduce the idea of double counting. Rather than simply deal with event numbers, which take no account of pt_1/pt_2 distributions with pt, we shall count each double high pt product seperately (a logical approach as the two direct photons in a double event are theoretically indistinguishable). Double counting was employed throughout the background calculation.

The pt distributions of the trigger particles in the observed $\gamma\gamma$, $\gamma\pi^0$, $\pi^0\gamma$ and $\pi^0\pi^0$ events are shown in figs. 7.1a - d.

A software problem caused the $\pi^0\gamma$ signal in the 3.0→3.5 GeV/c bin to be underenumerated (fig. 7.1b). A value for this bin (330 events) was extrapolated from the upper bins.

7.4 Calculating the Background to the Double Direct Photon Signal.

This method uses the Monte Carlo events generated at Geneva. It is similar in outline to the single direct photon background calculation. Firstly, we separate the purely hadronic and direct photon parts of the Monte Carlo, which we denote as MC1 and MC2. MC1 contains all parton-parton subprocesses which lead to high pt π^0s, ηs, ωs etc., while MC2 contains the single direct photon producing subprocesses $q\bar{q}\rightarrow\gamma g$, $qg\rightarrow\gamma q$, $qq\rightarrow qq(q\rightarrow\gamma q)$ etc. The numbers of $\pi^0\pi^0$, $\gamma\pi^0$, $\pi^0\gamma$ and $\gamma\gamma$ events produced in MC1 and MC2 (as determined by the Geneva analysis programs) are illustrated in figs. 7.2a and b. Any double direct photon events observed are necessarily false as the double direct photon subprocess are not present in either the MC1 or MC2 programs. The two sets of numbers were then multiplied by factors A and B to bring them into as close agreement with their proportions in the data as possible. In other words, we minimise the following χ^2:

$$\chi^2 = \sum_{i=1}^{6} \sum_{j=1}^{3} \frac{(\text{data} - A.MC1 - B.MC2)^2_{ij}}{\sigma^2_{ij}}$$

where the index i runs over all pt bins and the index j runs over the three classes of events $\pi^0\pi^0$, $\gamma\pi^0$ and $\pi^0\gamma$. The errors take the data and Monte Carlo statistical errors into account.

The best fit is given by A = 2.790 and B = 0.068 with a χ^2 of 1.56 per d.o.f.

The background is then assumed to be entirely described by the two Monte Carlos. The double direct photon components of MC1 and MC2 were multiplied (after the MC1 figures were smoothed as shown in fig. 7.3a) by A and B respectively to give the background. This calculation is shown below (double counting employed);

pt	A	MC1		B	MC2		result	(smoothed)
3-3.5 GeV/c	2.790	29	+	00.068	768	=	134	(134)
3.5-4 GeV/c		14			418		48	(68)
4-4.5 GeV/c		7			202		33	(33)
4.5-5 GeV/c		3			117		25	(17)
5-5.5 GeV/c		1			55		4	(7)
5.5-6 GeV/c		0.5			21		1	(2)

The final background figures are themselves smoothed (figures shown in brackets at right, above and in fig. 7.3b), and subtracted from the observed signal (shown below). Below, the numbers obtained using double counting are converted back into event numbers. As the away side photon need only have a pt of 2.75, this was not simply a case of halving the total, and the proportions of trigger and away side photons seen in the data have been used to perform the conversion.

pt	signal-background	result	(whole events)
3-3.5 GeV/c	274 - 134 =	140 ∓ 15	(64 events)
3.5-4 GeV/c	129 - 68 =	62 ∓ 10	(47 events)
4-4.5 GeV/c	70 - 33 =	37 ∓ 9	(30 events)
4.5-5 GeV/c	39 - 17 =	22 ∓ 8	(19 events)
5-5.5 GeV/c	22 - 8 =	14 ∓ 5	(12 events)
5.5-6 GeV/c	10 - 2 =	8 ∓ 4	(8 events)

There were 283 photons seen after background subtraction, which is the equivalent of 179 whole events (due to rounding errors the event totals in each bin add up to 180). The total of 179 events is in the predicted range. Subtracting the background from the raw signal we obtain

$$344 \mp 19 - 165 \mp 13 = 179 \mp 25 \text{ events}$$

i.e. a 7σ signal.

7.5 Systematic errors in the Background Calculation.

The above method made use of event totals in MC data which had been reached using the Geneva analysis programs, rather than their Glasgow equivalents. We can reduce this dependence by altering the MC1 and MC2 event totals using the Glasgow and Geneva event totals as seen in the data. Altering the event totals found in the Monte Carlo generated-data and observing the effect the change has on the factors A and B will at least allow us to estimate the systematic error.

The changes are made as follows. Let the number of events of type i seen by the Geneva analysis be Ni_{Gen} and the number seen by the Glasgow analysis be Ni_{Gla}. The events of type i in the Monte Carlo are then multiplied by Ni_{Gla} / Ni_{Gen} and the χ^2 minimization performed above is repeated. Ni_{Gen}, Ni_{Gla} (not double counted) and the old and new MC1 and MC2 for the first 3-3.5 GeV/c bin

are shown below. The trigger and away side π° background figures of 5% and 1% were replaced by the Geneva figures of 12% and 12% for consistency and the Monte Carlo figures were not smoothed.

event type	Ni_{gen}	Ni_{Gla}	Old MC1	New MC1	Old MC2	New MC2
$\pi^\circ\pi^\circ$	1997	1840	654	603	76	70
$\pi^\circ\gamma$	614	4770	147	114	1309	1017
$\gamma\pi^\circ$	547	355	104	68	2742	1780

These modifications resulted in a fit of A=3.123 and B=0.105. The background calculations presented above were performed again with the new figures;

pt	A	MC1	B	MC2	result
3-3.5 GeV/c	3.123	29	+ 0.105	768	= 171
3.5-4 GeV/c		7		418	66
4-4.5 GeV/c		7		202	43
4.5-5 GeV/c		4		117	25
5-5.5 GeV/c		0		55	6
5.5-6 GeV/c		0		21	2

and

pt	signal-background	(events)
3-3.5 GeV/c	274 - 171 = 103 ∓ 15	(47)
3.5-4 GeV/c	129 - 66 = 63 ∓ 10	(47)
4-4.5 GeV/c	70 - 43 = 27 ∓ 9	(22)
4.5-5 GeV/c	39 - 25 = 14 ∓ 8	(12)
5-5.5 GeV/c	22 - 6 = 16 ∓ 5	(14)
5.5-6 GeV/c	10 - 2 = 8 ∓ 4	(8)

i.e. a total of 150 ∓ 22 events. By this last correction we have made our analysis more independent of Geneva's, though at the expense of slightly increasing our statistical error.

Before we can compare this result with that arrived at by the Geneva group, we must calculate the cross section using the detection efficiency.

7.6 The Double Direct Photon Acceptance.

The double direct photon acceptance was calculated using a tape of 8984 MC double direct photon events, generated by the TWISTER Monte Carlo on the Geneva 3090 IBM as described above. The standard Glasgow double direct photon analysis program was run on the MC events (using the same cuts as for the analysis of the data), and 1957 were found. This is equivalent to an acceptance of 21.8 ∓ 0.5%.

A detailed study of the geometrical acceptance at Geneva gave losses and their magnitudes as follows;

γ conversion	13%
γ outside calorimeter	27%
$\gamma\gamma$ not in opposite quadrants	5%
Accidental triggers rejection	3%
Misidentification of γ	1%
Fiducial cuts	17%

The first five of these are applicable to the Glasgow analysis but the last will differ slightly as the Geneva analysis required a photon-like shower to be 5cm from the nearest quadrant edge while at Glasgow the requirement was D+2 cm (see section 4.3 above). The stricter cut at Glasgow will increase the loss to 19% ∓ 1%. The cumulative acceptance taking all these losses into account is therefore

35-36%. At first sight this is in disagreement with the Glasgow acceptance of 21.8 ∓ 0.5, but this list does not include losses due to the pt requirement on the away side photon which causes some genuine double direct photon events to be rejected. This is discussed below.

7.7 The 'z' Variable.

A genuine double direct photon event in which the trigger photon has a pt above 3 GeV/c but the opposite photon has a pt less than 2.75 GeV/c will be rejected by the cuts used in the analysis. To investigate this problem further we will introduce the variable z, defined as;

$$z = -pt_1.pt_2/pt_1^2 = -(pt_2/pt_1)\cos\Delta\phi$$

where $\Delta\phi=\phi_1-\phi_2$. The z distribution for all 344 double direct photon events found the '86 data is shown in fig. 7.4. Sixty per cent of events lie in the region below $z < 0.85$. Assuming that the low z events are not entirely false (Monte Carlo double direct photon events show a similar z disribution) we deduce that ~60% of $\gamma\gamma$ events with pt_1 between 3.0 and 3.5 GeV/c will be rejected (assuming $\Delta\phi$ to be 180°). The corresponding figure for the next pt bin, 3.5→4.0, is 35%. This effect is clearly largest in these two lowest pt bins, which contain the great majority of events. The overall loss is consequently large, amounting to 37% over the whole pt range.

The Geneva acceptance corrected for this effect is 22.4 ∓ 1.0, closely compatible with the Glasgow figure of 21.8 ∓ 0.5.

7.8 Cross-Sections.

When calculating the cross-sections, double counting is employed as the two photons are theoretically indistinguishable as mentioned above. The equations used

to calculate the cross-section are essentially the same as those given in section 6.1 above. The cross-section ($d\sigma/dpt$) vs. pt is shown in fig. 7.5, together with the Beyond-Leading-Log (BLL) prediction (solid line) and the Born term prediction (broken line) [61].

The double direct photon cross-section above pt=3.0 GeV/c, integrated over xf and ϕ, was measured to be 73.4 $\mp$ 10.4 (statistical) $\mp$ 7.4 (systematic) pb. The systematic error due to the absolute energy scale and systematic errors in the Monte Carlo, as discussed above in section 5.9, was estimated to be 10%.

The first order QCD calculation (using Duke-Owens set 1 structure functions and Λ_{QCD} = 200 MeV) predicts a $q\bar{q}\rightarrow\gamma\gamma$ cross-section of 39.4 pbarn. The inclusion of BLL terms raises this to 57.8 pbarn, consistent with the cross-section obtained above.

The integrated cross-section as measured by the Geneva group was 69 $\mp$ 11.5 pb. In conclusion, therefore, the double direct photon analyses at Glasgow and Geneva are compatible. These results have been published [62].

7.9 The Calculation of R and a_s.

The ratio R, given by (section 1.5.1)

$$R = \frac{\sigma(\pi^- p\rightarrow\gamma X)-\sigma(\pi^+ p\rightarrow\gamma X)}{\sigma(\pi^- p\rightarrow\gamma\gamma)-\sigma(\pi^+ p\rightarrow\gamma\gamma)}$$

was calculated using the single and double direct photon cross-sections. The term $\sigma(\pi^+ p\rightarrow\gamma X)$ was available from the analysis of the '84 and '85 runs, whilst the term $\sigma(\pi^+ p\rightarrow\gamma\gamma)$ was estimated using a Monte Carlo. It was found to be $\sim$ 10% of the $\pi^- p\rightarrow\gamma\gamma$. Recalling that (neglecting $d\bar{d}$ annihilation)

$$a_s(LO) = (1/3)aR, \qquad 7.1$$

where (LO) indicates leading order approximation and a is the electromagnetic coupling strength, a calculation of a_s can now be made. This will only be useful if the Q^2 value at which the measurement is made is known.

The Q^2 range is dependent on the choice of scaling. In the table below, the value of a_s arrived at using the experimental value R is shown for the three pt bins 4.0→4.5, 4.5→5.0 and 5.0→6.0, using three different scaling approaches.

Firstly (column (i)) the leading order approximation $a_s(LO)$ is obtained by inserting the value of R into the the equation 7.1 above. Secondly, the cross-sections are expressed as corrections to the first-order Born term σ_0, and R can be rewritten as

$$R = \frac{K_1\sigma_0^{\gamma}}{K_2\sigma_0^{\gamma\gamma}} = \frac{\int F_q(M_1^2)F_{\bar{q}}(M_1^2)\, d\sigma_0^{\gamma}(Q_1^2)(1+a_s C^{\gamma})}{\int F_q(M_2^2)F_{\bar{q}}(M_2^2)\, d\sigma_0^{\gamma\gamma}(1+a_s C^{\gamma\gamma})}$$

where M_1^2 and M_2^2 are the factorisation scales of the structure functions F and Q_1^2 is the renormalisation scale. Conventional $M_1^2 = M_2^2 = Q_1^2 = pt^2$ scaling produces large higher order corrections, both K_1 and K_2 being ~1.6. The values of a_s resulting from this are shown as column (ii) in the table. An argument against this choice of scaling is that the σ_0^{γ} Born term multiplied by the K_1 factor of ~1.6 does not reproduce the measured single direct photon cross-section distribution. Furthermore, correcting the $a_s(LO)$ values of column (i) by using the K-factors does not bring them into agreement with those reached using $Q^2=pt^2$ scaling.

Pt range (GeV/c)	R expt	(i)a_s(LO)	(ii)$a_s(Q^2=pt^2)$	(iii)a_s(opt)
4.0→4.5	180∓46	0.44∓0.11	0.193	0.46 ∓ 0.14
4.5→5.0	159∓50	0.39∓0.12	0.187	0.39 ∓ 0.11
5.0→6.0	102∓32	0.25∓0.0	0.180	0.31 ∓ 0.09

In column (iii) the scales have been chosen using the principle of 'minimum sensitivity' described in section 1.10. This principle leads to the adoption of 'optimised' scales which place the WA70 experiment in the approximate Q^2 range 0.5 → 1.2, lower than by setting $Q^2=pt^2$. The resulting K-factors are also lower, K_1 being ~0.9 and K_2 ~1.2. This successfully reproduces the single direct photon cross-section. QCD cross-sections calculated using BLL terms are typically within 30% of those calculated using first order approximations only, so a correct choice of scaling should produce values for a_s within 30% or so of the a_s(LO) values of column (i). This is indeed the case.

In fig. 7.6 [63], the a_s(LO) values of column (i) are shown (filled circles) placed at the Q^2 values suggested for them using optimised scales, and at the Q^2 values suggested by conventional $Q^2=pt^2$ scaling (open circles). The most recent theoretical predictions of a_s [62] made assuming Λ_{QCD} to be 100, 200 and 500 MeV are also shown. Adopting $Q^2= pt^2$ scaling situates the points in a region consistent with a Λ_{QCD} value above 500 MeV, in conflict with recent measurements of this parameter such as the value of 230 $\mp$15 $\mp$50 MeV [58] discussed in chapter 6. With optimised scaling however, the a_s measurements lie in a region consistent with this value.

Chapter Seven Figures.

Figure 7.1a Pt distribution of trigger γs in 344 observed $\gamma\gamma$ events.

Figure 7.1b Pt distribution of trigger γs in 409 observed $\gamma\pi^0$ events.

Figure 7.1c Pt distribution of trigger π^0s in 405 observed $\pi^0\gamma$ events.

Figure 7.1d Pt distribution of trigger π^0s in 2376 observed $\pi^0\pi^0$ events.

Figure 7.2a Numbers of $\gamma\gamma$, $\gamma\pi^0$, $\pi^0\gamma$ and $\pi^0\pi^0$ events present in MC1, versus pt.

Figure 7.2b Numbers of $\gamma\gamma$, $\gamma\pi^0$, $\pi^0\gamma$ and $\pi^0\pi^0$ events present in MC2, versus pt.

Figure 7.3a Smoothed and unsmoothed pt distribution of $\gamma\gamma$ events in MC1.

Figure 7.3b Smoothed and unsmoothed pt distribution of final background to $\gamma\gamma$ signal.

Figure 7.4 Distribution of z in the '86 data, where

$z = -pt_1.pt_2/pt_1^2 = -(pt_2/pt_1)\cos\Delta\phi$.

Figure 7.5 Double direct photon cross-section ($d\sigma/dpt$) vs. pt ('86 data) together with the Beyond-Leading-Log prediction for this cross-section.

Figure 7.6 The coupling strength of the strong force, a_s as measured by WA70, versus Q^2. Q^2 co-ordinates arrived at using optimised scales (filled circles), and using conventional $Q^2=pt^2$ scaling (open circles).

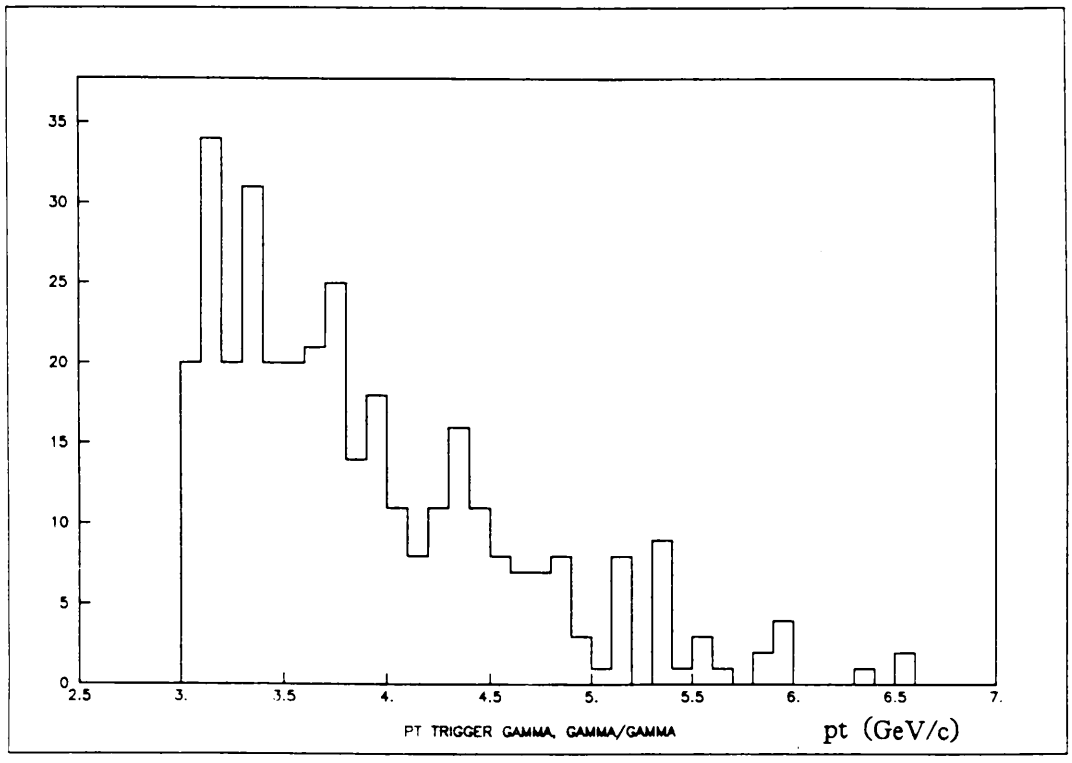

Figure 7.1a

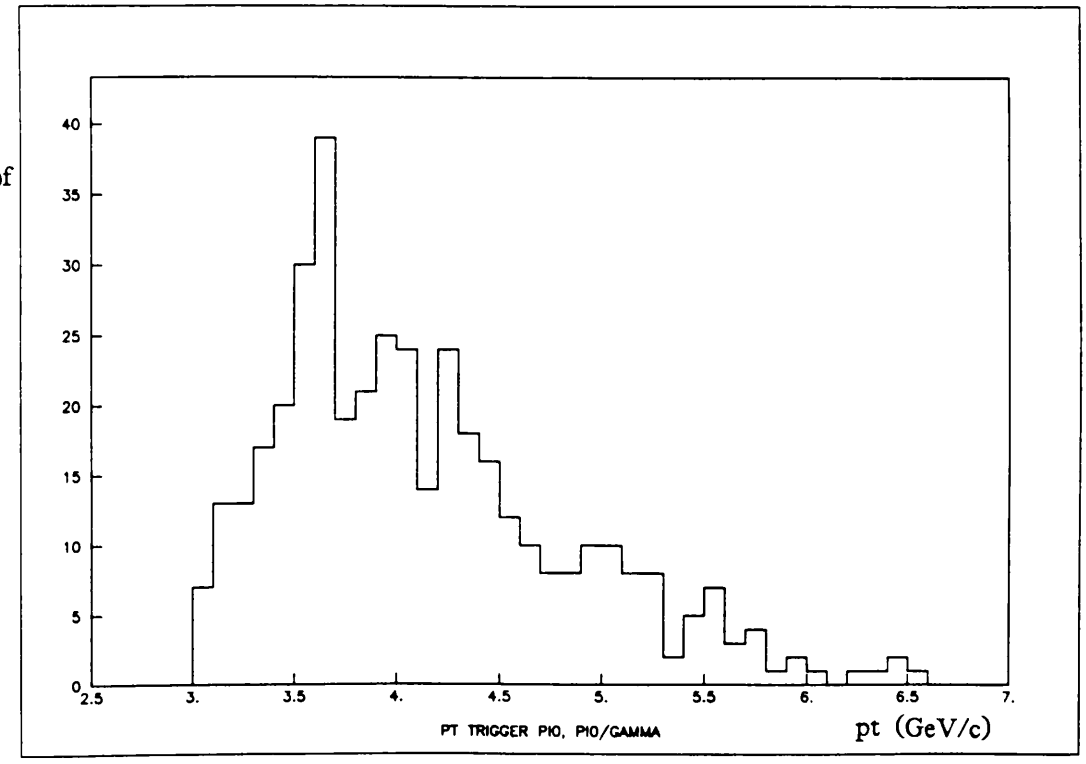

Figure 7.1b

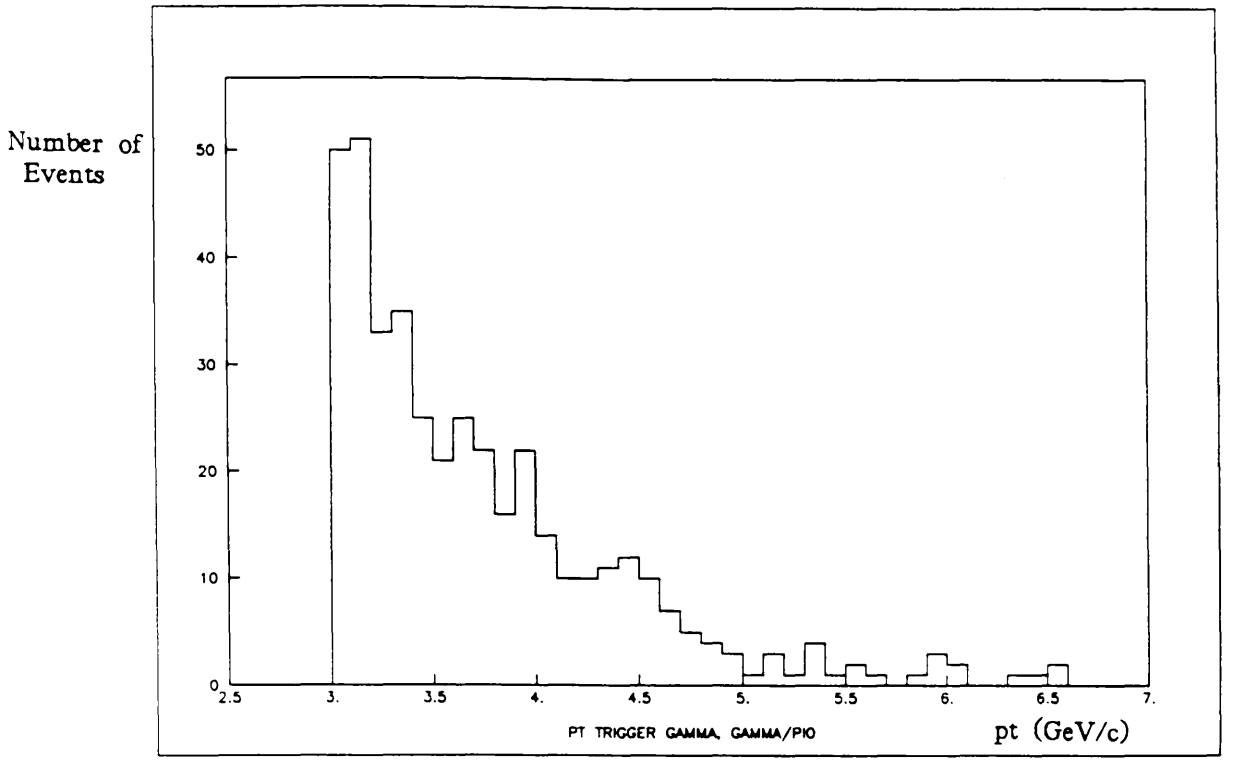

Figure 7.1c

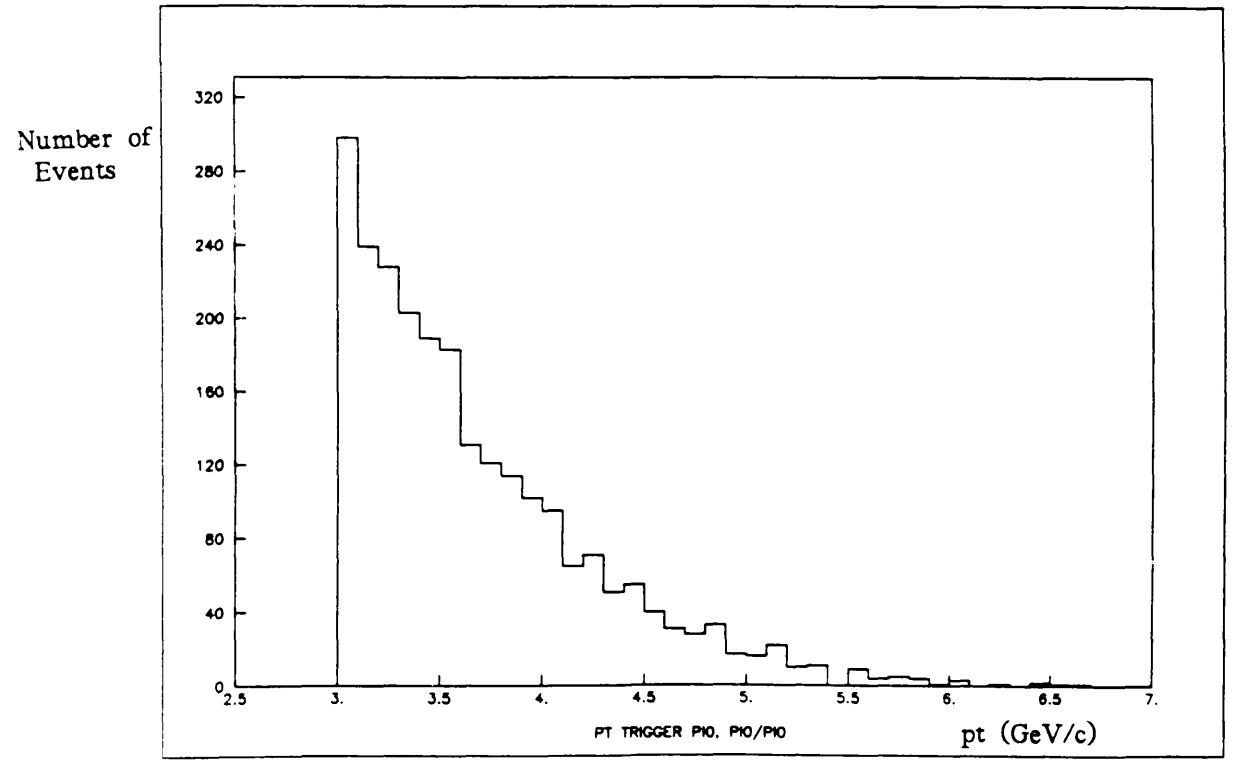

Figure 7.1d

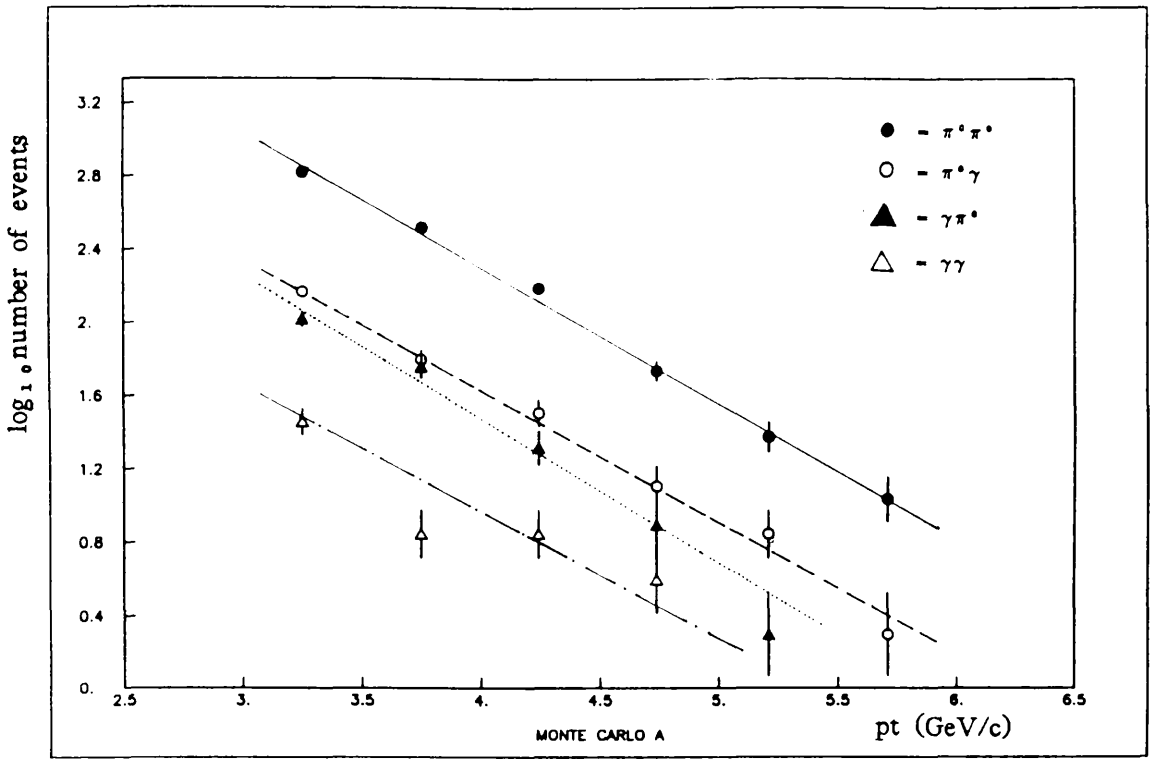

Figure 7.2a

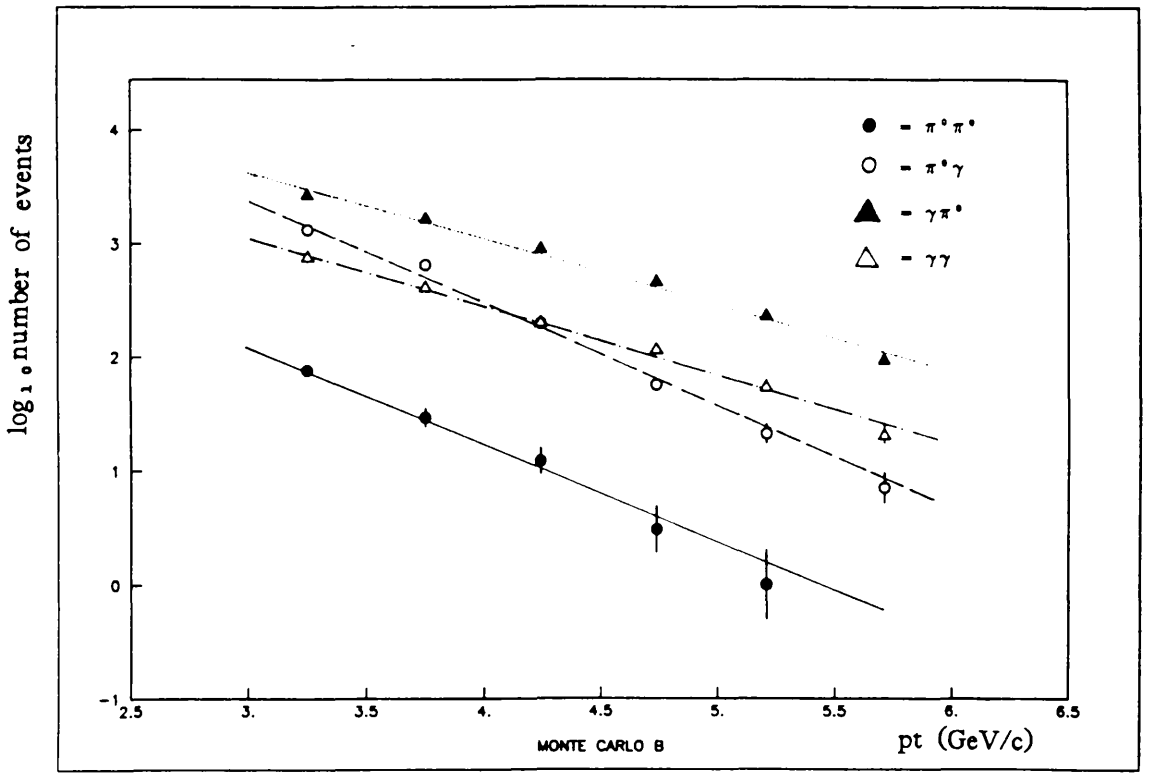

Figure 7.2b

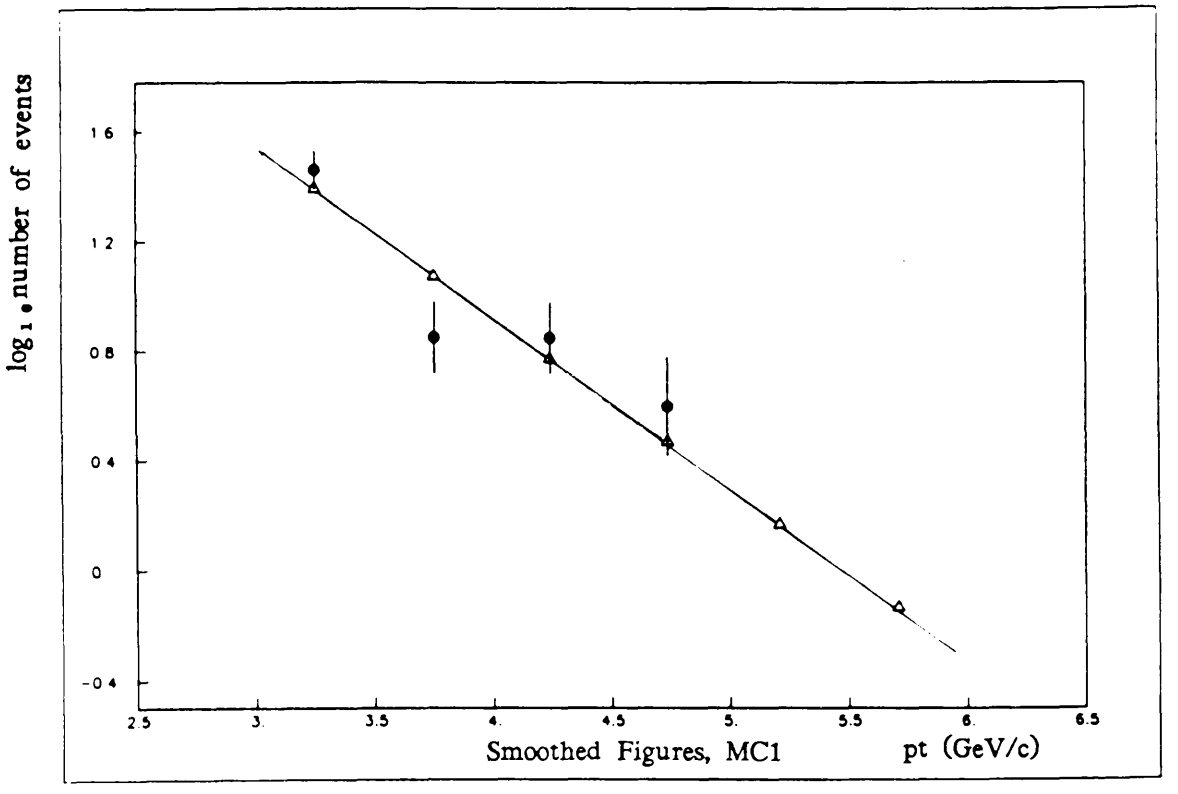

Figure 7.3a

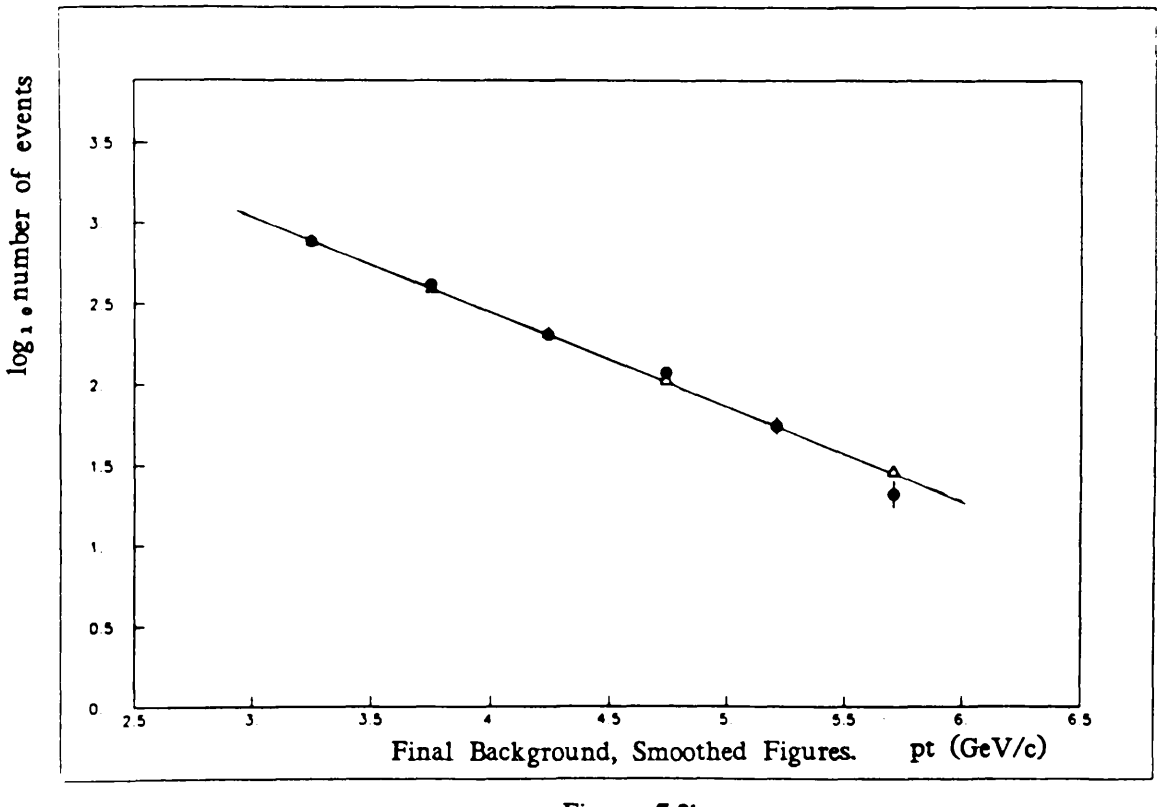

Figure 7.3b

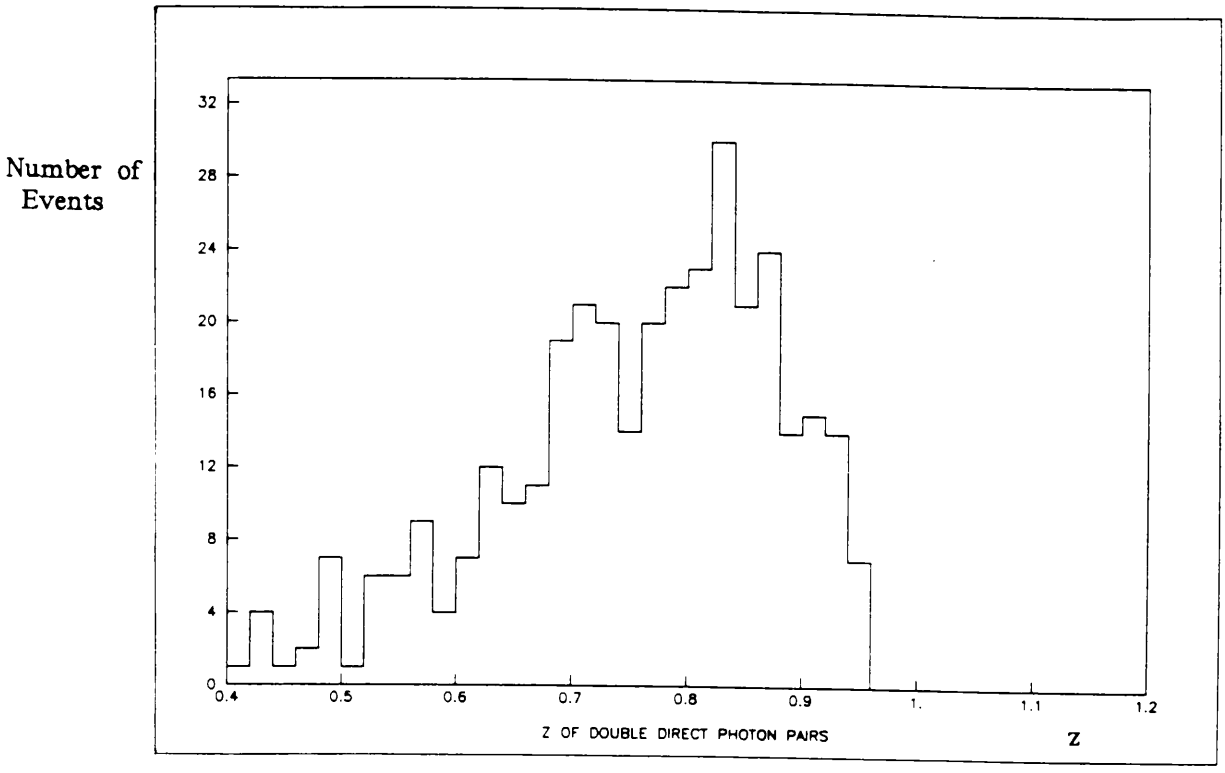

Figure 7.4

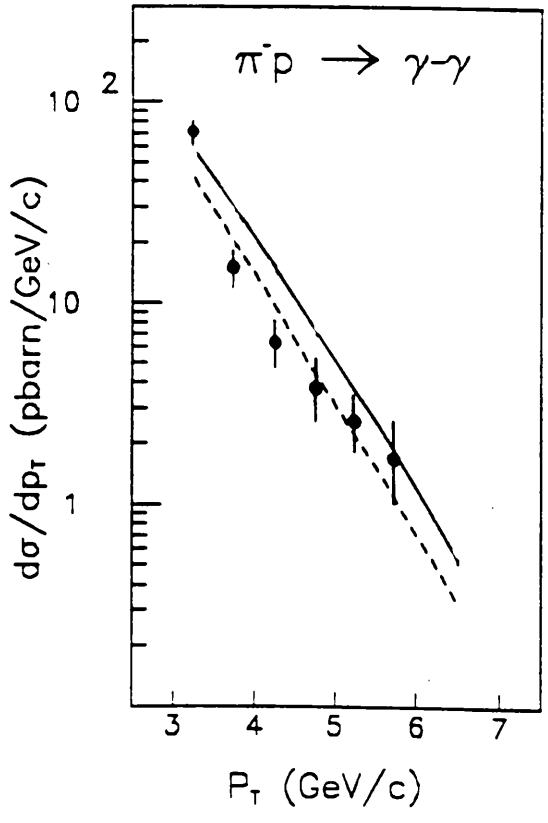

Figure 7.5

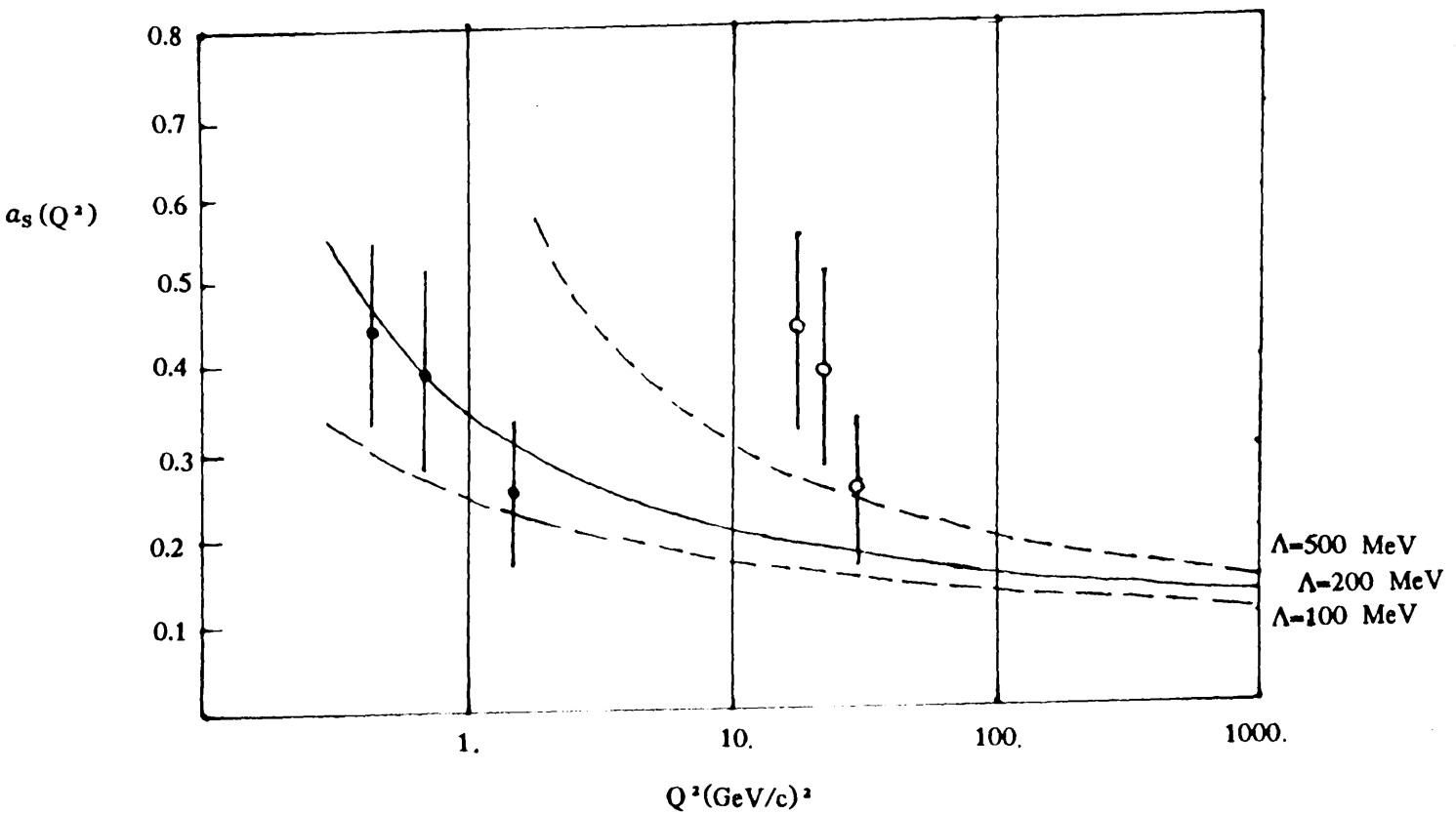
$a_s(Q^2)$
0.8
0.7
0.6
0.5
0.4
0.3
0.2
0.1
1.
10.
100.
1000.
Q^2(GeV/c)^2
Λ=500 MeV
Λ=200 MeV
Λ=100 MeV

Figure 7.6

CHAPTER 8

Conclusions.

WA70 has measured the single direct photon cross-section as a function of pt and xf to a greater accuracy than has been achieved by other experiments. This has allowed information on fundamental QCD parameters to be obtained. An examination of the direct photon cross-sections versus pt (figs. 6.1 to 6.2c) indicates that the Duke and Owens set II structure functions are incompatible with the cross-sections for the central and positive xf regions, while Duke and Owens set I structure functions are consistent with the experimental data. The reverse is true in the negative xf region, where set II are clearly favoured. When integrated over xf the cross-section data clearly favours set I over set II. The statistical errors in this case are at a minimum (fig. 6.1), and allow the set II structure functions to be rejected. The direct photon cross-section xf distributions do not allow a preference between the two sets to be made.

It can be remarked that there is no reason a priori for either of the two sets of Duke and Owens structure functions to be exactly correct. They were chosen (using Λ_{QCD} = 200 and 400 MeV for set I and set II respectively) to be the best fit to the data then available. Direct photon data was not included. The WA70 direct photon cross-section measurements have allowed a determination of the parameter Λ_{QCD}, (6.2 above), and it should be possible to derive an improved set of structure functions by incorporating the direct photon.

The direct photon cross-sections have also allowed the gluon structure function within the proton to be investigated, and an accurate determination of the

parameter η_g has been made.

The $\pi^- p \rightarrow \pi^0 X$ cross-section and the γ/π^0 ratio have also been measured.

A seven standard deviation double direct photon signal has been seen. The $\pi^- p \rightarrow \gamma\gamma X$ cross-section was found to be compatible with QCD predictions made using Duke and Owens Set I structure functions. The ratio R (section 7.9) was determined, and a measurement of the coupling constant α_s made. All the single and double direct photon cross-sections and α_s measurements could not be consistently explained using conventional $Q^2=pt^2$ scaling, but the adoption of 'optimised scales' did permit a consistent description of these quantities.

Experiment WA70 has demonstrated that very 'clean' samples of direct photons can be isolated and used to measure QCD parameters.

References.

1. Introduction to Elementary Particles, D.Griffiths, Harper and Row 1987, pp 77.

2. e.g. pp34 Collider Physics, V.D.Barger and R.J.N.Phillips, Adison-Wesley 1987.

3. Short Summary, V.A. Rubakov, Proceedings of 1987 JINR/CERN School of Physics, pp132.

4. Taken from Annual SERC Particle Physics Report, 1989.

5. e.g. R.K.Ellis, The Status of Perturbative QCD, Proceedings of the XXIV International Conference on High Energy Physics, pp48.

6. Gauge Theories in Particle Physics, I.J.R.Aitchison and A.J.G.Hey, Adam Hilger 1982.

7. Halzen F., Dechantsreiter M. and Scott D.M., Phys. Lett. B 78 (1978) pp318.

8. Contogouris A.P. Phys. Rev. D 25 (1982) pp1618.

9. Aurenche P., Douiri A., Baier R., Fontannaz M. and Schiff D., Phys. Lett. B 140 (1984) pp87

10. Contogouris A.P., Mebarki N., Tanaka H. and Vlassopulos S.D.P., Phys. Rev. D 32 (1985) pp1134

11. Turnbull R.M. J. Phys. G: Nucl. Phys. 14 (1988) pp135.

12. Baier R, Engels J. and Petersson B., Z. Phys. C 2 (1979) pp265.

13. Owens J.F., Rev. Mod. Phys. 59 (1987) pp465.

14. Contogouris A.P. and Tanaka H., Phys. Rev. D 33 (1986) pp1265.

15. Berger E.L., Braaten E. and Field R.D. Nucl. Phys. B 239 (1984) pp52.

16. Berman S., Bjorken J.D. and Kogut J. Phys. Rev D 4 (1971) pp3388.

17. Krawczyk M. and Ochs W., Phys. lett. B 79 (1978) pp199.

18. Aurenche P., Baier R., Fontannaz M. and Schiff D. Nucl. Phys.

B 286 (1987) pp509.

19. Stevenson P. and Politzer H.D., Nucl. Phys. B 277 (1987) pp509.

20. P.Aurenche, extract from talk given at Glasgow 1988.

21. Darriulat P et al Nucl. Phys. B 110, 365.

22. Ferbel T. and Molzon W.R. Rev. Mod. Phys. 56 (1984) pp181.

23. Angelis A.L.S. et al Phys. Lett. B 94 (1980) pp106.

24. Kourkoumelis C. et al Z. Phys. C 16 (1982) pp101.

25. Akesson T. et al Phys. Lett. B 123 (1983) pp367.

26. Appel J.A. et al Phys. Lett. B 176 (1986) pp239.

27. Ansari.R. et al CERN Report (1988) CERN-EP/88-102.

28. Badier J. et al Phys. Lett. B 164 (1985) pp184

29. Duke D.W. and Owens J.F. Phys. Rev. D 30 (1984) pp49.

30. De Marzo C. et al Phys. Rev. D 36 (1987) pp8.

31. Bernasconi A. et al CERN Report (1987) CERN-EP/87-120.

32. Bovet C. et al CERN report 82-13.

33. Beusch W. et al CERN reports SPSC/77-70/SPSC/T-17.

34. Gidal G. et al Berkeley report LBL-91 supplement, revised (1985).

35. Bachmann L. et al Nucl. Instr. and Meth. 206 (1983) pp85.

36. Bonesini M. et al Nucl. Instr. and Meth. 261A (1987) pp471.

37. Bonesini M. et al Nucl. Instr. and Meth. 264A (1988) pp205.

38. Bonesini M. et al Nucl. Instr. and Meth. 270A (1988) pp32.

39. Bonesini M. et al Nucl. Instr. and Meth. 263A (1988) pp325.

40. Bene P. et al Nucl. Instr. and Meth. 270A (1988) pp21.

41. Mathys, L. Thesis, University of Geneva no. 2279, 1987.

42. Lassalle J.C. et al Nucl. Inst. Meth. 176 (1980) 371-379.

43. Lassalle J.C. et al CERN report DD/EE/79-2, (1980).

44. Bengtsson, H.-U. et al Comp. Phys. Comms. 34 (1985) pp251.

45. Sjostrand T. et al Comp. Phys. Comms. 27 (1982) pp243.

46. Maxwell, R.A., thesis, University of Glasgow, 1987.

47. Lassalle J.C. and Carena F., CERN report DD/EE/79-1 (1979).

48. Ingleman G. TWISTER a Monte Carlo for QCD high pt scattering, DESY 86-131.

49. Jack, S.C. Thesis, University of Glasgow. Submitted 1989.

50. Poultney R.W. Internal WA70 report, 1987.

51. Focacci-Kienzle, M., Geneva University, private communication.

52. Lucock, R., Thesis, University of Glasgow. 1988.

53. Review of Particle Properties, Revs. of Mod. Phys., Vol. 56 no.2, part 2, April 1984.

54. Bonesini et al, paper submitted to Z. Phys. C, 1989.

55. Bonesini et al Z. Phys. C38 (1988) pp371.

56. Focacci-Kienzle, M., Geneva University, private communication.

57. Snow, S.W., Thesis, University of Liverpool, 1987.

58. Aurenche, P. et al, LPTHE Orsay preprint 88/38, 1988.

59. R806 Collaboration, Anassontzis E. et al, Z. Phys. C 13 (1982) pp277.

60. BCDMS collaboration, Phys. Lett. B 195 (1987) pp97.

61. Aurenche, P. Baier R., Douiri, Fontannaz M. Z. Phys. C 29 (1985) pp459.

62. Bonvin E. et al, Z. Phys. C 41 (1989) pp591.

63. Focacci-Kienzle, M., Geneva University, private communication 1988.